Hannon, A. C. In: *Modern glass characterization,* Ed. M. Affatigato, Wiley, New York, 2015, Chapter 5, p. 158-240.

5

NEUTRON DIFFRACTION TECHNIQUES FOR STRUCTURAL STUDIES OF GLASSES

Alex C. Hannon

ISIS Facility, Rutherford Appleton Laboratory, Chilton, Didcot, Oxon, UK

5.1 INTRODUCTION

Neutron diffraction (ND) is an important experimental technique for the investigation of the structure of glasses. It can be used to study oxide glasses, chalcogenide glasses, metallic glasses, amorphous semiconductors, molecular glasses, amorphous polymers, organic glasses, and so on. An ND experiment yields a measurement of the distribution of interatomic distances that can be more accurate than for any other experimental method. The shortest distances in the glass (the short range order, SRO) can be characterized in terms of coordination numbers, bond lengths, and other short distances. These can be measured very accurately by ND, and used to determine the coordination polyhedra that form the basis of the glass structure. The way in which these units connect together (the intermediate range order, IRO) is also probed by ND, although in a more subtle way, and its investigation usually requires some kind of modeling of the ND results. The results of an ND experiment can be predicted exactly for a structural model, and hence ND provides a rigorous test of structural models.

The main aim of this chapter is to provide empirical information to enable a new researcher, such as a research student, to plan and perform an ND investigation of the structure of glass samples, to analyze the experimental data, and to begin to interpret

Modern Glass Characterization, First Edition. Edited by Mario Affatigato.

the results. A brief outline is given of the theory of ND for glasses; particular emphasis is given to subjects such as incoherent scattering, which new researchers tend to find especially troubling. The study of glass structure by ND is best not considered in isolation, but instead in the wider context of both the study of other types of material, and the use of other techniques to study glass structure. Therefore, whilst the main emphasis of this chapter is very much on ND from glasses, this is set in the wider context of liquid and crystalline materials when relevant; the experimental approaches described here can also be of use in the study of these other types of material. It is also worth mentioning that there are other neutron scattering techniques of use in the study of glass, such as inelastic scattering and quasi-elastic scattering, which are beyond the scope of this chapter.

5.2 INSTRUMENTATION

5.2.1 The Neutron

The neutron was discovered relatively recently by Chadwick in 1932, for which he received the Nobel Prize for physics in 1935. Soon after that, Fermi received the Nobel Prize in physics for studies of the interactions between neutrons and matter, but it was many years before the Nobel Prize in physics was belatedly awarded to Brockhouse and Schull for the development of neutron scattering techniques for studies of condensed matter. It is useful to consider the properties of the neutron, as given in Table 5.1, because they lead to some important advantages and limitations for the use of ND.

Bound neutrons in a stable nucleus are stable, but free neutrons undergo β-decay with a mean lifetime of approximately 15 minutes. Thus a nuclear reaction of some sort is required to produce a beam of neutrons for a diffraction experiment. In practice the number of neutrons produced by a radioactive source is insufficient for a useful diffraction experiment, and the only two methods currently capable of producing enough neutrons are either nuclear fission in a nuclear reactor, or the interaction of an accelerated particle beam with a target. Accelerators and reactors are large, expensive facilities, and hence their availability is limited; the total number of neutron sources in the world is probably less than 30. The use of a diffractometer at most neutron sources may be requested by submission of an experimental proposal, and further information about the application procedure should be sought on the internet.

TABLE 5.1. Properties of the neutron.

Mass	$m_n = 1.00866491600$ amu
Mean free lifetime	881.5 s
Charge	zero
Spin	$^1/_2$
Magnetic dipole moment	$\mu_n = -1.91304272\ \mu_N$

5.2.2 The Interactions between a Neutron and a Sample

As implied by its name, the neutron is neutral. The lack of a charge means that a neutron does not interact with the electric field in a sample, and this is part of the reason why the interaction between a neutron and a sample is relatively weak. The main interaction between a neutron and a sample is the nuclear force between the neutron and the nuclei of the sample, and this interaction occurs for all samples. The neutron has spin $\frac{1}{2}$ and a non-zero magnetic dipole moment, and consequently there is a magnetic interaction between a neutron and the unpaired electrons in the atoms in a sample. Therefore, for samples containing magnetic ions, there is a magnetic interaction between a neutron and the sample, in addition to the nuclear interaction. A detailed consideration of magnetic diffraction is beyond the scope of this chapter, but Section 5.4.7.1 indicates how paramagnetic self scattering can be taken into account.

The interaction between a neutron beam and a sample (via nuclear forces and the magnetic interaction) is relatively weak, compared to the interaction between an X-ray beam and a sample (via the electromagnetic interaction), and hence ND is an intensity-limited technique. Thus it is always important to ensure that an ND experiment yields results with sufficiently good statistical accuracy; this is achieved by using relatively large samples (the volume of a typical ND sample is of order 1 to 2 cm^3), and the longest possible counting time. Nevertheless, the relatively weak interaction for neutrons is highly advantageous because the experimental corrections (for absorption, multiple scattering, etc.) can often be performed much more reliably for ND, leading to more accurate results.

It is useful to consider the simple case of a neutron beam with wavevector $\boldsymbol{k}$, parallel to the z-axis (see Figure 5.1), which is incident on a single fixed nucleus. In this case the incident wavefunction can be represented as

$$\psi_{\text{inc}} = \exp(\mathrm{i}kz). \tag{5.1}$$

If the neutron wavelength is of the order 1 Å, then this is larger than the size of a nucleus by a factor *ca.* 10^5. Therefore the waves scattered by different parts of the nucleus will all be in phase, with the result that the total scattered wave is spherically symmetric. In this case the scattered wavefunction at the point $\boldsymbol{r}$ is

$$\psi_{\text{sc}} = -\frac{b}{r}\exp(\mathrm{i}kr) \tag{5.2}$$

where b is a constant, known as the scattering length of the nucleus. The scattering length determines the amplitude of the wave scattered by the nucleus, and it is defined so that a positive value corresponds to a phase change of π between the incident and scattered waves. It is very important to note that the scattered wave is spherically symmetric, so that b is not a function of scattering angle; instead b is a simple constant. Thus, nuclear neutron scattering does not involve a form factor (unlike X-ray diffraction, or magnetic ND), with the result that reliable information can be measured up to high momentum transfer, leading to high resolution in real space and accurate bond lengths.

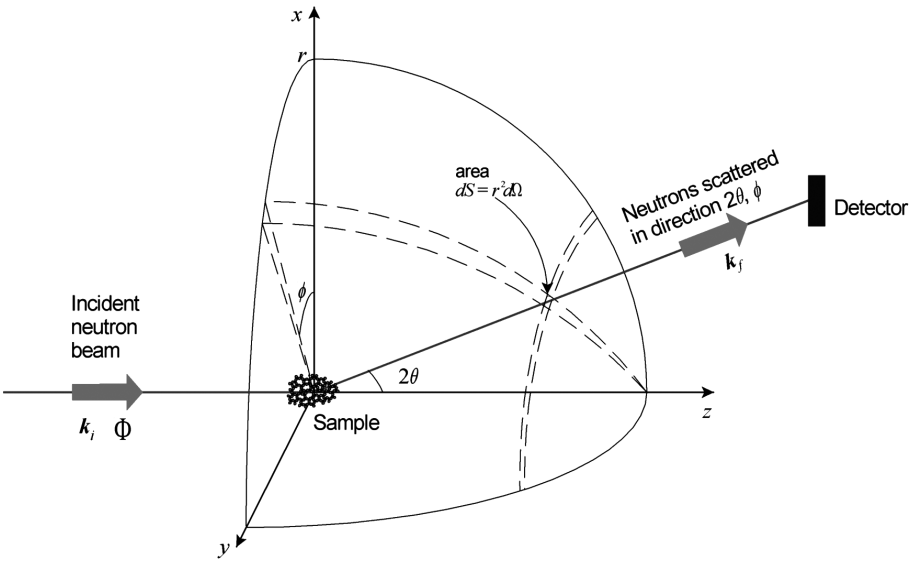

Figure 5.1. The geometry for a neutron diffraction experiment.

The neutron mass is similar to the mass of a proton ($m_n/m_p \approx 1.0014$), and thus inelastic scattering processes (where the neutron exchanges energy with the sample) are of great importance, especially for samples containing hydrogen (i.e., protons which are not bound in a larger nucleus). A neutron with energy E has a de Broglie wavelength, λ, given by the non-relativistic expression

$$E = \frac{h^2}{2m_n\lambda^2} \tag{5.3}$$

(or $E = 81.787/\lambda^2$ in convenient units of meV and Å, respectively), and thus the neutron exhibits wavelike behavior including diffraction. Diffraction effects are most clearly observed if the wavelength is similar to the distances between the scattering centers. For example, the silicon–oxygen bond length in SiO_2 glass is 1.61 Å, and a neutron with this wavelength has an energy *ca.* 31 meV. Thus neutrons with a wavelength suitable for a diffraction experiment also have an energy which is similar in magnitude to the vibrational energies in solids (e.g., the largest vibrational energy in SiO_2 glass is *ca.* 170 meV). Consequently, inelastic scattering phenomena are of great importance, and inelastic neutron scattering experiments can provide an important fundamental probe of the structure of glasses.

5.2.3 Neutron Sources

5.2.3.1 Reactor Sources Neutron beams for ND first became available in the 1940s, with the advent of nuclear reactors in which neutrons are produced by the fission

of ^{235}U nuclei. The cross-section for neutron-induced fission of ^{235}U is high only for slow neutrons with energies in the meV range, whereas the fast neutrons produced by fission have much higher energies in the MeV range. Hence, in order to sustain the fission process, a reactor includes a component, known as a moderator, which slows down the neutrons. The neutrons undergo inelastic collisions (see Section 5.2.2) with the nuclei in the moderator, so that they are in thermal equilibrium at the temperature of the moderator. The moderator normally contains large numbers of low mass nuclei (usually H or D), because the energy transferred in the inelastic collisions is maximized when the mass of the colliding nucleus is as close as possible to the neutron mass. The peak flux within the moderator is at a neutron speed v_p given by

$$E = \frac{1}{2} m_n v_p^2 = k_B T, \tag{5.4}$$

where T is the temperature of the moderator. For example, a temperature of 290 K corresponds to a neutron energy E of 25 meV, a neutron wavelength λ of 1.8 Å, or a neutron speed v of 2200 m/s. It is thus fortuitous that the process of moderation produces neutrons which, as well as being slowed down for maintaining the fission reaction, also have a wavelength suitable for performing ND experiments.

A neutron diffractometer uses a beam of neutrons that is obtained by viewing a moderator through a beam-tube or neutron guide which passes through the shielding around the neutron source. Note that in practice the moderator used as a source of neutrons for ND experiments at a reactor may be separate from the moderator used to slow the neutrons in order to maintain the fission reaction. Figure 5.2 shows the neutron flux for three different moderators at the world's pre-eminent reactor source of neutrons, the Institut Laue-Langevin (ILL) in Grenoble, France. Reactor neutron sources produce a high flux of thermal neutrons (E∼25 meV, T∼290 K) and cold neutrons (E∼1 meV, T∼12 K), but they have little flux at higher epithermal energies (E∼1 eV, T∼12000 K). This is a consequence of the fact that a reactor can only produce neutrons which are in thermal equilibrium with a moderator, and there are practical limitations on the maximum temperature of the moderator.

The neutron flux produced by a normal nuclear reactor is unchanging with time and covers a wide range of neutron wavelengths. In order to perform an ND experiment it is thus necessary to monochromate the neutron beam from a reactor so that it covers a narrow range of neutron wavelengths, and the vast majority of the flux from the source is lost at this stage.

5.2.3.2 Accelerator Sources Since the 1960s, ND experiments have increasingly come to be performed using sources of neutrons that are based on a particle accelerator. A beam of charged particles is accelerated to a high energy and then fired at a target. Interactions between the particle beam and the nuclei in the target produce high energy neutrons that are then slowed down by a moderator.

The earlier accelerator-based neutron sources used an electron linear accelerator to accelerate an electron beam to relativistic energies (∼50 MeV), which was then fired at a dense target made of a heavy element, usually uranium, and neutrons were produced

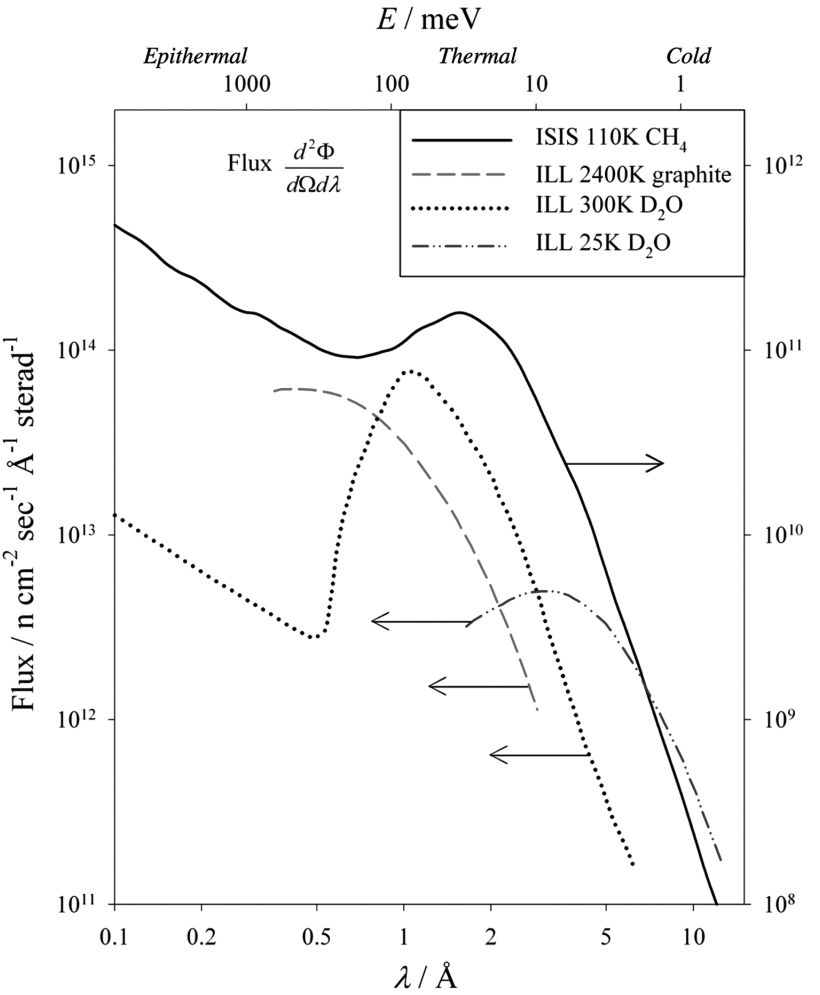

Figure 5.2. The neutron flux distribution for three different moderators at the ILL reactor (left-hand scale) and for the liquid methane moderator at the ISIS accelerator (right-hand scale).

by a two-stage process. Firstly, the electrons were slowed down extremely rapidly due to the strong interaction with the electromagnetic field of the target nuclei, producing a cascade of bremsstrahlung photons. Secondly, some of these photons went on to produce neutrons by photo-neutron reactions, where the photon excites a target nucleus that subsequently decays with the emission of a neutron. Approximately 20 electrons must be accelerated for each neutron produced.

More recent accelerator-based neutron sources use a linear accelerator, sometimes in combination with a synchrotron, to accelerate a beam of protons to a high energy (~800 MeV). The proton beam is fired at a heavy metal target (made for example of

tantalum, tungsten, uranium, or mercury), and neutrons are produced by the spallation process. Spallation is a violent interaction between the proton and the target nucleus that results primarily in the emission of neutrons, but also a variety of light nuclear fragments. In effect, the protons chip pieces off the target nuclei, and each proton produces about 15 neutrons for a non-fissile target (or about 25 neutrons for a fissile target).

Accelerator-based sources are usually pulsed[1] (typically with a pulse repetition rate of order 50 Hz), and so they produce a pulsed neutron flux that is ideally suited to the time-of-flight ND technique. This technique involves measuring the time-of-flight (T-O-F), t, for a neutron to travel the total flight path, L, from the moderator to the detector, via the sample. On the assumption of elastic scattering (i.e., initial and final neutron energies are the same, $E_i = E_f$) then

$$t = \frac{m_{\mathrm{n}}}{h} L\lambda, \tag{5.5}$$

(or $t = 252.82L\lambda$ in convenient units of μs, meters, and Ångstroms, respectively), and it is straightforward to determine the neutron wavelength. The use of the T-O-F technique removes the need to monochromate the neutron beam and thus, even though the raw flux produced initially by an accelerator-based source is much less than that produced by a reactor source, the final flux available for ND is of a comparable order of magnitude (see Figure 5.2).

The moderator at an accelerator-based neutron source is used to slow the neutrons down so that they have suitable wavelengths for ND, in the same way as for a reactor neutron source. However, in order that the moderation process does not broaden the pulsed time structure of the neutron flux too much, the moderator must be relatively small. (Also note that, unlike a reactor, the process of moderation plays no role in the production of neutrons at an accelerator-based source.) This has the consequence that the neutrons produced by an accelerator-based source are under-moderated and there are many more epithermal neutrons (i.e., neutrons with energy greater than thermal neutrons, see Figure 5.2) than for a reactor source. Figure 5.2 also shows the neutron flux for a moderator at the ISIS spallation neutron source at the Rutherford Appleton Laboratory, UK. The epithermal neutrons at a pulsed neutron source allow diffraction patterns to be measured up to high momentum transfers, and it is this which enables high resolution in real space to be achieved (see Section 5.4.2.2).

5.2.4 Neutron Diffractometers

5.2.4.1 Neutron Diffractometers—General Principles The purpose of a total neutron diffractometer is to measure the differential cross-section

$$I^{\mathrm{N}}(Q) = \left(\frac{d\sigma}{d\Omega}\right)_{\mathrm{tot}} = \frac{R_{\mathrm{tot}}}{N\Phi d\Omega}, \tag{5.6}$$

[1] Accelerator-based neutron sources which are quasi-steady-state or intensity-modulated also exist. Furthermore pulsed neutrons have also been produced in Russia by using a pulsed reactor.

where R_{tot} is the rate at which neutrons of wavelength λ are scattered into the solid angle $d\Omega$ in the direction $(2\theta,\phi)$ (see Figure 5.1), irrespective of whether or not they are scattered elastically (i.e., total neutron scattering). N is the number of atoms in the sample and Φ is the flux of neutrons of wavelength λ that is incident on the sample.

In general the differential cross-section depends upon the scattering vector

$$\boldsymbol{Q} = \boldsymbol{k}_i - \boldsymbol{k}_f, \tag{5.7}$$

where $\boldsymbol{k}_i$ and $\boldsymbol{k}_f$ are the neutron wavevector before and after scattering. The term *momentum transfer* (i.e., the momentum transferred to the sample) is commonly used for $\boldsymbol{Q}$, although strictly speaking this term should be used for $\hbar\boldsymbol{Q}$. Diffraction data are treated by considering the scattering to be totally elastic so that the magnitudes of the initial and final neutron wavevectors are the same,

$$|\boldsymbol{k}_i| = |\boldsymbol{k}_f|. \tag{5.8}$$

Most glass samples are isotropic (i.e., their properties are the same in all directions), and for an isotropic sample it is only the magnitude of the momentum transfer that is significant, in which case the differential cross-section is a function of a single variable

$$Q = |\boldsymbol{Q}| = \frac{4\pi \sin\theta}{\lambda}. \tag{5.9}$$

For ND experiments on polycrystalline powders it is usually more convenient to treat the differential cross-section as a function of d-spacing, d $(= 2\pi/Q)$, defined according to Bragg's law by

$$2d \sin\theta = \lambda. \tag{5.10}$$

Bragg peaks are then observed in the differential cross-section whenever the d-spacing satisfies

$$d = d_{hk\ell}, \tag{5.11}$$

where $d_{hk\ell}$ is a d-spacing between atomic planes (with Miller indices $(hk\ell)$) in the crystal for which the structure factor is non-zero.

To produce high quality data, a neutron diffractometer must satisfy several requirements: (i) The data must have a good statistical accuracy, which is obtained by having a high count rate. This is achieved by such factors as an intense source, a large total detector solid angle, and a sufficiently large sample. (ii) The corrections that are made to the data must be as small as achievable. In particular the background must be small, featureless and unchanging. (iii) The range in Q must be as wide as possible, in order to provide high resolution in real space. (iv) The reciprocal-space resolution must be as narrow as possible.

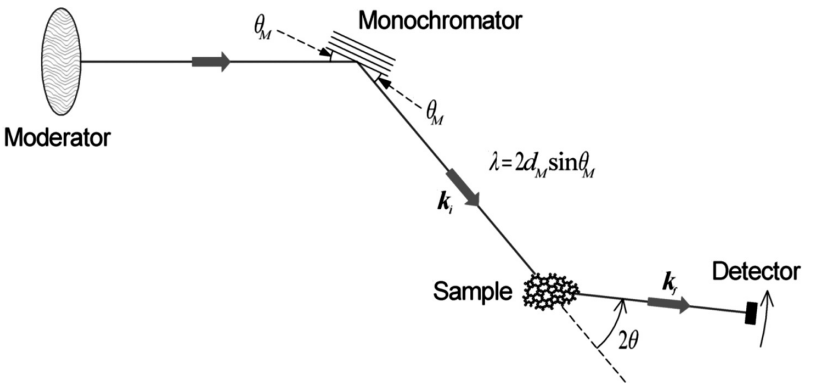

Figure 5.3. Schematic of a neutron diffractometer for a continuous source.

Due to its lack of charge, a neutron cannot be detected by directly producing an electrical current in a detector. Instead a more indirect method of detection is used, involving a nuclear reaction that releases energy, which is then turned into an electrical signal, such as the absorption of a neutron by a ^{3}He nucleus

$$^3_2\mathrm{He} + ^1_0\mathrm{n} \rightarrow ^3_1\mathrm{H} + ^1_1\mathrm{p} + 0.770\ \mathrm{MeV}. \tag{5.12}$$

Neutrons are usually detected using single particle counting.

5.2.4.2 Reactor Source Diffractometers A schematic of the layout of a typical neutron diffractometer at a continuous (reactor) source is illustrated in Figure 5.3. The neutron beam coming from the moderator at a conventional reactor covers a wide range of wavelengths and is unchanging with time. Therefore a single crystal monochromator is used to produce a monochromatic beam. The general principle of operation of a neutron diffractometer at a steady state source is the same as for a conventional laboratory X-ray diffractometer, since both have a well-defined incident wavelength. The differential cross-section is measured as a function of Q by moving the detector to different scattering angles, 2θ, and measuring the scattered count rate. That is to say, Q (or d) is scanned by varying 2θ whilst keeping the neutron wavelength λ constant (c.f. Eq. 5.9).

Figure 5.4 shows the D4c diffractometer [1] at the ILL reactor which, for many years, has been the most successful reactor-based diffractometer for studying the structure of liquids and amorphous materials. The diffractometer uses neutrons from a hot graphite moderator at a temperature of 2400 K, because this produces neutrons with short wavelengths and hence a high maximum Q can be achieved, leading to good real-space resolution. A copper monochromator is used to produce neutrons with a wavelength of 0.7 Å, 0.5 Å or 0.35 Å, depending on which copper reflection is selected. Most of the neutron flight path is evacuated in order to minimize background due to the scattering of neutrons by air. There are nine one-dimensional position sensitive detectors, each of

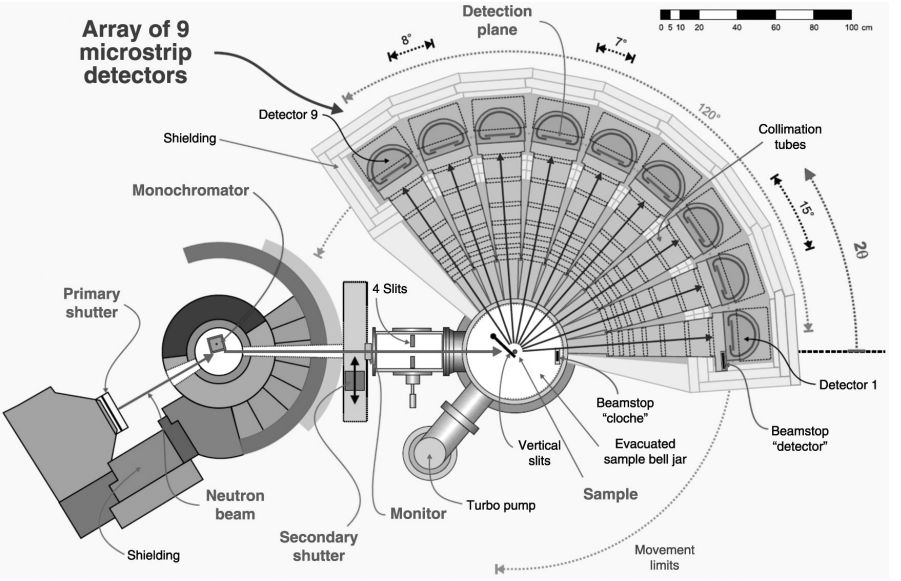

Figure 5.4. The D4c liquids and amorphous diffractometer at the Institut Laue Langevin [1].

which is a micro-strip detector with 64 elements. The large number of detectors is used to provide a large detector solid angle and hence a high count rate. The detectors can cover a range in scattering angle, 2θ, from 1.5° to 140°, and with a wavelength of 0.5Å the Q-range of D4c extends from 0.3 to 24 $Å^{-1}$. (A higher maximum Q may be attained with a wavelength of 0.35 Å, but the flux available at this wavelength is an order of magnitude lower and is too low for regular use.)

5.2.4.3 Pulsed Source Diffractometers A schematic of the layout of a typical T-O-F neutron diffractometer at a pulsed source is illustrated in Figure 5.5. The T-O-F

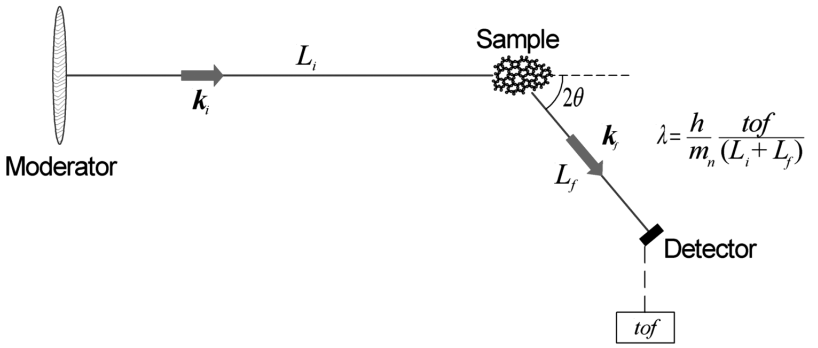

Figure 5.5. Schematic of a time-of-flight neutron diffractometer for a pulsed source.

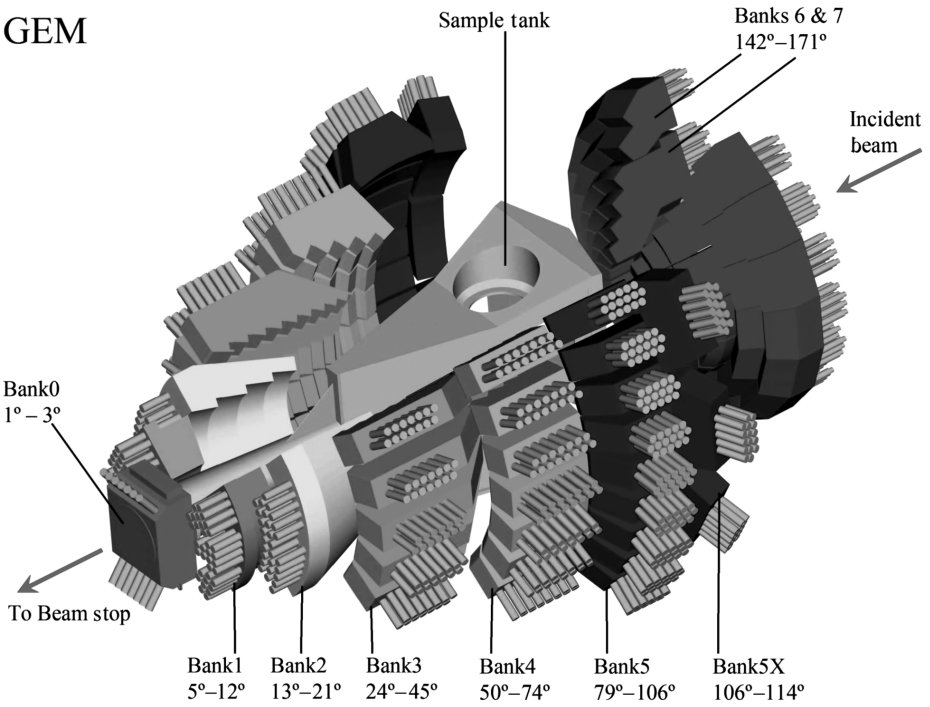

Figure 5.6. The GEneral Materials diffractometer, GEM, at the ISIS Facility [2]. See plate section for a color version of this figure.

technique (see Eq. 5.5) is used to determine the wavelength of the detected neutrons and hence a monochromator is not needed. The differential cross-section is measured as a function of Q with the detector at a fixed scattering angle, 2θ, and Q (or d) is scanned by varying the neutron wavelength λ (c.f. Eq. 5.9). The T-O-F technique is thus a dispersive technique and a white beam covering a wide range of wavelengths is incident on the sample. For diffraction from a crystalline powder, pulsed source data have the simplifying property that T-O-F is proportional to d-spacing;

$$t = \frac{2m_n}{h} Ld \sin\theta, \tag{5.13}$$

(or $t = 505.64Ld\sin\theta$ in convenient units of μs, meters, and Ångstroms, respectively). A noteworthy advantage of the ability to measure a full diffraction pattern at a single fixed scattering angle is that complex sample environment equipment can be used (e.g., for high pressures) with two well-collimated flight paths for the incident and scattered beams so that background from the equipment is minimized.

Figure 5.6 shows the GEneral Materials diffractometer, GEM [2], at the ISIS spallation neutron source, which is arguably the best neutron diffractometer in the world for high real-space resolution studies of glass structure. The neutron beam comes from a liquid methane moderator at a temperature of 110 K. A cooled moderator is used in

order to reduce the correction for inelasticity effects. The length of the incident flight path, L_i, is 17.0 m, leading to a high resolution in reciprocal space. In practice a T-O-F diffractometer has several different detector banks at different scattering angles, 2θ, in order to extend the Q-range of the data, and GEM has detector banks at eight different scattering angles. The detectors are ZnS scintillators with narrow 5 mm active elements so as to minimize the angular contribution to the reciprocal-space resolution, and the best resolution ($\Delta Q/Q \sim 0.35\%$) is obtained from the backward angle detectors. The detectors cover a very large solid angle (area$\sim$10 m^2, maximum azimuthal angle$\sim$45°) so as to achieve a high effective count rate. A nimonic t_0 chopper at a distance 9.3 m from the moderator is used to close off the beam at $t = 0$, and thus prevent very fast neutrons and prompt gamma rays from reaching the sample. This prevents high energy neutrons from thermalizing in large pieces of sample environment equipment (e.g., high pressure equipment) and then giving rise to a substantial background. In addition two disc choppers are used at flight paths of 6.5 m and 9.5 m to define a restricted wavelength range for the beam reaching the sample. This is done so as to avoid frame overlap, which can be a significant problem for a diffractometer with a longer flight path. Frame overlap occurs when slower neutrons from a pulse of the source are overtaken by faster neutrons from the subsequent pulse. If the flux of the slower neutrons is significant, then a diffraction peak which in reality is detected at the long T-O-F t, appears to be detected at the earlier time t-τ_0 (where τ_0 is the period of the source), and this leads to spurious peaks in the data. The sample tank contains an oscillating radial collimator, made of ^{10}B-coated mylar vanes, which collimates the secondary flight path from sample to detector, thus reducing background, especially from bulk sample environment such as high pressure equipment. However, for most simple glass structure studies, the oscillating collimator is removed because it imposes a rapidly changing profile on the scattered neutrons, which may be problematic for the experimental corrections.

5.3 THEORETICAL ASPECTS OF NEUTRON DIFFRACTION ON GLASSES

5.3.1 The Static Approximation

The outline of ND in this chapter is given within the static approximation, in which the atoms in a sample are fixed, so that their positions do not change and they do not exchange energy with a neutron beam. For a more rigorous theoretical derivation of results, including the effects of inelastic scattering, the reader should consult other more fundamental texts [3–7].

5.3.2 Scattering from a Single Nucleus

For the single fixed nucleus considered above in Section 5.2.2, the cross-section can be evaluated using Eq. 5.6. The incident neutron flux is $\Phi = |\psi_{\text{inc}}|^2 = 1$ (see Eq. 5.1), whilst the rate at which neutrons are scattered into the area dS is $R_{\text{tot}} = |\psi_{\text{sc}}|^2 dS = b^2 d\Omega$

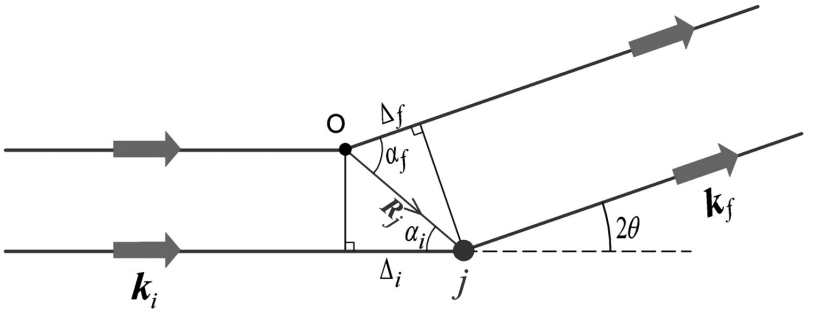

Figure 5.7. The scattering geometry for a single atom, *j*, at a position $\boldsymbol{R}_j$ relative to an arbitrary origin O. For the wave scattered from the atom, there is a path length difference $\Delta_i - \Delta_f = \boldsymbol{R}_j.(\hat{\boldsymbol{k}}_i - \hat{\boldsymbol{k}}_f)$ relative to the origin.

(see Figure 5.1 and Eq. 5.2). The differential cross-section for the single fixed nucleus is then

$$I^{\mathrm{N}}(Q) = \left(\frac{d\sigma}{d\Omega}\right)_{\mathrm{tot}} = b^2. \tag{5.14}$$

Integrating this expression over all possible directions for the scattered neutron gives the total cross-section for the nucleus as $\sigma = 4\pi b^2$, and the transmission of a thickness x of identical non-interacting atoms with number density ρ^0 is given by the Beer–Lambert law,

$$T = \frac{I(x)}{I_0} = \exp(-\rho^0 x\sigma). \tag{5.15}$$

Usually scattering lengths are given in units of fm (i.e., 10^{-15} m), but cross-sections are given in units of barns (10^{-28} m). This can lead to an error by a factor of 100 if sufficient care is not taken when using tabulated scattering lengths to calculate a cross-section.

5.3.3 Scattering from an Assembly of Nuclei

Figure 5.7 shows the scattering geometry for a single atom, *j*, at position $\boldsymbol{R}_j$ relative to an arbitrary origin O. For the wave scattered from the atom, there is a path length difference $(\Delta_i - \Delta_f)$ relative to the origin. This is equivalent to a phase difference $(\boldsymbol{Q}.\boldsymbol{R}_j)$ (using Eq. 5.7). For an assembly of N nuclei, the scattered wavefunction involves a sum over the phase factors for all the nuclei,

$$\psi_{\mathrm{sc}} = \sum_{j=1}^{N} -\frac{b_j}{r}\exp(\mathrm{i}\boldsymbol{Q}.\boldsymbol{R}_j). \tag{5.16}$$

The differential cross-section is then given by

$$I^{\mathrm{N}}(\boldsymbol{Q}) = \frac{r^2}{N}\left|\psi_{\mathrm{sc}}\right|^2 = \frac{1}{N}\sum_{j=1}^{N}\sum_{k=1}^{N} b_j b_k \exp(\mathrm{i}\boldsymbol{Q}.(\boldsymbol{R}_j - \boldsymbol{R}_k)). \tag{5.17}$$

Thus the scattered intensity depends on a sum over all the interatomic vectors, $(\boldsymbol{R}_j - \boldsymbol{R}_k)$, in the sample.

5.3.4 Isotropic Samples

Glasses and crystalline samples are usually isotropic, in which case the scattered intensity depends on the magnitude of the momentum transfer, $Q = |\boldsymbol{Q}|$, but not on the direction of $\boldsymbol{Q}$. In this case, averaging Eq. 5.17 over all directions of $\boldsymbol{Q}$ leads to the Debye equation,

$$I^{\mathrm{N}}(Q) = \frac{1}{N}\sum_{j=1}^{N}\sum_{k=1}^{N} b_j b_k \frac{\sin(QR_{jk})}{QR_{jk}}, \tag{5.18}$$

where R_{jk} is the magnitude of the interatomic vector, $(\boldsymbol{R}_j - \boldsymbol{R}_k)$, that is, R_{jk} is the distance between atoms j and k.

5.3.5 Coherent and Incoherent (Distinct and Self) Scattering

A significant difference between ND and XRD (X-ray diffraction) concerns the incoherent scattering from the sample. For XRD, the scattering power (i.e., the form factor) of all atoms of the same element may be regarded as identical. However, for ND, the scattering length b_j (i.e., the amplitude of the neutron wave scattered by a nucleus) is not the same for all nuclei of a particular element due to two factors, isotopic incoherence and spin incoherence. Isotopic incoherence arises as a result of the presence of more than one isotope of a particular element. Spin incoherence is due to the fact that a neutron and a nucleus of spin I can form two different compound nuclei of spin $I \pm 1/2$; the amplitude of the neutron wave scattered by the nucleus, and thus the scattering length, is generally different for the two different compound nuclei.

For a consideration of coherent and incoherent scattering it is convenient to write Eq. 5.18 in the form

$$I^{\mathrm{N}}(Q) = \sum_{j=1}^{N}\sum_{k=1}^{N} b_j b_k \langle j, k\rangle, \tag{5.19}$$

The value of b_j is not the same for all the nuclei of a single element, due to isotopic and spin incoherence, and hence to obtain a useful result Eq. 5.19 is averaged over all possible distributions of scattering length for atoms of the same element, making the assumption that there is no correlation between the values of b_j for any two nuclei. Now

the average value of $b_j b_k$ differs, depending whether or not $j = k$ is satisfied.

$$\begin{aligned} \overline{b_j b_k} &= (\bar{b})^2, \qquad \text{if } j \neq k \\ \overline{b_j b_k} &= \overline{b^2}, \qquad \text{if } j = k \end{aligned} \tag{5.20}$$

where $\bar{b}$ is the average scattering length (also called the coherent scattering length) for all nuclei of a particular element, whilst $\overline{b^2}$ is the average of the squared scattering length for the relevant element. (In Eq. 5.20, it is assumed that j and k can refer to two nuclei of the same element.) The double summation of Eq. 5.19 may thus be separated into $j \neq k$ (distinct) terms and $j = k$ (self) terms;

$$I^{\mathrm{N}}(Q) = i^{\mathrm{N}}(Q) + I^{\mathrm{S}}(Q), \tag{5.21}$$

where the self scattering is given by

$$I^{\mathrm{S}}(Q) = \sum_l c_l \overline{b_l^2} = \left\langle \overline{b^2} \right\rangle_{\mathrm{av}}, \tag{5.22}$$

in which $c_l = N_l/N$ is the atomic fraction for element l, and $\langle \overline{b^2} \rangle_{\mathrm{av}}$ is the average squared scattering length for the sample (i.e., a weighted average over all the elements in the sample). The average scattering cross-section per atom is thus $\sigma_{\mathrm{scatt}} = 4\pi \langle \overline{b^2} \rangle_{\mathrm{av}}$. The distinct scattering is given by

$$i^{\mathrm{N}}(Q) = \sum_{l,l'} \bar{b}_l \bar{b}_{l'} \sum_{\substack{j=1 \\ j \neq k}}^{N_l} \sum_{k=1}^{N_{l'}} \frac{1}{N} \frac{\sin(QR_{jk})}{QR_{jk}}, \tag{5.23}$$

where the l and l' summations are over the elements in the sample (e.g., for $PbO\text{-}SiO_2$, l = Pb, Si, O). The j (or k) summations are then over all the N_l (or $N_{l'}$) atoms of element l (or l'), excluding terms where j and k refer to the same atom.

In Eq. 5.21 the differential cross-section, $I^{\mathrm{N}}(Q)$, is separated into two parts, the distinct and self scattering; the distinct scattering is an interference term which contains structural information about the interatomic distances in the sample, whilst the self scattering is essentially a background which does not contain structural information. In order to extract structural information about the sample it is necessary to perform a satisfactory subtraction of the self scattering from the measured diffraction data.

The separation into distinct and self terms arises naturally in diffraction theory, and is useful for the study of glass structure, and hence this is the formalism that is used in this chapter. However, there is an alternative formalism, in terms of coherent and incoherent scattering, which is also widely used. By the algebraic trick of adding and

subtracting a $\sum_j \bar{b}_j^2 \langle j,j \rangle$ term to Eq. 5.19, the differential cross-section may be separated into its coherent and incoherent parts.

$$I^{\mathrm{N}}(Q) = \sum_{l,l'} \bar{b}_l \bar{b}_{l'} \sum_{j=1}^{N_l} \sum_{k=1}^{N_{l'}} \frac{1}{N} \frac{\sin(QR_{jk})}{QR_{jk}} + \left(\left\langle \overline{b^2} \right\rangle_{\mathrm{av}} - \left\langle \bar{b}^2 \right\rangle_{\mathrm{av}} \right), \tag{5.24}$$

in which self terms ($j = k$) are now included in the summation. The incoherent cross-section of the sample is

$$\sigma_{\mathrm{inc}} = 4\pi \left(\left\langle \overline{b^2} \right\rangle_{\mathrm{av}} - \left\langle \bar{b}^2 \right\rangle_{\mathrm{av}} \right), \tag{5.25}$$

in which $\langle \bar{b}^2 \rangle_{\mathrm{av}} = \sum_l c_l \bar{b}_l^{\,2}$, and $\sigma_{\mathrm{coh}} = 4\pi \langle \bar{b}^2 \rangle_{\mathrm{av}}$ is the average coherent scattering cross-section for the sample. The interpretation of the coherent contribution to the differential cross-section is that this is what would be measured from a sample for which all nuclei of element l had a scattering length of $\bar{b}_l$. The coherent contribution to the differential cross-section contains the interference information relating to the positions of atoms in the sample. For most elements the incoherent cross-section is relatively small, but a notable exception to this is hydrogen for which the incoherent cross-section is very large, so that the measured experimental diffraction pattern is dominated by the incoherent contribution, and this can be a severe problem as is discussed in Section 5.4.6.2.

Figure 5.8 illustrates how the differential cross-section, $I^{\mathrm{N}}(Q)$, can be separated into either distinct and self contributions, or coherent and incoherent contributions. Experimental data for liquid CCl_4 are used for this illustration because this compound has a larger incoherent cross-section than most materials, due to the fact that chlorine has two isotopes with very different scattering lengths, and both isotopes have a significant abundance. The average level of $I^{\mathrm{N}}(Q)$ is given by the self scattering, and the distinct scattering, $i^{\mathrm{N}}(Q)$, oscillates about this average level; this is an important underlying principle for the treatment of experimental data.

As shown by Eq. 5.23, the distinct scattering contains information about the structure of the sample, in the form of the interatomic distances, weighted according to the coherent neutron scattering lengths of the atoms. The magnitude of the coherent scattering length of an element is determined by the strong interaction between the nucleus and the neutron, and hence it varies haphazardly across the periodic table, as shown in Figure 5.9. This behavior leads to certain advantages for ND, compared to XRD. For example, XRD is not good at distinguishing elements which are adjacent in the periodic table, because their X-ray scattering powers (i.e., their atomic numbers) are almost the same. Also, ND is much better than XRD for determining the position of oxygen atoms, since oxygen scatters weakly for XRD, but relatively strongly for ND.

5.3.6 Atomic Vibrations

5.3.6.1 The Effect of Inelasticity on the Self Scattering An important stage in the analysis of ND data is to obtain the distinct scattering, $i^{\mathrm{N}}(Q)$, by subtracting

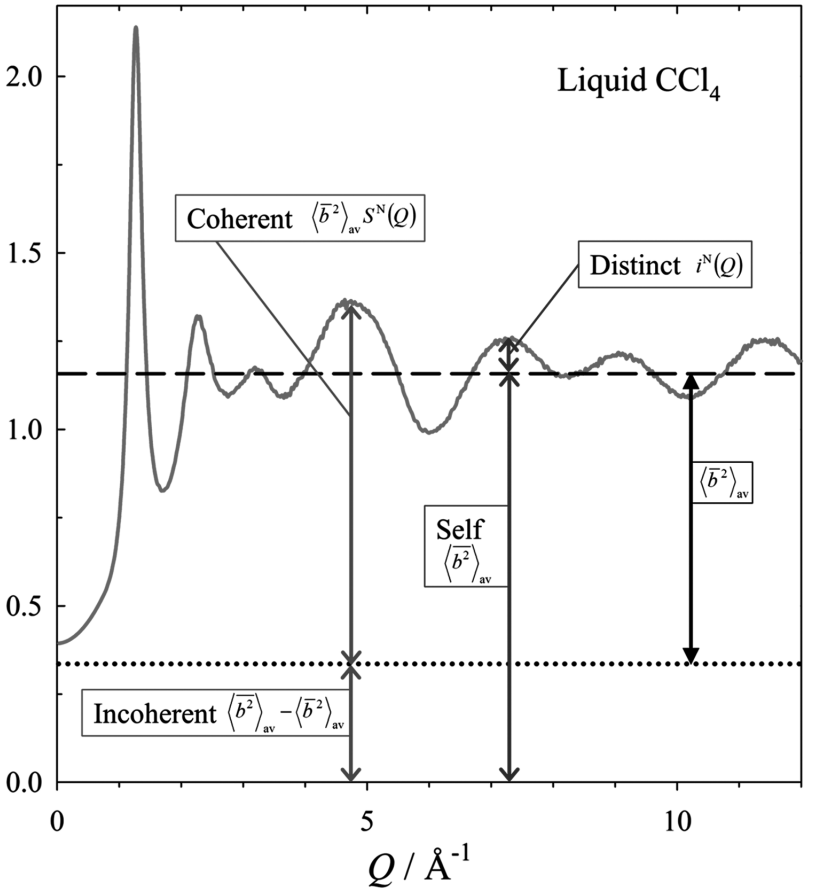

Figure 5.8. The lower Q region of the corrected differential cross-section, $I^N(Q)$, for liquid CCl_4, showing how it can be separated into either self and distinct contributions, or into coherent and incoherent contributions.

the self scattering from the measured differential cross-section (see Figure 5.10). It appears from Eq. 5.21 that this should be simple, since in the static approximation the self scattering is a constant, $I^S(Q) = \sum_l c_l \overline{b_l^2}$, independent of Q. However, this is not the case; in practice the effect of inelastic scattering of neutrons on $I^S(Q)$ must be taken into account.

In the static approximation it is assumed that neutrons do not exchange energy with the sample, but actually a scattered neutron may have a non-zero energy transfer

$$E = E_i - E_f, \tag{5.26}$$

where E_i and E_f are the neutron energy before and after scattering. A non-zero value of E corresponds to inelastic scattering. The effect of inelastic scattering for diffraction

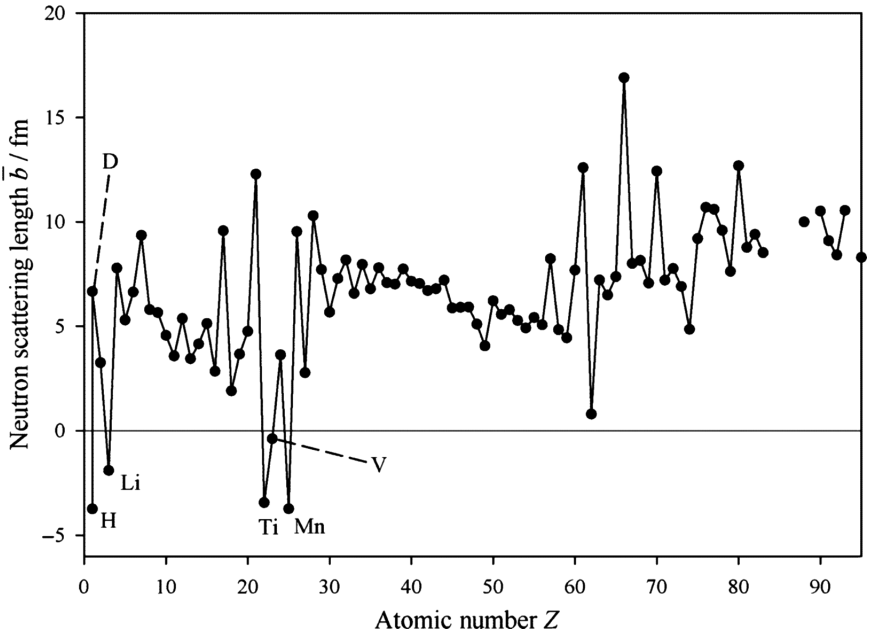

Figure 5.9. The bound atom coherent neutron scattering length of the natural elements (and deuterium) as a function of atomic number [32]. Elements with a negative scattering length (and deuterium) are indicated by the element symbol.

was first considered by Placzek [8] (who showed that, fortunately, to first order, there is no inelasticity effect for the distinct scattering, $i^{\mathrm{N}}(Q)$), and it is still widely known as "the Placzek correction". The effect can be calculated within an approximation (first derived for a reactor diffractometer by Johnson et al. [5] and for a T-O-F diffractometer by Wright [9] and later by Howe et al. [10]), and a full treatment of this topic is beyond the scope of this chapter; the reader should consult more advanced texts for full details [11]. However, the salient points can be understood from the following equation;

$$I^{\mathrm{S}}(Q) = \sum_l c_l \overline{b_l^2}(1 - P_l(Q, 2\theta, M_l, T, \varepsilon(E_f), \Phi(E_i))). \tag{5.27}$$

The Placzek correction, P_l, depends on the scattering angle, 2θ, so that the self scattering becomes smaller at higher angles. The correction depends on the sample temperature, T, so that the effect is more severe for a hotter sample. The correction also depends on the masses of the atoms in the sample, so that the effect is more severe for lighter elements. Furthermore, the correction depends on the energy efficiency, $\varepsilon(E)$, of the detector, on the energy distribution of the source, $\Phi(E)$, and on the Q-E locus for neutrons detected with the same apparent momentum transfer. These last three factors all depend on the parameters of the diffractometer, and in particular the inelasticity effect has

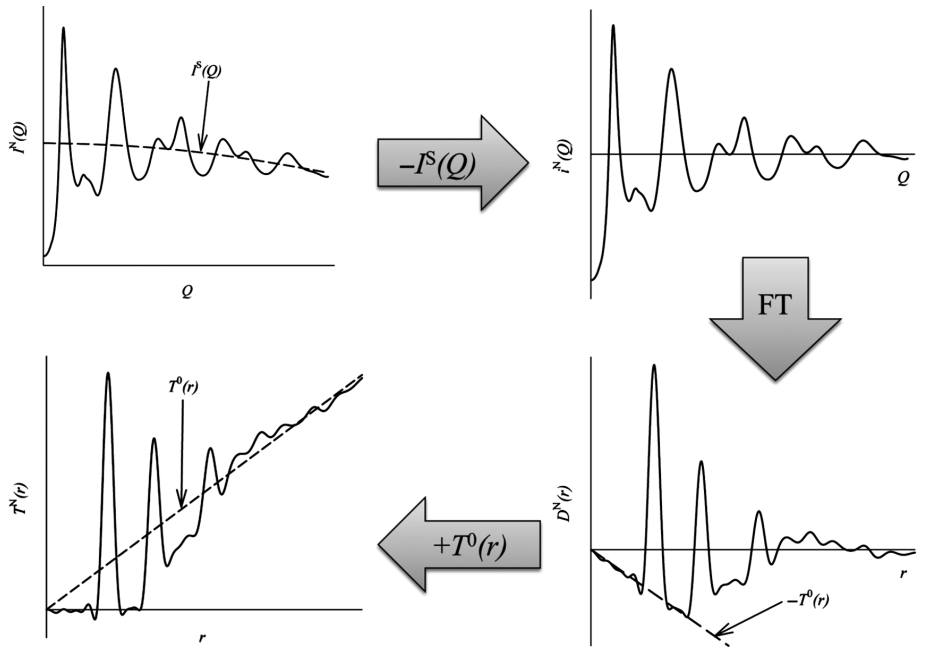

Figure 5.10. Key stages in the analysis of (corrected and normalized) neutron diffraction data from a glass: subtraction of self scattering, Fourier transformation, addition of $T^0(r)$.

marked differences between reactor and T-O-F diffractometers. Figures 5.11 and 5.12 show the corrected differential cross-section, $I^N(Q)$, for B_2O_3 glass, as measured on the D4 [12] and GEM [13] diffractometers, respectively, together with the calculated self scattering, $I^S(Q)$. For a reactor diffractometer (Figure 5.11), the main effect is that the self scattering becomes smaller at higher angle (i.e., at higher Q). For a T-O-F diffractometer (Figure 5.12), the self scattering also becomes smaller at higher angle (i.e., the self scattering is smaller for detector banks at higher angle). However, for a T-O-F diffractometer the Q-dependence of the self scattering is different, with a very strong increase at the lowest Q, followed by a minimum at intermediate values of Q, arising from the energy distribution of the neutrons from the source, which is characteristic of the temperature of the moderator. For the analysis of T-O-F diffraction data, it is important to note that, because the Placzek correction (see Eq. 5.27) depends on scattering angle, 2θ, this correction must be made before data from different scattering angles are combined to form the final determination of the distinct scattering, $i^N(Q)$.

5.3.6.2 The Effect of Atomic Vibrations on Diffraction The Debye equation in the form given above (Eq. 5.23) does not explicitly include the effect of atomic

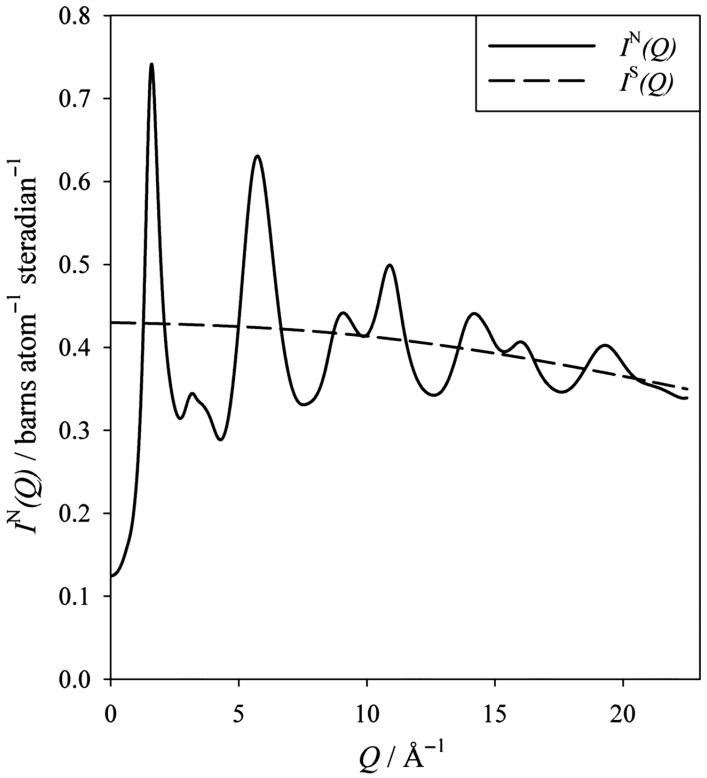

Figure 5.11. The differential cross-section of B_2O_3 glass, $I^N(Q)$ (corrected and normalized), measured on the D4 diffractometer, together with the calculated self scattering [12].

motions, but these may be included as follows:

$$i^{\mathrm{N}}(Q) = \sum_{l,l'} i^{\mathrm{N}}_{ll'}(Q) = \sum_{l,l'} c_l c_{l'} \bar{b}_l \bar{b}_{l'} (S_{ll'}(Q) - 1), \tag{5.28}$$

$$i^{\mathrm{N}}_{ll'}(Q) = \bar{b}_l \bar{b}_{l'} \frac{1}{N} \sum_{j=1}^{N_l} \sum_{\substack{k=1 \\ j \neq k}}^{N_{l'}} \exp(-2W_{jk}) \frac{\sin Q\langle R_{jk}\rangle}{Q\langle R_{jk}\rangle}, \tag{5.29}$$

$$2W_{jk} = \frac{Q^2 \left\langle u^2_{jk} \right\rangle}{2}. \tag{5.30}$$

where $\langle R_{jk}\rangle$ is the mean distance between the pair of atoms j and k, and $\langle u^2_{jk}\rangle$ is the mean square variation in the distance between these two atoms. Thus the effect of atomic vibrations is to introduce the Debye–Waller factor, $\exp(-2W_{jk})$, which leads to a reduction (i.e., a damping) of the distinct scattering at higher Q. In Eq. 5.28, the distinct scattering is separated into partial structure factors, $S_{ll'}(Q)$, for each pair of elements, l

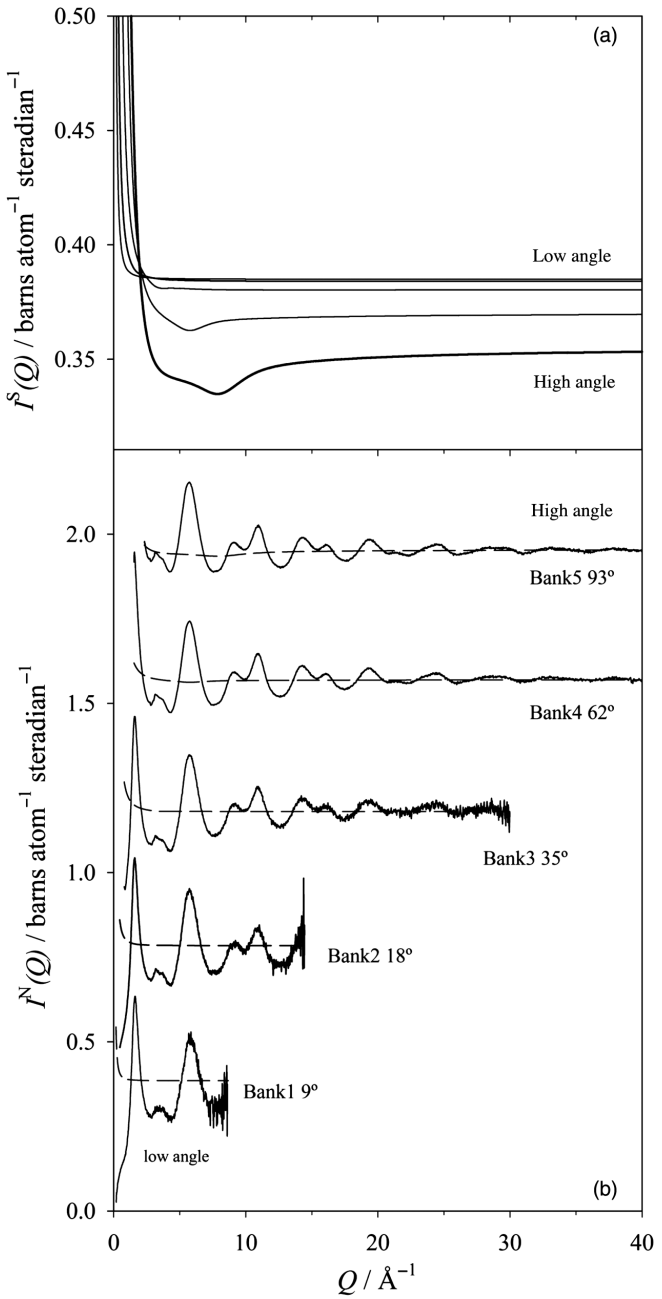

Figure 5.12. (a) The calculated self scattering, $I^S(Q)$, for B_2O_3 glass on the GEM diffractometer. (b) The (corrected and normalized) differential cross-section of B_2O_3 glass, $I^N(Q)$, measured on the GEM diffractometer (continuous line), together with the calculated self scattering (dashed line) [13]. The curves for the different detector banks are shown with vertical offsets for clarity.

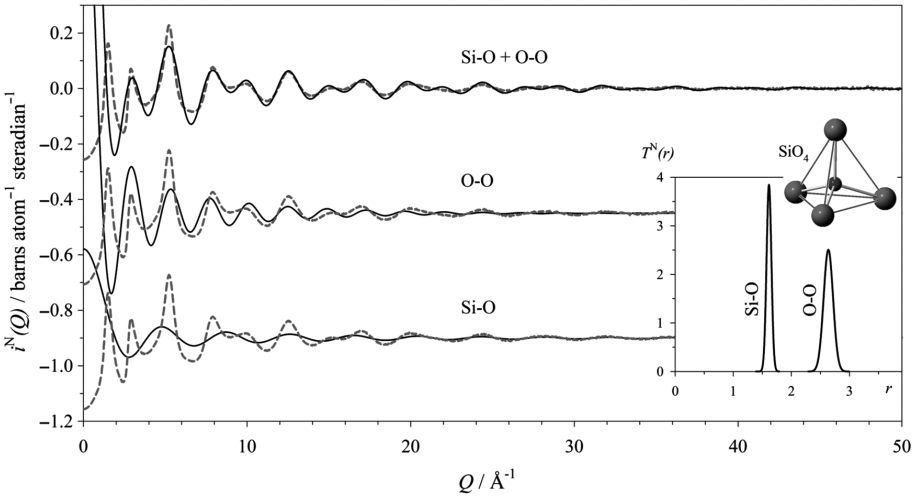

Figure 5.13. The distinct scattering, $i^N(Q)$, for SiO_2 glass (dashed line), together with a Debye equation simulation for an ideal SiO_4 tetrahedron with realistic thermal displacement factors (continuous line). The Si–O and O–O contributions to the simulation are shown (together with the experimental result shown again as a dashed line) with vertical offsets. The inset shows the corresponding correlation function, $T^N(r)$, for the simulation, and a SiO_4 tetrahedron.

and l', in the sample; these are often called Faber–Ziman partial structure factors [14]. Some workers also find it useful to define a total coherent structure factor, $S^N(Q)$, for example by

$$i^N(Q) = (S^N(Q) - 1) \left\langle \bar{b}^2 \right\rangle_{av} . \tag{5.31}$$

Figure 5.13 shows a simple application of Eqs. 5.28 to 30 to simulate the distinct scattering for SiO_2 glass, by calculating the distinct scattering for an ideal SiO_4 tetrahedron (using physically realistic thermal displacement factors $\langle u^2_{SiO} \rangle^{1/2} = 0.041$ Å and $\langle u^2_{OO} \rangle^{1/2}) = 0.081$ Å). For this tetrahedron, there are only two interatomic distances, the bond length $r_{SiO} = 1.614$ Å, and the oxygen–oxygen distance, $r_{OO} = \sqrt{8/3} r_{SiO} = 2.636$ Å. There are thus two simple contributions to the simulation, $i^N_{SiO}(Q)$ and $i^N_{OO}(Q)$, both of which are damped sinc functions, as shown in the lower parts of Figure 5.13. The Si–O distance has a smaller variation, so that it damps less severely to high Q, and hence it is possible to estimate the length of the Si–O bond from the period (ΔQ) of oscillation of $i^N(Q)$ at high Q, according to $r_{SiO} \approx 2\pi/\Delta Q$.

The simulated function in Figure 5.13 gives a reasonably close description of the observed features in the distinct scattering, $i^N(Q)$. Thus the general shape of the distinct scattering for a glass is determined by the basic structural unit. For pairs of atoms which are further apart than those in the basic structural unit, the RMS (root mean square) variation in distance, $\langle u^2_{jk} \rangle^{1/2}$, is relatively large and hence their contribution

is concentrated mainly at lower Q; this is why the simulation in Figure 5.13 is less satisfactory at lower Q.

The Debye equation method of simulating diffraction data can be very powerful, for example for predicting the scattering from extremely small particles (i.e., nanoparticles). However, it rapidly becomes hard to perform the calculation as the model gets bigger, because the number of interatomic distances involved is proportional to N^2.

The Debye–Waller factor defined according to Eq. 5.30 is not exactly the same as used in crystallography. In crystallographic analysis (which is essentially a description of the long range order) the Debye–Waller factor for a pair of atomic sites, d and d', is $\exp(-(W_d + W_{d'}))$, where $W_d = Q^2\langle u_d^2\rangle/2$ and $\langle u_d^2\rangle$ is the mean square displacement of the atom from the site. Thus the crystallographic Debye–Waller factor treats the two sites as independent oscillators, and it is not related to the interatomic distance between two atoms. If two atoms are close together, especially if they are bonded, their thermal motions are highly correlated, with the result that the value of $\langle u_{jk}^2\rangle^{1/2}$ is smaller for short distances $\langle R_{jk}\rangle$ than would be predicted by the crystallographic Debye–Waller factor [15].

Although the Debye equation is able to give a reasonable description of the diffraction pattern (i.e., the distinct scattering), each atomic pair provides a contribution which extends over the full Q-range, and hence the Debye equation does not provide a useful means of separating the contributions arising from different pairs of atoms in the structure. In order to obtain specific information about the different interatomic distances in the glass, it is necessary to adopt a Fourier transform approach, so that a correlation function in real space can be studied.

5.3.7 Real-space Correlation Functions

So far, the diffraction from a glass has been considered in terms of the scattering in reciprocal space, but it is immensely powerful to consider how this may be related to information in real space by means of Fourier transformation.

The simplest correlation function to understand is the radial distribution function (RDF) of a monatomic system, *n(r)*. This may be defined so that *n(r)dr* is the number of atoms inside a spherical shell with radii r and $r+dr$, with an average atom at the center. Figure 5.14 gives a graphical representation of how such functions are related to the atomic structure. The total correlation function, *t(r)*, and pair correlation function, *g(r)*, of the monatomic system may then be defined according to

$$n(r) = rt(r), \tag{5.32}$$

$$t(r) = 4\pi r g(r). \tag{5.33}$$

Very few samples of interest are monatomic; it is important to consider samples containing more than one element, in which case the different scattering lengths of the elements must be taken into account, and this is done by means of partial correlation functions. The partial RDF, $n_{ll'}(r)$, is defined so that $n_{ll'}(r)dr$ is the number of atoms of type l' in a spherical shell $(r,r+dr)$ with an average atom of type l at the center, and there

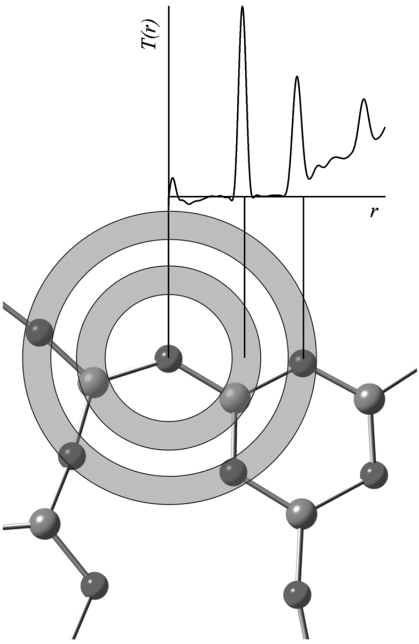

Figure 5.14. The neutron correlation function, $T^{N}(r)$, for B_2O_3 glass [13], together with a fragment of a two-dimensional B_2O_3-like network, showing how the peaks in the correlation function arise from the interatomic distances.

are corresponding partial functions, $t_{ll'}(r)$ and $g_{ll'}(r)$, which are defined in the same way as in Eqs.5.32 and 5.33.

The total correlation function measured in an ND experiment, $T^{N}(r)$, is obtained by Fourier transformation of the distinct scattering,

$$T^{N}(r) = T^{0}(r) + D^{N}(r) = T^{0}(r) + \frac{2}{\pi}\int_{0}^{\infty} Qi^{N}(Q)\, M(Q) \sin(rQ)\, dQ\,, \qquad (5.34)$$

where $D^{N}(r)$ is the differential correlation function, $M(Q)$ is a modification function introduced to take account of the finite Q-range of the experimental data (see Section 5.4.2.2), and the average density contribution is defined by

$$T^{0}(r) = 4\pi r g^{0} \left\langle \bar{b} \right\rangle_{\text{av}}^{2}, \qquad (5.35)$$

where $g^0 = N/V$ is the macroscopic atom number density, and $\langle \bar{b} \rangle_{\text{av}} = \sum_l c_l \bar{b}_l$ is the average coherent neutron scattering length for the sample. $D^{N}(r)$ is the function which is obtained directly by Fourier transformation of the distinct scattering, and it arises from deviations of the scattering length density from the average.

The total neutron correlation function is related to the partial functions according to

$$T^{\mathrm{N}}(r) = \sum_{l,l'} c_l \bar{b}_l \bar{b}_{l'} t_{ll'}(r). \tag{5.36}$$

It is of great importance to note that the l–l' and l'–l partial correlation functions are not independent, but are related according to

$$t_{l'l}(r) = t_{ll'}(r)\,\frac{c_l}{c_{l'}}. \tag{5.37}$$

A simple way to understand this point is to consider that the number of Si–O bonds in a silicate sample is equal to the number of O–Si bonds; hence the ratio of coordination numbers depends on the relative numbers of the two types of atom,

$$n_{\mathrm{OSi}} = n_{\mathrm{SiO}}\frac{c_{\mathrm{Si}}}{c_{\mathrm{O}}}, \tag{5.38}$$

that is, the coordination numbers n_{SiO} and n_{OSi} are not independent.

Figure 5.15 shows a measurement for GeO_2 glass [16] of the various neutron correlation functions introduced above. The total neutron correlation function, $T^{\mathrm{N}}(r)$, is the most widely favoured of these functions for use in studying glass; for example, its use has often been advocated by Wright [3]. The RDF was used extensively in the past, such as in the pioneering XRD work of Warren [17], but is not widely used now. It has the advantage of suppressing artefacts at low r, but also suppresses the nearest neighbor peak(s), and arguably these are the most important peaks in the measured correlation function. The pair correlation function, $g^{\mathrm{N}}(r)$, is more commonly favoured in studies of liquid structure [18]. It does not suppress the nearest neighbor peak(s), but it does suppress the longer range peaks (which are not so significant in a liquid), and it amplifies artifacts at low r. The total correlation function, $T^{\mathrm{N}}(r)$, is the function which arises directly from the Fourier transform in Eq. 5.34 without multiplication/division by a factor r, and it provides a reasonable compromise between suppressing or amplifying both the low r artifacts and the longer range information.

Figure 5.14 shows graphically how the total correlation function is related to the atomic structure for a simple oxide glass. Usually the first peak arises from bond lengths in the basic structural unit (e.g., the B–O bond length in B_2O_3 glass), and this is followed by a peak which arises from the oxygen–oxygen distance in the basic structural unit (e.g., the O–O distance in BO_3 units in pure B_2O_3 glass). The total correlation function can be measured experimentally for any isotropic sample, and Figure 5.16 shows the distinct scattering and $T^{\mathrm{N}}(r)$ for three samples, liquid, glass and crystal, which all have a tetrahedral structural unit. It is striking that the first two peaks, arising from the two distances within the tetrahedron, are similarly well defined in all three phases, that is, the basic structural units in glasses are neither less well defined than in crystals, nor more well defined than in liquids. The differences between the three different phases occur mainly

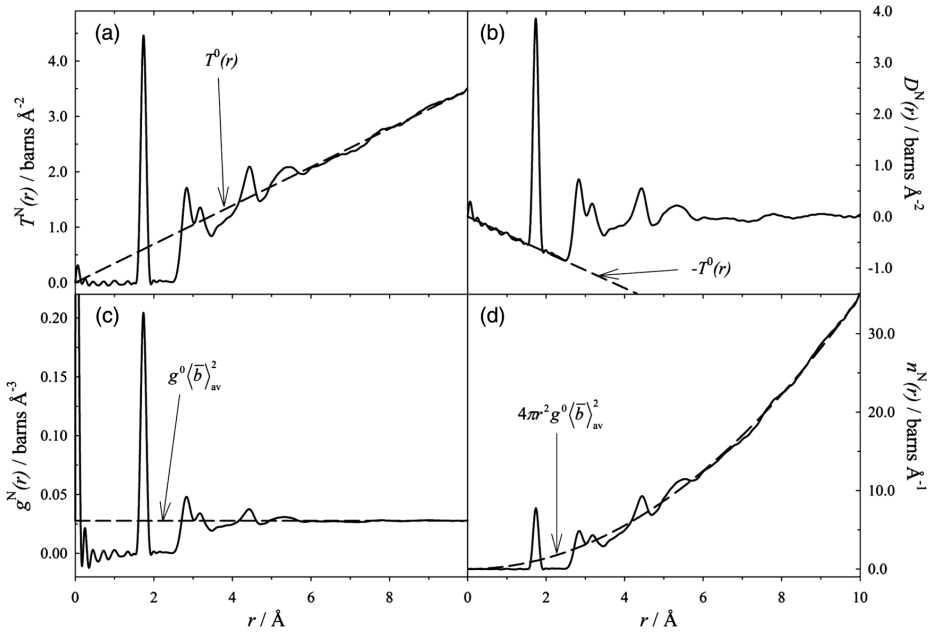

Figure 5.15. Neutron correlation functions for GeO_2 glass [16]: (a) the total correlation function, $T^N(r)$; (b) the differential correlation function, $D^N(r)$; (c) the pair correlation function, $g^N(r)$; and (d) the radial distribution function $n^N(r)$. In each case the experimental result is shown as a continuous line, whilst the relevant average density term is shown as a dashed line.

at longer distance. For the liquid, there is only slight order beyond the structural unit. For the glass there is more order than the liquid in the medium range, whilst the crystal has much greater order at longer range. The experimental approach (i.e., correlation functions) described here was originally developed mostly for the study of glasses and liquids, but in recent years it has increasingly been applied to the study of crystalline structures [19], in which case it is often called *the PDF method* [20] (see Section 5.4.10). The term PDF is an abbreviation for Pair Distribution Function, and this function is equivalent to the differential correlation function, $D^N(r)$, introduced above in Eq. 5.34.

A difficulty of this field, especially for newcomers, is that there is not a generally agreed convention for the exact definition of correlation function or scattering function; different workers may use the same notation for different functions, or different notation for the same function. A detailed discussion of this issue has been given by Keen [21], but here are some guidelines that may be of use in determining exactly what correlation function has been used in a publication:

- What is the long range trend of the correlation function? Is it proportional to r^2, r or a constant (i.e., is the definition $n^N(r)$, $T^N(r)$ or $g^N(r)$)? If the correlation function is non-zero at high r, then the dependence on r should be apparent at

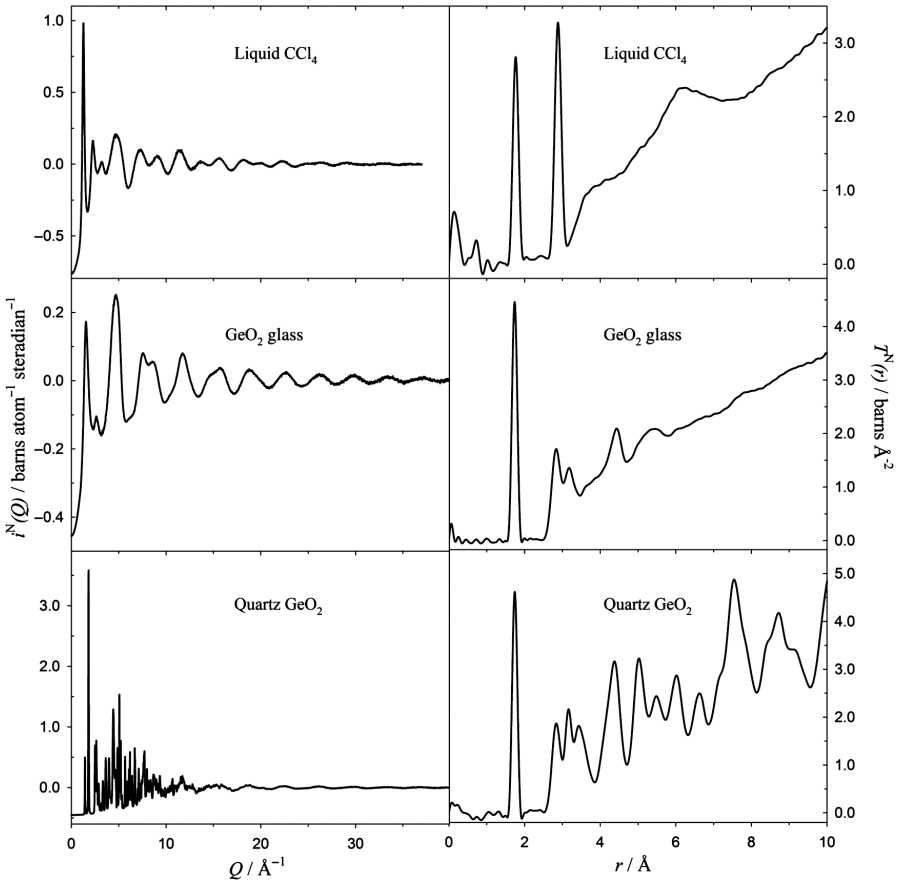

Figure 5.16. The distinct scattering, $i^N(Q)$ (left-hand side), and the neutron correlation function, $T^N(r)$ (right-hand side), for liquid carbon tetrachloride, GeO_2 glass, and GeO_2 in its quartz crystalline form [16]. See plate section for a color version of this figure.

high r (as in Figure 5.15a, c and d). If the correlation function oscillates about zero (as in Figure 5.15b), then the dependence on r should be apparent from the low r region.

- Has the average density contribution been subtracted, to yield a correlation function which oscillates about zero? (e.g., in Figure 5.15b, $T^0(r)$ has been subtracted to yield the differential correlation function, $D^N(r)$).
- In this chapter, a consistent normalization to one atom is used (i.e., the equations involve a factor $1/N$, where N is the total number of atoms in the sample). Another normalization (often used by Wright [3]) is in terms of a composition unit (for SiO_2 this involves three atoms, and hence the correlation function is three times larger). An alternative approach is to define the correlation functions so that they oscillate about one, and this is more popular in the study of liquid structure

[18]. The pair correlation function, $g^{\mathrm{N}}(r)$, consistent with the definitions above, oscillates about $g^0\langle\bar{b}\rangle^2_{\mathrm{av}}$, but it oscillates about one if divided by this factor. For a monatomic sample, this normalization is attractive because then the pair correlation function indicates how the local density varies with distance from an average atom. However, for other samples, the situation is not so simple, due to the weighting of each partial contribution by the scattering lengths of a pair of atoms, and so this normalization is less attractive.

In a more complete theory of ND, the pair correlation function is shown to be the distinct van Hove correlation function [22], $g_{ll'}(r) = G^D_{ll'}(r, 0)$, where

$$G^D_{ll'}(\boldsymbol{r}, t) = \frac{1}{N_l} \sum_{\substack{j=1 \\ j\neq k}}^{N_l} \sum_{k=1}^{N_{l'}} \int \left\langle \delta(\boldsymbol{r}' - \boldsymbol{R}_j(0))\delta(\boldsymbol{r}' + \boldsymbol{r} - \boldsymbol{R}_k(t)) \right\rangle d\boldsymbol{r}'. \tag{5.39}$$

$\boldsymbol{R}_j(t)$ represents the position of atom j at time t, and thus $G^D_{ll'}(\boldsymbol{r}, t)$ represents the correlation between atoms of type l at time zero with atoms of type l' at later time t. Thus the exact interpretation of total diffraction is that it yields an instantaneous "snapshot" of the interatomic vectors.

The Fourier transformation of experimental data (Eq. 5.34) is in practice performed numerically by software, and for equally spaced data this can be done efficiently by use of Filon's quadrature [23]. Fast Fourier transform techniques can also be used for the purpose; at first sight these may appear unsuitable, due to the requirement for 2^n points, but this requirement can be met by padding with zeroes at high Q. For unequally spaced data numerical integration methods can be used. The numerical evaluation of the Fourier transform in Eq. 5.34 essentially involves a weighted sum over the measured intensity points, $y_i \pm e_i$, and Toby and Egami [24] have shown that the error on the Fourier transform can also be evaluated by a suitable summation of the intensity errors, e_i. To a reasonable approximation, their result can be simplified for equally spaced data to give the error on $D(r)$ as

$$\sigma_{D(r)} \approx \frac{\Delta Q}{\pi} \left(2 \sum_i e_i^2 \right)^{1/2}, \tag{5.40}$$

where ΔQ is the spacing between the intensity points. It is also possible to derive the correlation function using inverse methods [25]. This involves having a trial real-space correlation function, comparing its Fourier transform with the experimental data in Q space, and adjusting the real-space correlation function so that the agreement in Q space is optimized. An advantage of inverse methods is that the effect of Q-resolution can readily be incorporated. On the other hand, it is not clear how to evaluate the errors on a correlation function produced in this way. More importantly, for inverse methods, the mathematical description of the real-space resolution function is not clear, which is a disadvantage for peak-fitting methods of peak deconvolution (see Section 5.4.3), and for

differentiating between small genuine peaks and artifacts (such as termination ripples, see Section 5.4.2.2).

5.4 THE APPLICATION OF NEUTRON DIFFRACTION TO STUDIES OF GLASS STRUCTURE

5.4.1 Experimental Corrections

ND has the advantage that the scattering length, $\bar{b}$, is a constant which is independent of Q (unlike X-ray or electron diffraction, which involve a Q-dependent form factor), with the result that the diffraction pattern can be measured reliably to very high Q, with a reliable normalization between the low and high Q regions. Furthermore, because the interaction between the neutron and matter is relatively weak, experimental corrections can often be performed relatively reliably. As a consequence of these advantages, highly reliable results may be obtained, leading to trustworthy determinations of coordination numbers, distributions of bond lengths, etc.

The Fourier transformation of the experimental data required to obtain the correlation function (see Eq. 5.34) involves integrations of the distinct scattering, $i^{N}(Q)$, over the full Q-range that has been measured. For this to be reliable, it is essential that the different regions of $i^{N}(Q)$ are correctly weighted relative to each other, and for this to be achieved it is necessary to correct the data for all the various experimental effects that cause the data to have any kind of Q-dependent suppression/amplification. Furthermore, ND has the ability to produce results that are accurately normalized on an absolute scale, and this leads to an ability to provide accurate coordination numbers. However, for reliable absolute normalization to be achieved, it is necessary to perform a full set of experimental corrections on the data for the following effects [26]:

- *Detector dead-time*. After a detector chain has counted a neutron, it is unable to count another neutron for a period of time. Thus more intense regions of the signal are suppressed, and it is necessary to correct for this effect.
- *Subtraction of backgrounds*. It is necessary to subtract the contribution to the scattering that arises from general backgrounds, and from the sample container.
- *Absorption*. This is when a neutron is permanently absorbed by a nucleus.
- *Attenuation*. This is when the incident and scattered flux of neutrons are reduced due to further scattering events.
- *Multiple scattering*. When neutrons are scattered more than once, this is called multiple scattering. Multiply scattered neutrons are removed from the incident and scattered beams, as considered by the theory described above, but they are still detected, and hence they lead to a further 'background' signal which must be subtracted.

In principle, these effects (apart from multiple scattering) are relatively simple to understand and account for. For example, the effects of absorption and attenuation can be calculated by means of a generalization of Eq. 5.15, involving an integration over all

possible neutron paths through the sample. However, in practice the various absorption and scattering events are all interrelated [27]; for example, the multiple scattering from the sample may be absorbed by the container, the single scattering from the container may be multiply scattered by the sample, etc. Therefore the evaluation of a full set of corrections is a complex and convoluted process, and sophisticated software is required. Perhaps the most complete and reliable software currently available for this process is Soper's GudrunN program [28], which is available on the internet [29].

Although it is possible to correct the experimental data for all of the effects outlined above, it is best to use an experimental setup in which they are made as small as possible. A useful rule of thumb for diffraction is that the sample should not scatter more than 5% of the incident beam. Most samples are available in the form of a powder or coarse grains, in which case it is essential to use a sample container, and this should be designed so that the container scattering is minimized. Sometimes it is possible to make a glass sample in the form of a cylindrical rod, in which case a container is not required, and this is the ideal experimental setup.

As is apparent from Figure 5.9, vanadium has a smaller coherent neutron scattering length than any other element. Thus the scattering from vanadium is almost entirely incoherent (see Eqs.5.24 and 5.25), with the consequence that the Bragg peaks observed from a sample of pure vanadium metal are extremely small. Thus vanadium plays a special role in neutron scattering; for example, vanadium is often used to make sample containers because of its very small Bragg peaks. Perhaps the best sample containers for ND on glasses are cylinders made of thin vanadium foil, say 25 or 40 μm in thickness, because this minimizes the container scattering which must be subtracted in the corrections process. Another special metal for neutron scattering is $Ti_{62}Zr_{38}$ alloy which has an average coherent neutron scattering length of zero, and hence is a null alloy with no Bragg peaks [30]. It is possible to make a null alloy in this way, firstly because the two elements concerned have coherent scattering lengths of opposite sign (as shown in Figure 5.9, a few elements, such as titanium, have negative scattering lengths), and secondly because the Ti-Zr system forms a substitutional solid solution. $Ti_{62}Zr_{38}$ alloy is useful for making sample containers for use with demanding sample environment equipment, such as is used for high pressure. However, it suffers from the disadvantages that it is not available as a thin foil, and its diffraction pattern has diffuse scattering due to local order.

Another important use of vanadium, due to its mostly incoherent scattering, is as a calibration standard, which can be expressed simply by the following equation:

$$\text{Normalized sample spectrum} = \left(\frac{\text{sample} - \text{empty container background}}{\text{vanadium} - \text{background}} \right). \tag{5.41}$$

In an ND experiment on a glass it is normal to also measure the diffraction pattern of a vanadium standard (either a cylinder if the detectors cover a wide angular range, or a flat plate if the detectors are all at low scattering angles), so that this normalization can be performed. This provides correct inter-normalization of results from different detectors, allows the corrected differential cross-section to be normalized on an absolute scale

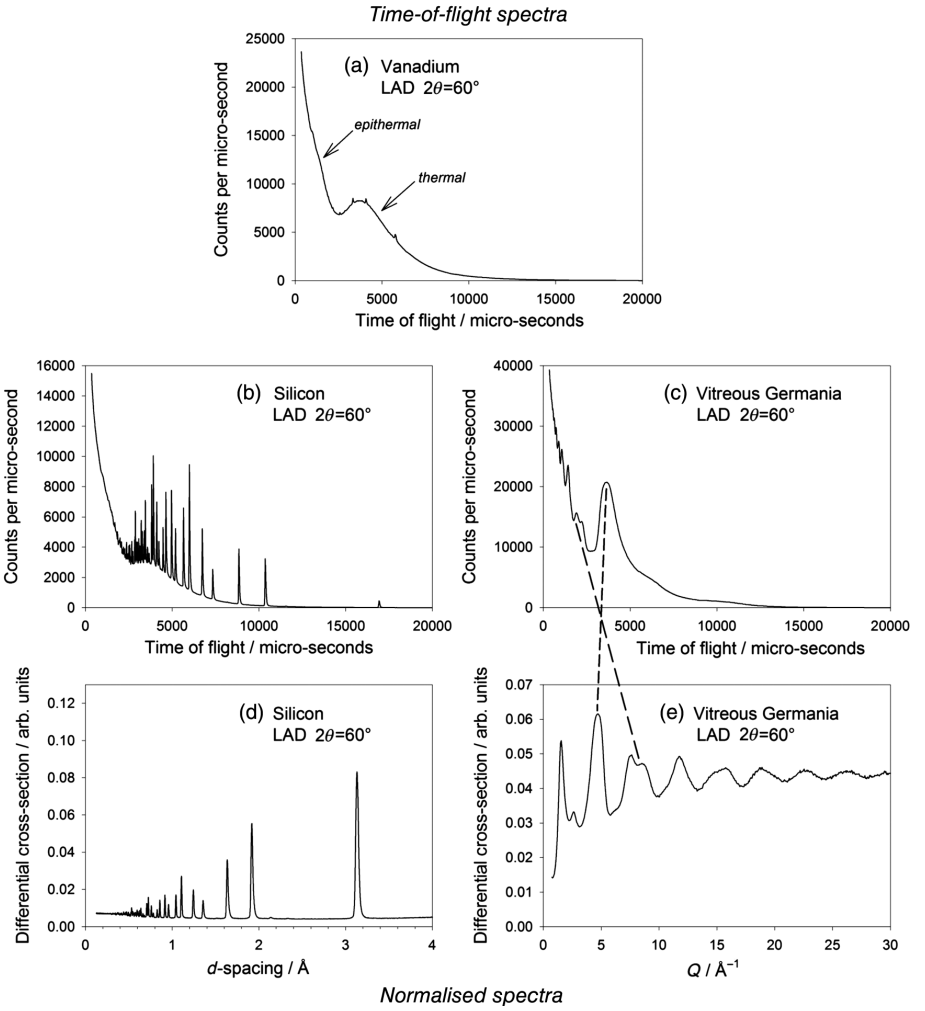

Figure 5.17. Time-of-flight spectra for (a) vanadium; (b) polycrystalline silicon; and (c) GeO_2 glass. Also shown are the normalized spectra for (d) polycrystalline silicon and (e) GeO_2 glass.

(since the differential cross-section of vanadium can be calculated according to Eqs.5.24 and 5.25, using the known cross-section, σ_{inc}, and since $\bar{b}$ for vanadium is almost zero, see Figure 5.9), and for a pulsed source diffractometer allows the flux distribution, $\Phi(\lambda)$, arising from the moderator to be normalized out. Figure 5.17 illustrates the effect of flux normalization for pulsed diffraction data, using data from the former LAD diffractometer. The vanadium T-O-F spectrum is closely related to the flux distribution $\Phi(\lambda)$ arising from the moderator. The upturn in $\Phi(\lambda)$ at low times is due to high energy epithermal neutrons whilst the broad peak at intermediate times is the peak of a Maxwellian distribution whose position depends on the moderator temperature (c.f. Eq. 5.4).

TABLE 5.2. Absorption cross-sections of natural elements for the 10 most absorbing elements and some other elements of interest [32].

Element	B	Cd	In	Sm	Eu	Gd	Dy
$\sigma_{abs}(2200\ ms^{-1})$/barns	767	2520	193.8	5922	4530	49700	994
Element	Ir	Hg	Pa	O	Si	Cl	Ge
$\sigma_{abs}(2200\ ms^{-1})$/barns	425	372.3	200.6	0.00019	0.171	33.5	2.2

For values of r less than the shortest interatomic distance in the glass, the total correlation function, $T^N(r)$, should ideally be equal to zero. However, as shown in Figures 5.10, 5.14, 5.15 and 5.16, real experimental results are not identically zero in this region. Firstly, there are Fourier ripples and experimental noise in this region. Secondly, an unphysical peak is often observed at a short distance in the range below 1 Å, which arises because of imperfections in the experimental corrections. Most corrections change relatively slowly in Q space, compared to the genuine experimental information, and hence inadequacies in the corrections give rise to the unphysical peak at low r. As Wright has advocated [31], the behavior of the low r region of an experimental correlation function can be used to indicate how well the experimental corrections have been performed. Nevertheless, there are inverse methods of obtaining the correlation function [25], which usually involve setting the correlation function to zero below a minimum distance, in which case it is not possible to determine the quality of the corrections from the low r region.

For neutron energies in the thermal region (i.e., for T of order 300 K or lower in Eq. 5.4), many nuclei have an absorption cross-section known as a "1/v cross-section", which means that it is proportional to the neutron wavelength; $\sigma_{abs}(\lambda) = \lambda\sigma_0$. For this reason, absorption cross-sections are conventionally quoted for a neutron speed of 2200 ms^{-1}, and Table 5.2 gives the absorption cross-sections at this speed for the 10 most absorbing natural elements, together with a few other relevant elements. As a rule of thumb, if the average absorption cross-section for a sample is of order 1000 barns or greater, then absorption is too large for it to be feasible to measure a useful diffraction pattern. On the other hand, if the average absorption cross-section is of order 100 barns or less, it is possible to obtain a meaningful diffraction pattern which can be corrected successfully. For example, chlorine has a significant absorption cross-section, and thus the correlation function for liquid CCl_4 shown in Figure 5.16 is relatively noisy at low r, due to the significant correction for absorption. Boron is an important element in the glass field, but samples containing higher concentrations of natural boron are too absorbing for useful ND results to be obtained; for example, if a B_2O_3 sample containing natural boron is used, it may not be possible to observe any scattered neutrons, due to the high absorption. However, the isotopes of boron are available at relatively low cost, and hence it is normal to make samples using highly enriched ^{11}B ($\sigma_{abs}(^{10}B) = 3835$ barns, $\sigma_{abs}(^{11}B) = 0.0055$ barns [32]). Boron is also widely used as a shielding material in neutron diffractometers, usually in the form of boron carbide or boron nitride. Cadmium and gadolinium are also widely used for shielding, but they are of more limited benefit at a pulsed neutron source, because they are virtually transparent to higher energy neutrons.

5.4.2 Resolution

5.4.2.1 Reciprocal-space Resolution As shown in Figure 5.16, the features in the ND pattern of a glass are much broader than the Bragg peaks observed in the diffraction pattern of a crystalline powder. The glass diffraction features are thus much broader than the reciprocal-space resolution of a typical neutron diffractometer, and this can give the impression that the Q-resolution is not an important effect when studying glasses; this is not correct. Grimley et al. [33] have given the following simple consideration of the effect of Q-resolution, which has been confirmed by other more sophisticated approaches [24,25,34,35]. The measured diffraction pattern is a convolution of the ideal diffraction pattern (i.e., measured with perfect resolution) with the resolution function. According to the convolution theorem, the measured correlation function is then the product of the ideal correlation function with the Fourier transform of the resolution function. A simple description of the resolution function is a Gaussian centered at the origin, and hence in real space this corresponds to another Gaussian centered at the origin. In conclusion, this shows that the effect of Q-resolution is that the measured differential correlation function, $D^{\mathrm{N}}(r)$, becomes increasingly damped at higher r. The coordination numbers determined from ND are normally slightly below the expected value (e.g., for SiO_2 glass a value of 3.9 has been obtained by ND [5], and this is typical, whereas the expected value for this tetrahedral glass is four), and this can be ascribed to the damping of the peaks in the correlation function that arises from the Q-resolution. Nevertheless, for a modern diffractometer with high Q-resolution, coordination numbers closer to the ideal values tend to be measured, see Section 5.4.3.

5.4.2.2 Real-space Resolution The Fourier transform in Eq. 5.34 requires that the distinct scattering, $i^{\mathrm{N}}(Q)$, is known to infinitely large values of Q, but in practice it is only possible to measure experimental data up to some finite value, $Q_{\max}$. If the Fourier transform is calculated from the experimental data with a sharp cut-off at $Q_{\max}$, then the resultant correlation function has significant termination ripples, which can easily be mistaken for real features (e.g., see Figure 5.18c). Hence it is common [36] to multiply the distinct scattering by a modification function, $M(Q)$, which is chosen so as to reduce the termination ripples, though at the expense of some loss of resolution in real space. The most commonly used modification function is the Lorch function [37], defined as follows:

$$M_{\mathrm{Lorch}}(Q) = \frac{\sin(\Delta r Q)}{\Delta r Q} \tag{5.42}$$

$$M_{\mathrm{Lorch}}(Q) = 0 \quad Q > Q_{\max}.$$

where delta-r=pi/$Q_{\max}$

The use of the Lorch function reduces the termination ripples to a very large extent. (Indeed with the high $Q_{\max}$ of pulsed ND, the effect of thermal motion is often to entirely remove the termination ripples from the correlation function). However, this gain is achieved at the expense of some loss of resolution, with a full width at half maximum (FWHM) $\Delta r_{\mathrm{Lorch}} = 5.437/Q_{\max}$. If the Fourier transform is performed without a

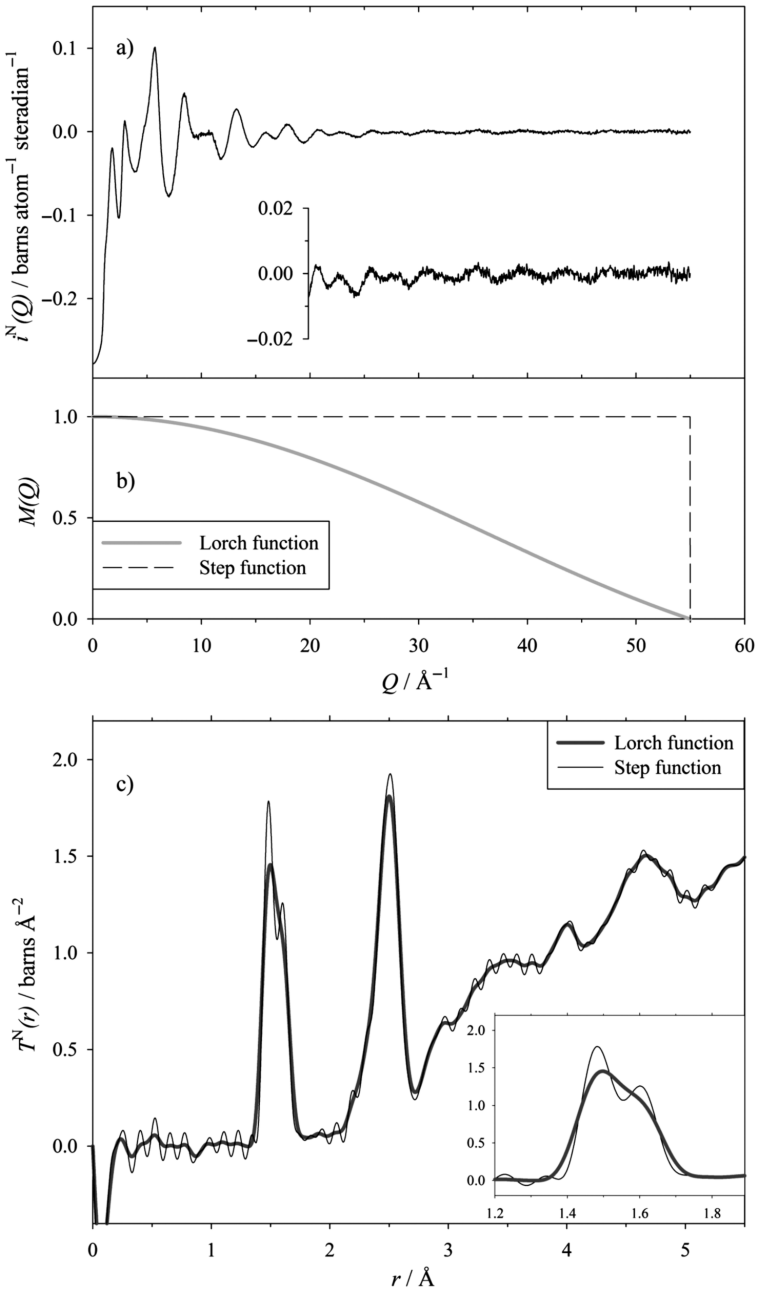

Figure 5.18. Neutron diffraction results for $2CaO{\cdot}Na_2O{\cdot}3P_2O_5$ glass [2, 42]. (a) The distinct scattering, $i^N(Q)$, with the high Q region shown in an inset. (b) The step and Lorch modification functions [37] for $Q_{max} = 55Å^{-1}$. (c) The total neutron correlation function, $T^N(r)$, obtained using the two modification functions shown in part (b) with the first peak region shown in an inset.

modification function (i.e., with a "step" modification function which equals unity for $Q \leq Q_{\max}$ and is zero for $Q > Q_{\max}$) this yields the best possible real-space resolution, with a FWHM $\Delta r_{\text{step}} = 3.791/Q_{\max}$, but at the expense of relatively large termination ripples on either side of a real peak in the correlation function, $T^{\text{N}}(r)$. In earlier work, [38] a pseudo Debye-Waller factor, $\exp(-\alpha^2 Q^2)$ (see Eqs.5.29 and 5.30), with an arbitrary 'thermal factor' α, was used as a modification function, but this reduces the termination ripples less than with the use of the Lorch function. Occasionally other modification functions have been proposed [39, 40], but currently the use of the Lorch function is pre-eminent [41].

The high energy neutrons which are available only for an accelerator source (see Section 5.2.3.2) make it possible to measure diffraction patterns to higher values of $Q_{\max}$ than is possible for a reactor source, so that a narrower real-space resolution width, Δr, can be obtained. For example, Figure 5.18a shows the distinct scattering for $2CaO{\cdot}Na_2O{\cdot}3P_2O_5$ glass [2,42]; for phosphate glasses oscillations are often observable to very high momentum transfer [43], and for this glass they can be discerned up to $Q_{\max} = 55\text{Å}^{-1}$, as shown in the inset to the figure. Figure 5.18b shows the Lorch and step modification functions, evaluated for this value of $Q_{\max}$, whilst Figure 5.18c shows the corresponding total correlation neutron functions, $T^{\text{N}}(r)$. The inset to Figure 5.18c shows the detail of the first peak region, for interatomic distances of order 1.5 Å, which are due to P–O bonds. For the step modification function there is a clear splitting into two peaks at 1.4800(6) Å and 1.5977(10) Å, due respectively to bonds to non-bridging and bridging oxygen. The step modification function gives the best possible resolution, but at the cost of significant termination ripples in the correlation function; on the other hand, the Lorch modification function [37] greatly reduces the termination ripples, but at the cost of an increase in the resolution width, so that the two types of P–O bond lead to an asymmetry in the first peak, rather than a clear splitting.

Figure 5.19 shows simulations of the total neutron correlation function for an ideal GeO_4 tetrahedron with bond length $r_{\text{GeO}} = 1.7369$ Å, using physically realistic values for the RMS variation in interatomic distance ($\langle u^2_{\text{GeO}} \rangle^{1/2} = 0.0422$ Å and $\langle u^2_{\text{OO}} \rangle^{1/2} = 0.1005$ Å). The two peaks are due to interatomic distances between Ge–O and O–O atom pairs. The simulations in Figures 5.19a and 5.19b were calculated using the Lorch modification function [37] and values of $Q_{\max}$ that are typical of what can be achieved in an experiment at a good reactor source (24 Å^{-1}) and at an accelerator source (40 Å^{-1}), respectively. The effect of the value of $Q_{\max}$ on the real-space resolution width is evident, but the figure also illustrates how the high values of $Q_{\max}$ available at an accelerator source can virtually remove the termination ripples. This effect occurs if the resolution width, Δr, is not larger than the width which arises from the RMS variation in interatomic distance (which has a FWHM given by $\sqrt{8 \log_e 2}\langle u^2_{jk} \rangle^{1/2} \approx 2.355 \langle u^2_{jk} \rangle^{1/2}$), and often occurs using an accelerator source.

Pulsed ND at an accelerator source has played an important role in investigations of the bond lengths in phosphate glasses, because it is the only experimental technique which has proved able to resolve the difference in the lengths of the two types of P–O bond [43], due to the high values of $Q_{\max}$ ($\sim 50 - 60$ Å^{-1}) which can be achieved. In pure P_2O_5 glass [44], 40% of the oxygen atoms bond to only one phosphorus atom, and they

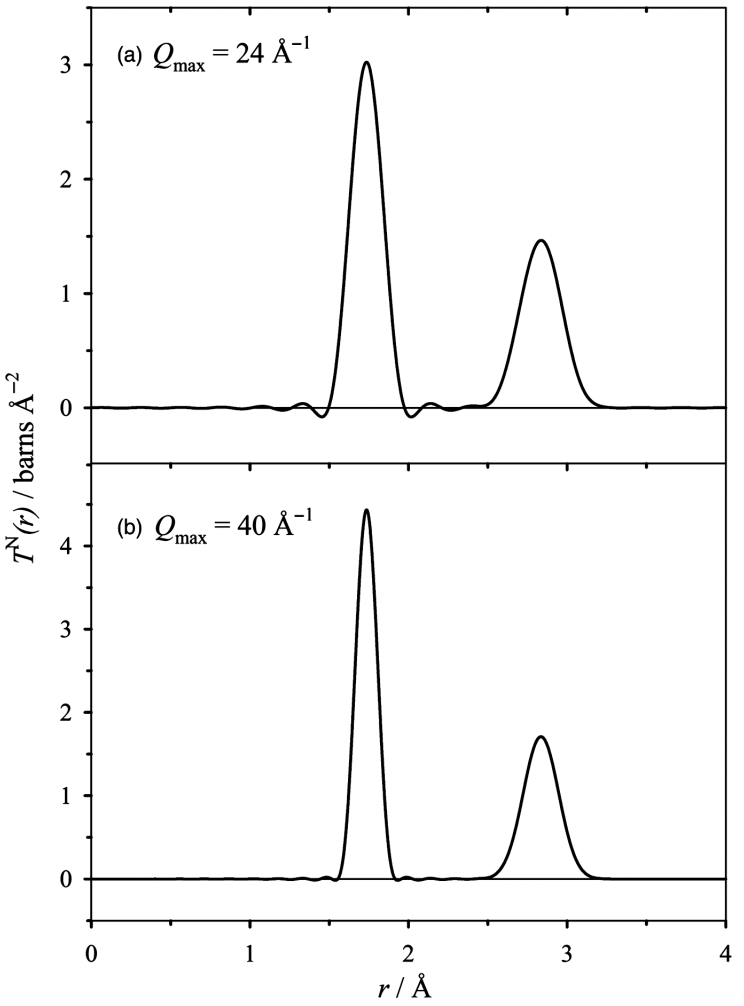

Figure 5.19. Simulation of the total neutron correlation function, $T^N(r)$ (as obtained using the Lorch modification function [37]), for an ideal GeO_4 tetrahedron, showing the effect of maximum momentum transfer, Q_{max}, on real-space resolution and termination ripples. (a) Q_{max} = 24 Å^{-1}, (b) Q_{max} = 40 Å^{-1}.

are described as terminal oxygens (TOs). As modifier oxide is added to P_2O_5, the number of oxygens which are truly terminal (i.e., bonded to only one cation) decreases, whilst the number of non-bridging oxygens (i.e., oxygens which are bonded to one phosphorus and also one or more modifier cations) increases. However, the ND data show that there is no clear distinction between the lengths of the P-TO and P-NBO bonds [43].

In view of the importance of real-space resolution, it is worthwhile to discuss the factors which determine the value of Q_{max}. For a reactor source, Q_{max} is determined

simply by the maximum achievable scattering angle, which is limited at $2\theta = 180°$, and the wavelength, λ, which depends on the parameters of the monochromator and the temperature of the moderator. For an accelerator source, very high energy epithermal neutrons are often available, and in principle experimental data can be measured up to several hundred $Å^{-1}$. However, in practice the useful value of Q_{max} depends on the rate at which the oscillations in the distinct scattering, $i^N(Q)$, diminish at high Q. The width, $\langle u_{jk}^2 \rangle^{1/2}$, of the first peak in the correlation function determines the Debye–Waller factor, $\exp(-Q^2\langle u_{jk}^2 \rangle/2)$, which governs the rate at which the amplitude of the oscillations in $i^N(Q)$ decrease at high Q (see Eqs.5.29 and 5.30). Thus the information in the diffraction pattern diminishes rapidly at higher Q. Also the statistical accuracy of the ND pattern measured at an accelerator source becomes progressively worse as Q increases (as is apparent in Figure 5.12, for example), and furthermore the Q-resolution width at high Q is proportional to Q, so that the diffraction features are increasingly broadened as Q increases. Therefore in practice the value of Q_{max} is the point at which the amplitude of the oscillations in $i^N(Q)$ becomes small in comparison with the size of the error bars on the experimental data. For each sample, the width of the first peak in $T^N(r)$ is different, and hence the useful value of Q_{max} depends on the sample. All of the factors discussed cause it to rapidly become harder to observe the oscillations in $i^N(Q)$ as Q increases, and hence the prospect of measuring ND to significantly higher values of Q_{max} than currently available is very challenging.

5.4.3 Peak Fitting and Integration

The previous section shows how ND can be very powerful for determining bond lengths in glasses, but it can also be very powerful for determining coordination numbers. The concept of coordination number is very important in structural studies of glasses. A simple definition is that the coordination number is the total number of neighbors of a central atom. When this concept is applied to glasses it must be recognized that usually it is only possible to determine the average coordination number (i.e., the coordination number averaged over all relevant central atoms) since different types of atomic site cannot necessarily be differentiated. Coordination numbers for a glass can be determined experimentally from the area under a peak in the correlation function. If a peak in $T^N(r)$ at a distance $r_{ll'}$, due to a pair of elements l–l', has an area $A_{ll'}$, then the corresponding coordination number is given by

$$n_{ll'} = \frac{r_{ll'}A_{ll'}}{(2 - \delta_{ll'})c_l\bar{b}_l\bar{b}_{l'}}. \tag{5.43}$$

where $\delta_{ll'}$ is the Kronecker delta. To determine the coordination number from a peak in $T^N(r)$, it is necessary to identify the pair of elements, l–l', which give rise to the peak, and to determine the area of the peak, $A_{ll'}$, which can be determined either by fitting or

integration. For a discussion of the area of a peak it is necessary to consider the factors which give rise to the broadening of the peak:

1. *Real-space resolution*. This has been discussed in the preceding section, and its effect can be calculated analytically.
2. *Thermal motion of the atoms*. The thermal motion of the atoms gives rise to a broadening of a peak in the correlation function which, in the harmonic approximation, can be described by a Gaussian. Even at very low temperature there is significant thermal broadening due to zero-point motion.
3. *Static disorder*. If there is structural disorder in the interatomic distances then this also gives rise to a broadening of a peak in the correlation function. For example, the two P–O distances in a phosphate glass (e.g., see Figure 5.18c) give rise to a broadening of the first peak in the correlation function. If a peak in the correlation function is asymmetric, then this is definite evidence of static disorder. However, generally speaking, it is not possible to distinguish static disorder from thermal disorder, in which case the RMS variation in interatomic distance has contributions from both effects.

The contribution to the partial correlation function $t_{ll'}(r)$ due to a single interatomic distance r_{jk} with RMS variation in distance $\langle u_{jk}^2 \rangle^{1/2}$ is

$$t_{jk}(r) = \frac{n_{jk}}{r_{jk}\left(2\pi \left\langle u_{jk}^2 \right\rangle\right)^{1/2}} \exp\left(-\frac{(r - r_{jk})^2}{2\left\langle u_{jk}^2 \right\rangle}\right), \tag{5.44}$$

where n_{jk} is the coordination number, that is, the average number of k type atoms around a j type atom. In reciprocal space, this corresponds to

$$i_{jk}(Q) = n_{jk}\bar{b}_j\bar{b}_k \frac{\sin(Qr_{jk})}{Qr_{jk}} \exp\left(-\frac{\left\langle u_{jk}^2 \right\rangle Q^2}{2}\right). \tag{5.45}$$

It is simpler computationally to take the effect of real-space resolution into account by using Eq. 5.45 to calculate the reciprocal-space function, and then to Fourier transform to real space, using the same modification function and value of $Q_{\max}$ as for the experimental data. This procedure gives the function which is then fitted to the experimental correlation function.

Figure 5.20a shows the results of fitting a single peak to the neutron correlation function of GeO_2 glass (determined using the Lorch modification function with $Q_{\max} = 40$ Å^{-1}) [16], and the corresponding parameters are given in Table 5.3. A very close fit to the peak is obtained, as is apparent from the oscillations in the residual, which are of similar magnitude to the oscillations in the experimental data on either side of the peak.

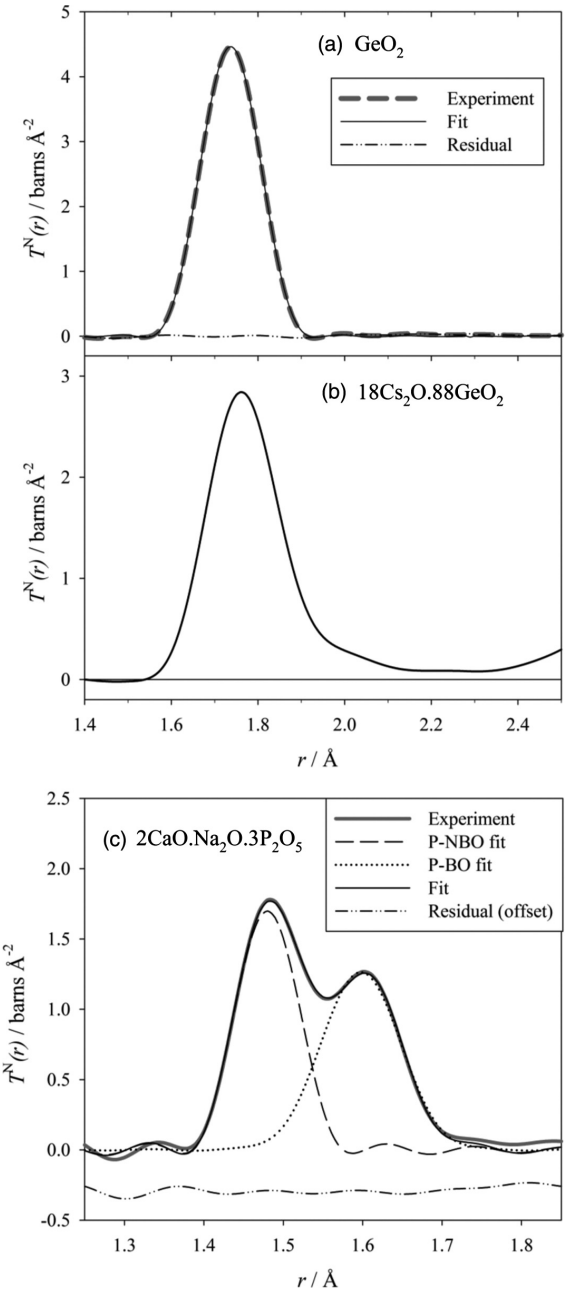

Figure 5.20. The first peak region of the total neutron correlation function, $T^N(r)$, for (a) GeO_2 glass [16] (thick grey line is experiment, thin black line is fit, dashed line is residual); (b) $18Cs_2O{\cdot}88GeO_2$ glass [16]; and (c) $2CaO{\cdot}Na_2O{\cdot}3P_2O_5$ glass (thick grey line is experiment, thin line is fit, dashed line is fitted P-NBO component, dotted line is fitted P-BO component, dot-dashed line is residual (offset)) [2, 42].

TABLE 5.3. Parameters from fitting the total neutron correlation function, $T^N(r)$.

Sample	Q_{max} / Å^{-1}	Atom pair, l–l'	$r_{ll'}$ / Å	$\langle u^2_{ll'} \rangle^{1/2}$ / Å	$n_{ll'}$
GeO_2	40	Ge-O	1.7369(2)	0.0422(3)	4.032(8)
$2CaO{\cdot}Na_2O{\cdot}3P_2O_5$	55	P-NBO	1.4800(6)	0.0362(5)	1.87(3)
		P-BO	1.5977(10)	0.0490(9)	1.96(4)

There is no apparent asymmetry in the observed peak, and probably the static disorder in the Ge–O bond lengths is very small. The fitting method is well suited to determining the area under such a peak, because it allows the (positive *and* negative) contributions from the termination ripples to be taken into account correctly. The coordination number of the fit (see Table 5.3) is within 1% of the ideal value of four for this tetrahedral glass, and a major reason for the high accuracy of this result is the high Q-resolution of the modern diffractometer that was used (see Section 5.4.2.1).

Figure 5.20c shows the results of fitting the sum of two peaks to the neutron correlation function of $2CaO{\cdot}Na_2O{\cdot}3P_2O_5$ glass (determined using the step modification function with $Q_{max} = 55$ Å^{-1}) [2, 42], and the corresponding parameters are given in Table 5.3. In this case, it is expected that the structure of a phosphate glass involves two discrete, different bond lengths (P-NBO and P-BO), and clearly fitting is well suited to determining them accurately. The software which has been used to produce the correlation function fits shown in this chapter (and which can also fit X-ray correlation functions) is available on the internet [45].

On the other hand, Figure 5.20b shows the neutron correlation function of a binary germanate glass containing 18 mol% Cs_2O (determined using the Lorch modification function with $Q_{max} = 40$ Å^{-1}) [16]. The position of the peak maximum is shifted to slightly longer distance, compared to pure GeO_2 glass, but the more marked effect is the appearance of a significant shoulder on the right hand side of the peak. This peak asymmetry is definite evidence of a distribution of Ge–O bond lengths in this glass. It is generally accepted that the addition of modifier to GeO_2 results in the average Ge–O coordination number increasing above four, and then decreasing back towards four when larger amounts of modifier are added, and ND has provided the main proof for this effect [16, 46, 47]. However, it is not yet fully established whether the higher coordinated germanium atoms are six-coordinated or five-coordinated (or both). Nevertheless, in either case the higher coordination is likely to involve more than one bond length; for example, it is well known that octahedral coordination usually involves two different bond lengths (axial and equatorial) due to the Jahn–Teller effect. If several different bond lengths (or a distribution of bond lengths) are expected within the envelope of a single correlation function peak, then it is debatable whether the fitting approach is the best way to characterize the peak. The advantages of fitting are that the contributions to the peak area from the termination ripples are included, and that it provides a reasonable way of taking into account the overlap with an adjacent peak (such as the O–O peak which is centered at approximately 2.8 Å in germanate glasses—see Figure 5.20b. In

this way, the experimental peak can be fitted using a small number of discrete distances, and thus the peak can be parameterized and a reasonable estimate of its area obtained [47]. A pitfall of this approach is that it provides values for several bond lengths which are not meaningful, with the hazard of overinterpretation.

In cases where there is an extended distribution of interatomic distances, it is preferable to determine the area under a peak in the experimental RDF by integration, which avoids the problem of potential overinterpretation, and then to use the coefficient $(2 - \delta_{ll'})c_l\bar{b}_l\bar{b}_{l'}$ from Eq. 5.43 to determine the coordination number. For this approach it is necessary to choose the limits for the integration, and usually the best choice is to use the position of the first minimum on either side of the peak. For example, integration of the RDF for the peak shown in Figure 5.20b between the two adjacent minima (at 1.48 and 2.30 Å) gives a Ge–O coordination number of 4.36, and this could correspond to 36% of the germaniums being 5-coordinated, or 18% being 6-coordinated [16]. Although it is not necessary to explicitly specify the distance range for a simple case like GeO_2, where there is a narrow distribution of bond lengths that is well separated from any other interatomic distances (see Figure 5.20a), for an extended, overlapping distribution (as for $18CsO{\cdot}82GeO_2$, Figure 5.20b) it is essential.

5.4.4 Normalization of Data

An ND measurement has the potential to measure coordination numbers which are more accurate than can be obtained by any other technique, because of the lack of a form factor and the ability to achieve a reliable normalization of the experimental data. However, as discussed below, for accurate coordination numbers to be obtained it is essential that the density and chemical composition of the sample are well known. Indeed, it is doubtful whether it is meaningful to determine a particular coordination number unless the composition of the sample is known.

As shown in the previous section (see Eq. 5.43), the coordination number is derived from the area, $A_{ll'}$, under a peak in the measured correlation function, $T^{\mathrm{N}}(r)$. However, an accurate coordination number can only be obtained if firstly the experimental corrections are performed as well as possible (see Section 5.4.1), and secondly the final correlation function is normalized as well as possible; if the normalization of the correlation function is not reliable, then the value obtained for the peak area, $A_{ll'}$, is not reliable. The coefficient $(2 - \delta_{ll'})c_l\bar{b}_l\bar{b}_{l'}$ in Eq. 5.43 depends on the atomic fraction for element l, and hence it is clear that the chemical composition of the sample must be well known for a reliable coordination number, $n_{ll'}$, to be derived from the peak area, $A_{ll'}$. However, the density of the sample is also of great importance due to the role it plays in determining the average density contribution, $T^0(r)$ (see Eq. 5.35). The quantity determined directly from the diffraction experiment is the differential correlation function, $D^{\mathrm{N}}(r)$, and then this is added to $T^0(r)$ to finally obtain the total correlation function, $T^{\mathrm{N}}(r)$ (see Figure 5.10). Thus, for $T^{\mathrm{N}}(r)$ to be reliable, it is required that $T^0(r)$ is reliable, *and* $D^{\mathrm{N}}(r)$ is correctly normalized relative to $T^0(r)$.

If the composition and density of the sample are both well known, then the average density contribution, $T^0(r)$, can be calculated reliably and it can be used to optimize the normalization of $T^{\mathrm{N}}(r)$, leading to accurate coordination numbers [48]. To illustrate this

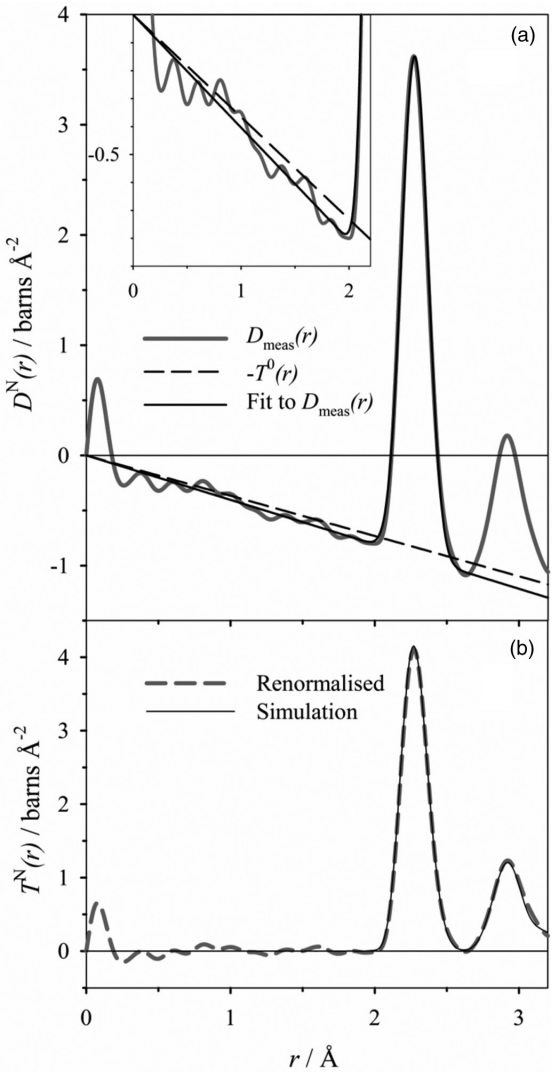

Figure 5.21. The low r region of the correlation function for crystalline Y_2O_3, showing (a) $D_{meas}(r)$ prior to renormalization (thick grey line), together with $-T^0(r)$ (dashed line) and a fit to the first peak in $D_{meas}(r)$ (thin black line) and (b) $T^N(r)$ after renormalization (thick grey line), together with a simulation (thin black line).

procedure, experimental data are shown for crystalline Y_2O_3; the structure of this crystal is well known [49], and there can be little doubt that the coordination is octahedral with $n_{YO} = 6$, and that the values for the density and chemical composition are reliable. Figure 5.21a shows the measured differential correlation function, $D_{meas}(r)$, as obtained by Fourier transformation of the corrected experimental diffraction pattern of Y_2O_3, and

also the negative of the average density contribution, $-T^0(r)$, calculated from the density and chemical composition,

$$T^0(r) = 4\pi r g^0 \left\langle \bar{b} \right\rangle_{\text{av}}^2 = -S^0 r. \tag{5.46}$$

In the low r region before the first peak, in principle $T^{\text{N}}(r)$ is zero (i.e., there are no interatomic distances below a certain minimum) and $D^{\text{N}}(r)$ should equal $-T^0(r)$. In practice $D^{\text{N}}(r)$ is expected to oscillate about $-T^0(r)$, due to the presence of termination ripples and experimental noise. It is apparent in Figure 5.21a that $D_{\text{meas}}(r)$ for Y_2O_3 does not agree closely with $-T^0(r)$. Figure 5.21a shows the result of a fit to the first peak in $D_{\text{meas}}(r)$ of a single peak (Eq. 5.44) together with a linear term, $-S_{\text{fit}}r$, where S_{fit} is a constant. The area of the fitted peak shown in Figure 5.21a gives a Y–O coordination number of 6.53. However, if the renormalizing factor S^0/S_{fit} is applied, then the renormalized Y–O coordination number is 5.93, which agrees closely with the ideal value of six, with an error of about 1%. Figure 5.21b shows the total correlation function calculated according to

$$T(r) = T^0(r) + \frac{S^0}{S_{\text{fit}}} D_{\text{meas}}(r), \tag{5.47}$$

together with a simulation of the total neutron correlation function, derived from the reported crystal structure [49]. The quality of the final normalization is apparent from the close agreement between the areas under the simulated and measured functions. The question arises as to why the data may not be perfectly normalized after careful corrections have been performed, and there are several possible reasons. For example, it may not be possible to determine the number of atoms in the beam accurately (the sample may not be perfectly uniform, the definition of the beam may not be precise, the beam profile may not be uniform, etc.), or there may be a sample-dependent contribution to the background.

5.4.5 Scattering at low *Q*

5.4.5.1 Homogeneous Samples Ideally, the Fourier transform (Eq. 5.34) requires that the distinct scattering is measured to a minimum Q-value of zero, but this cannot be achieved experimentally. However, it has long been established [50] that for a homogeneous sample (i.e., a sample which has no small angle scattering—see Section 5.4.5.2) the low Q limit may be represented as

$$i(Q) = A + BQ^2. \tag{5.48}$$

This form may be justified by considering that the scattering must be symmetric, that is, the same diffraction pattern must be measured for negative values of Q as for positive values. It can be useful to fit Eq. 5.48 to the low Q region (say below 1 Å^{-1} or less) of the measured distinct scattering as a means of extrapolating to $Q = 0$, prior to Fourier

transformation. A simple way of performing such a fit is to plot *i(Q)* versus Q^2, and then to perform a linear fit to the low Q region.

For a single phase liquid (i.e., a liquid without variations in chemical composition or density) at temperature T, the $Q = 0$ limit of the structure factor (for ND or XRD) is given by [51]

$$S(0) = g^0 k_B T \kappa. \tag{5.49}$$

where k_B is the Boltzmann constant and κ is the isothermal compressibility of the liquid. Strictly, this equation does not apply to a glass, because glasses are not in true thermodynamic equilibrium. However, a glass made by melt quenching can be regarded as a liquid which has been frozen at the glass transition temperature, T_g, and Wright et al. [52] have shown in a careful study of SiO_2 glass that the zero Q limit of the diffraction pattern of the glass is given by evaluating Eq. 5.49 for the melt at the glass transition temperature, using the high frequency determination of the isothermal compressibility. This has important implications for the nature of the glassy state, since it shows that the fluctuations of the melt are frozen in at temperature T_g; this is a strong argument against the formation of a micro-crystalline structure for the glass.

5.4.5.2 Inhomogeneous Samples If a sample has microstructure (i.e., inhomogeneities on a length scale, L, of order say ~10–1000Å) then the diffraction pattern will exhibit additional scattering at low Q (less than say 0.1 $Å^{-1}$), known as small angle neutron scattering (SANS) because it is normally measured at small scattering angles. The only true Bragg peak which arises from non-crystalline samples is the (000) reflection, which cannot be observed because it coincides with the transmitted beam. However, microstructure in the sample leads to a broadening of the Bragg peaks, and at low Q this is observed as SANS. A detailed discussion of microstructure is beyond the scope of this chapter, but it is worth noting that a fine powder sample will exhibit a significant SANS signal in the diffraction pattern.

To illustrate the phenomenon of SANS, it is worthwhile to consider an isolated (surrounded by empty space) sphere of radius R, with a uniformly distributed scattering length density, ρ_b, containing N atoms. For this uniform sphere, the distinct scattering is calculated analytically [53] as

$$i^N(Q) = 9I_0 \left(\frac{\sin y - y \cos y}{y^3} \right)^2, \tag{5.50}$$

where $y = QR$, and the $Q = 0$ limit is $I_0 = \rho_b^2 V_s^2 / N$, with sphere volume $V_s = 4\pi R^3/3$. (This is one of the very few uniform geometric objects for which an analytic result exists.) Figure 5.22a shows this function for a sphere of radius 20 Å. The scattering rises very strongly at low Q (less than about 0.2 $Å^{-1}$) to values greatly in excess of those observed at higher Q (see Figure 5.16). It is fundamental to note that SANS is observed if there is a *contrast* between the scattering length density of the object, ρ_b, and its surroundings.

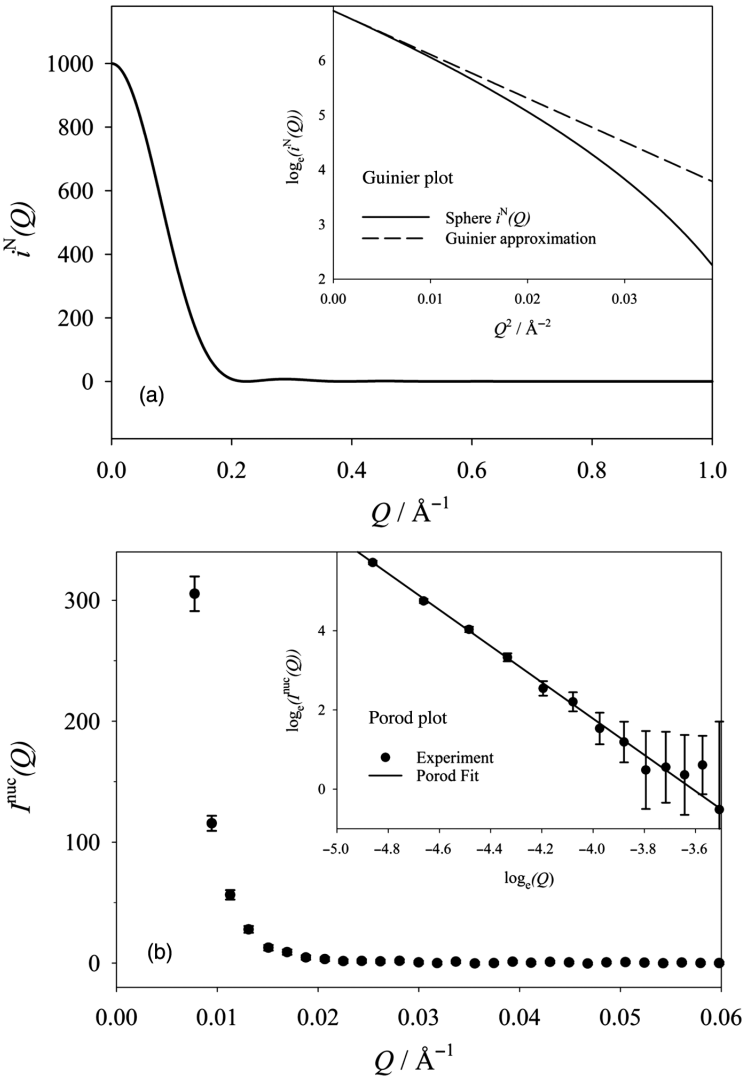

Figure 5.22. (a) The predicted distinct scattering for an isolated sphere of radius 20 Å, with $I_0 = 1000$. The inset shows a Guinier plot of the prediction, together with the corresponding Guinier approximation. (b) The measured nuclear SANS for amorphous Dy_7Ni_3. The inset shows a Porod plot of the experimental data, together with a Porod fit to the data.

If the scattering length density varies over a characteristic distance, L (e.g., the particle size), and the Q-values of the experimental data are small in comparison with L^{-1} (i.e., $QL \ll 1$), then the SANS can be described in terms of the Guinier approximation [54]. In this approximation, the coherent differential cross-section for a sample with

N_p particles of uniform scattering length density ρ_{bp}, embedded in a matrix of uniform scattering length density ρ_{bm}, is

$$\frac{d\sigma}{d\Omega}^{coh} = \frac{V_p^2 N_p^2}{N}(\rho_{bp} - \rho_{bm})^2 \exp\left(-Q^2 R_G^2/3\right), \tag{5.51}$$

where R_G is the radius of gyration (i.e., the RMS distance of part of the particle from its center). In this regime it is useful to plot the experimental data as $\log_e(I)$ versus Q^2, as shown in the inset to Figure 5.22a, in which case the slope of a linear fit yields an estimate of the particle size, R_G.

If the experimental Q-values are large in comparison with L^{-1} (i.e., $QL \gg 1$), then the SANS can be described in terms of the Porod approximation [55],

$$\frac{d\sigma}{d\Omega}^{coh} = \frac{2\pi A_p N_p}{N}(\rho_{bp} - \rho_{bm})^2 Q^{-n}, \tag{5.52}$$

where A_p is the surface area of a particle. If the structures giving rise to the SANS are compact and smooth then the dimensionality, n, has the value of four, but if the structures are fractal in nature then the value of n differs from four [56, 57]. Figure 5.22b shows a measurement of the nuclear SANS for the melt-spun amorphous metal Dy_7Ni_3 [58] (measured on the former D17 small angle diffractometer at the Institut Laue Langevin). In the Porod regime it is useful to plot the experimental data as $\log_e(I)$ versus $\log_e(Q)$, as shown in the inset to Figure 5.22b, in which case the slope of a linear fit yields the dimensionality. The Porod fit shown in Figure 5.22b yields a slope close to four, indicating that the SANS arises from the structure of the surface of the melt-spun ribbons. Contrast matching is an important experimental technique for SANS; this involves placing the sample in liquids of different scattering length density (which may be prepared, for example, by mixing H_2O and D_2O in different proportions) and observing the effect on the SANS signal. For example, this technique has been applied to melt-spun amorphous metal ribbons [59, 60]; it was possible to almost entirely remove the observed SANS, showing again that it arises from the surface structure of the ribbons.

The ordinary ND pattern (sometimes known as WANS—wide angle neutron scattering), as described elsewhere in this chapter, has conventionally been analyzed separately from the SANS signal. However, the advent of new ND instrumentation, particularly the Near and Intermediate Range Order Diffractometer [61] (NIMROD) at the ISIS Facility, which covers a Q-range wide enough to measure both regions simultaneously enables the interesting possibility of modeling both the microstructure and the atomic level structure at the same time.

5.4.6 Sample-Related Difficulties

As discussed in Section 5.4.4, for reliable and meaningful results to be obtained from an ND experiment on a glass, it is essential that the composition and density of the sample are well known. Thus glass samples studied by ND should always be well characterized, using as many different experimental techniques as possible.

TABLE 5.4. Energies of nuclear resonances below 4 eV for stable nuclei [62, 63].

Z	Element	Isotope	Resonance energies/eV						
38	Sr	^{87}Sr	3.54(2)						
45	Rh	^{103}Rh	1.257(2)						
46	Pd	^{108}Pd	2.96(1)						
48	Cd	^{113}Cd	0.178(2)						
49	In	^{113}In	1.80(3)						
		^{115}In	1.457(2)						
52	Te	^{123}Te	2.334(8)						
62	Sm	^{147}Sm	3.397(20)						
		^{149}Sm	0.0973(2)	0.872(3)					
63	Eu	^{151}Eu	0.321(1)	0.460(1)	1.055(3)	1.815(7)	2.717(5)	3.368(6)	3.710(6)
		^{153}Eu	1.727(5)	2.456(5)	3.294(6)	3.944(8)			
64	Gd	^{152}Gd	3.31(4)						
		^{155}Gd	0.0268(2)	2.008(10)	2.568(13)	3.616(6)			
		^{157}Gd	0.0314(2)	2.825(15)					
65	Tb	^{159}Tb	3.339(5)						
66	Dy	^{160}Dy	1.88(2)						
		^{161}Dy	2.71(2)	3.68(2)					
		^{163}Dy	1.713(4)						
67	Ho	^{165}Ho	3.92(1)						
68	Er	^{167}Er	0.460(2)	0.584(2)					
70	Yb	^{168}Yb	0.597(1)						
71	Lu	^{175}Lu	2.590(5)						
		^{176}Lu	0.1413(3)	1.565(4)					
72	Hf	^{177}Hf	1.098(20)	2.388(2)					
73	Ta	^{180}Ta	0.20(1)	0.435(1)	2.061(2)	2.203(4)	3.952(4)		
75	Re	^{185}Re	2.156(4)						
77	Ir	^{191}Ir	0.6528(50)						
		^{193}Ir	1.298(1)						
92	U	^{235}U	0.290(5)	1.124(5)	2.028(4)	2.76(1)	3.145(5)	3.615(5)	

5.4.6.1 Nuclear Resonances A nucleus absorbs neutrons very strongly if the neutron energy is close to the energy of an excited state of the nucleus; this phenomenon is known as a nuclear resonance [62, 63]. It is extremely hard to obtain useful ND data if the neutron energy is close to a resonance, due to the very strong absorption, but fortunately the great majority of isotopes do not have a resonance in the energy range used for ND.

Table 5.4 lists the energies for all resonances of stable nuclei which are less than 4 eV [62,63]. If a sample contains any of these nuclei then the effect of the resonance needs to be considered in an ND experiment. For a constant wavelength diffractometer it is necessary to choose a neutron wavelength so that the energy (see Eq. 5.3) is not close to a resonance energy. For a T-O-F diffractometer, the effect of resonances is more complex, and this is illustrated by Figure 5.23 which shows the corrected differential cross-section for a $10K_2O.90TeO_2$ glass [64], measured on the former LAD diffractometer [65]. The ^{123}Te nucleus has a resonance at 2.334(8) eV (see Table 5.4) [62], so that there is strong absorption in the region of the spectra which correspond to this energy, and this gives rise to a negative peak in the experimental data. The negative peak occurs over a

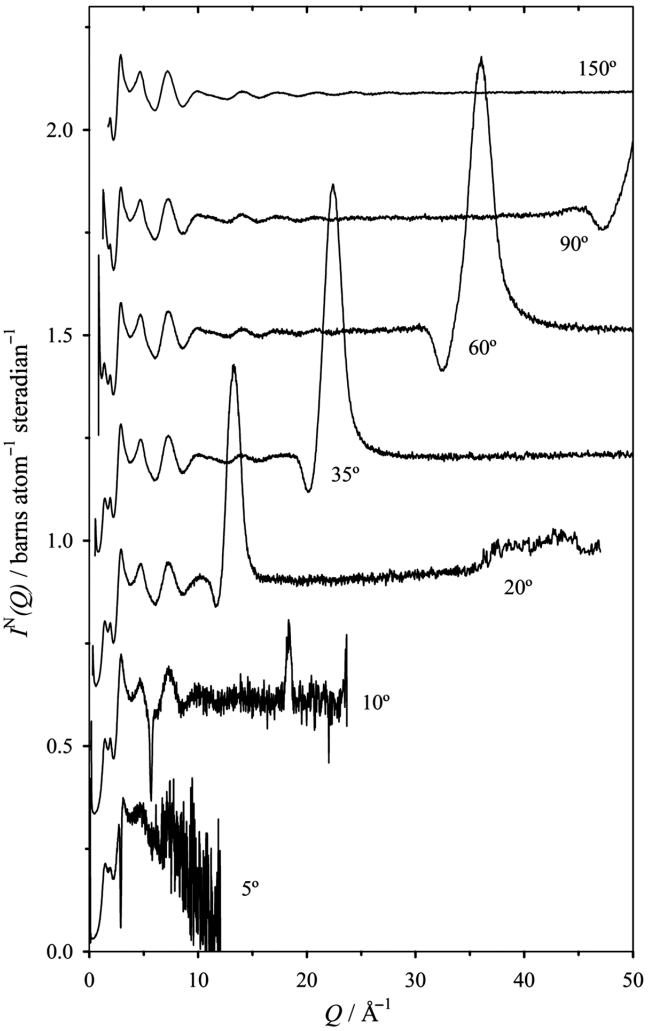

Figure 5.23. The (corrected and normalized) differential cross-section of $10K_2O{\cdot}90TeO_2$ glass, $I^N(Q)$, measured on the former LAD diffractometer [65]. The curves for the different detector banks are shown with vertical offsets for clarity.

different Q range for each detector angle, illustrating an important point in understanding experimental problems with T-O-F diffraction; if a problem is due to a diffraction effect then the related feature occurs at the same Q-value for different detector angles, but if a problem is due to a constant-energy effect (such as a resonance) then the related feature occurs at different Q-values for different detector angles. For the data shown in Figure 5.23, there is also a strong positive peak for the intermediate detector angles (20°, 35°, 60°, and 90°) because these detectors were sensitive to γ-rays; when a neutron is absorbed by a nucleus it may give rise to a prompt γ-ray which arrives at the detector

before neutrons with the energy of the resonance. However, modern neutron detectors should have very low sensitivity to γ-rays, so that this phenomenon is not observed. For a sample containing an element with a resonance, a reliable result (covering a full Q-range) can be obtained from a T-O-F diffractometer if the detectors cover a large range of angles; in this case a reliable result is obtained by combining the spectra from the different angles so that the Q-range for each angle that is affected by the resonance is avoided. Nevertheless, Table 5.4 shows that there are very few elements which are ill-suited to study by ND. For example, europium and gadolinium have a large number of resonances in the thermal region so that they are effectively "black" and useful ND results cannot be obtained. Neutron resonances are particularly common for rare earth (RE) elements, and hence (considering the chemical similarity of REs) it may be advisable when planning an experiment to choose to study samples containing REs for which resonances are not a problem.

5.4.6.2 Hydrogen Contamination It is always important to minimize chemical contamination of the sample, but for ND the effect of hydrogen contamination is especially profound. Some glasses, such as borates or phosphates, are particularly prone to pick up moisture (in the form of either –OH or H_2O) [66, 67], and much better ND results will be obtained if this contamination is reduced or eliminated. It may be advisable to place a sample under vacuum or in a sealed, dry environment as soon after manufacture as possible. Sometimes moisture contamination can be removed by drying in a vacuum oven, but this is only effective at removing surface H_2O, and has little effect on –OH or H_2O in the bulk. If the chemical formula of the sample of interest includes hydrogen, then ND results can be greatly improved if the sample is deuterated (i.e., if the hydrogen atoms are replaced with deuterium atoms). Nevertheless, it should be borne in mind that if a deuterated sample is exposed to normal atmosphere, the deuteration may be reversed within a few minutes, due to exchange with hydrogen in atmospheric moisture, which can be rapid.

For some scientific studies, however, it is desirable to measure ND for a sample with a significant hydrogen content. For example, Figure 5.24 shows experimental data for a sample of an amorphous zeolite precursor, which contains a large amount of hydrogen [68]. This illustrates the problems that arise with hydrogen; first, the very large incoherent cross-section of hydrogen (see Section 5.3.5) leads to a large incoherent background, and second, the inelasticity effect for hydrogen (see Section 5.3.6.1) is very severe, causing a strong rise in the self scattering at low Q. In fact, the approximate methods which are commonly used to calculate the self scattering (such as that originally proposed by Placzek [8]) break down if the sample contains hydrogen (because the neutron and proton mass are very similar), and it is necessary to remove the self scattering by an empirical method. Figure 5.24 shows a smooth fit to the experimental $I^N(Q)$ data which was achieved by using a cubic spline with variable knot spacing, together with the estimate of the distinct scattering that was obtained by subtraction of this fit [68]. Although such empirical methods are useful, it is always preferable to remove hydrogen from the sample if possible.

As shown in Section 5.3.6.1 (see Figures 5.11 and 5.12), the effect of inelasticity is much reduced at low scattering angle, and for this reason T-O-F neutron diffractometers with all of the detectors at low angle, such as SANDALS [69] (Small Angle Neutron

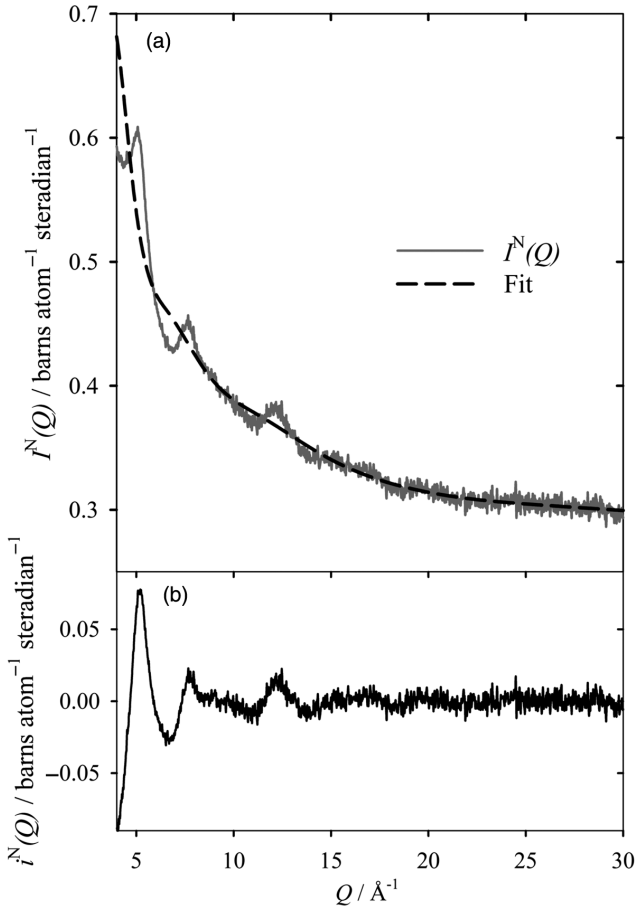

Figure 5.24. (a) The differential cross-section measured by Bank5 (93°) of the GEM diffractometer [2] for amorphous zeolite precursor LTA_5 [68], together with a smooth cubic spline fit. (b) The estimate of the distinct scattering which is obtained from a difference of the two curves in (a).

Diffractometer for Amorphous and Liquid Samples) and NIMROD [61] at the ISIS Facility, are available for the study of samples with low atomic mass (e.g., aqueous solutions).

5.4.6.3 Crystal Contamination ND is much more penetrating than XRD (which may only probe a short distance into the surface of the sample, depending on the X-ray wavelength and the sample composition), and thus for a sample containing a crystalline impurity the ND pattern is more likely than the XRD pattern to exhibit Bragg peaks. Furthermore, ND (especially time-of-flight ND) tends to have high Q-resolution, which also acts to make Bragg peaks more apparent. It is thus common for samples which appear fully amorphous by laboratory XRD to be shown to contain a significant crystalline contamination when ND is performed.

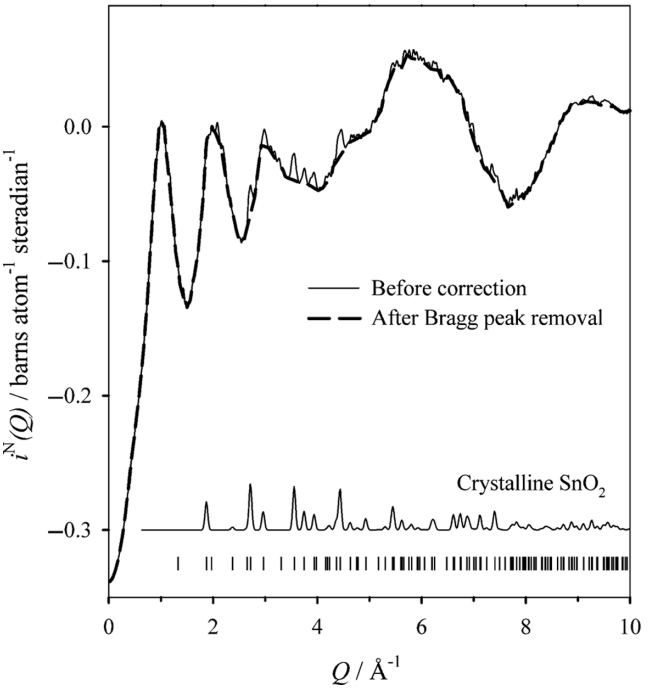

Figure 5.25. The distinct scattering, $i^N(Q)$, for a tin borate glass sample with nominal composition $70SnO{\cdot}30B_2O_3$ before and after removal of Bragg peaks (see text) [13]. Also shown is a simulation of the diffraction pattern for crystalline SnO_2 and vertical tick marks indicate the positions of the Bragg peaks.

Of course it is preferable to study phase pure glass samples that do not contain crystalline material, but sometimes this is not possible, and then it may be desirable to remove the Bragg peaks from the diffraction pattern. As a simple example, Figure 5.25 shows diffraction data for a tin borate-based glass of nominal composition $70SnO{\cdot}30B_2O_3$ [13], which exhibits Bragg peaks due to crystalline impurities. In this case, the Bragg peaks have been removed by the simple expedient of fitting a straight line underneath the Bragg peak. Figure 5.25 also shows a simulation of the diffraction pattern of crystalline SnO_2 in the rutile phase [70], calculated using CrystalMaker® software [71]. The predominant crystalline impurity is clearly SnO_2, due to disproportionation and then oxidation of tin in the melt [72]. The example in Figure 5.25 illustrates the difficulty of Bragg peak removal. As Q increases, the Bragg peaks become closer together, and it becomes impossible to remove them individually; thus the contribution from the crystalline impurity cannot be removed at higher Q. It is also not possible to remove the crystalline contribution to the diffraction pattern well by using a conventional crystallographic simulation method (e.g., the Rietveld method [73]), because such methods do not correctly describe the short range order (especially the effects of correlated atomic motion, see Section 5.3.6.2) and hence they

do not predict the higher Q region of the diffraction pattern. Therefore, the best way to remove the contribution due to a crystalline impurity may be to measure ND for a pure sample of the impurity, followed by a suitable subtraction of the correlation functions [74].

5.4.7 Partial Correlation Functions

5.4.7.1 Isotopic Substitution A limitation of a standard ND experiment is that the information obtained is not element-specific. The neutron correlation function, $T^{\mathrm{N}}(r)$, has contributions from all possible pairs of elements in the sample (e.g., Si–Si, Si–O, and O–O for SiO_2), and as r increases the contributions from the different pairs rapidly overlap and cannot be resolved. Isotopic substitution (first reported by Enderby et al. in a study of liquid Cu_6Sn_5 [75]) is a very important technique that can address this problem [18]. In this section, the method is first illustrated by a particularly elegant example, and is subsequently discussed from a general point of view.

There are a few elements which have isotopes with both positive and negative scattering lengths (H, Li, Ti, Cr, Ni, Sm, Dy, and W), in which case isotopic substitution can be used so that the coherent scattering length for the element is zero. This is known as *the null technique*; if an element has a coherent scattering length of zero, then this element does not contribute to the distinct scattering, and none of its partial correlation functions contribute to the measured correlation function. This technique is especially powerful if it can be applied to both elements in a sample with two elements—this has been called the double-null isotopic substitution technique [76].

The total correlation function measured in a single diffraction experiment is a sum of pairwise partial correlation functions (see Eq. 5.36), and for the binary amorphous metal Dy_7Ni_3 the total neutron correlation function is given by

$$T^{\mathrm{N}}(r) = c_{\mathrm{Dy}}\bar{b}_{\mathrm{Dy}}^2 t_{\mathrm{DyDy}}(r) + 2c_{\mathrm{Dy}}\bar{b}_{\mathrm{Dy}}\bar{b}_{\mathrm{Ni}} t_{\mathrm{DyNi}}(r) + c_{\mathrm{Ni}}\bar{b}_{\mathrm{Ni}}^2 t_{\mathrm{NiNi}}(r), \tag{5.53}$$

where $c_{\mathrm{Dy}} = 0.7$ and $c_{\mathrm{Ni}} = 0.3$ are the atomic fractions for the two elements. There are three independent partial correlation functions, because the Dy–Ni and Ni–Dy functions are not independent (see Eq. 5.37). (In general, a sample with N_{e} elements has $N_{\mathrm{e}}(N_{\mathrm{e}}+1)/2$ independent partial correlation functions.) ND was measured for all four samples, $^{\mathrm{Nat}}Dy_7{}^{\mathrm{Nat}}Ni_3$, $^{\mathrm{Nat}}Dy_7{}^{0}Ni_3$, $^{0}Dy_7{}^{\mathrm{Nat}}Ni_3$, and $^{0}Dy_7{}^{0}Ni_3$ (where ^{0}Dy and $^{\mathrm{Nat}}$Dy indicate dysprosium with the null and natural isotopic compositions, respectively) and the measured diffraction data are shown in Figure 5.26. For the $^{0}Dy_7{}^{0}Ni_3$ sample, there is no coherent nuclear scattering from either element, and this enables the magnetic scattering, $I^{\mathrm{M}}(Q)$, to be measured, so that it can be subtracted from the results for the other three samples. At room temperature, which is greatly in excess of the 35 K magnetic ordering temperature for Dy_7Ni_3, the magnetic scattering is almost entirely self scattering, given by

$$I^{\mathrm{MS}}(Q) = \frac{2}{3}(\gamma r_0)^2 \sum_l c_l \left|f_l(Q)\right|^2 \left\langle \mu_l^2 \right\rangle, \tag{5.54}$$

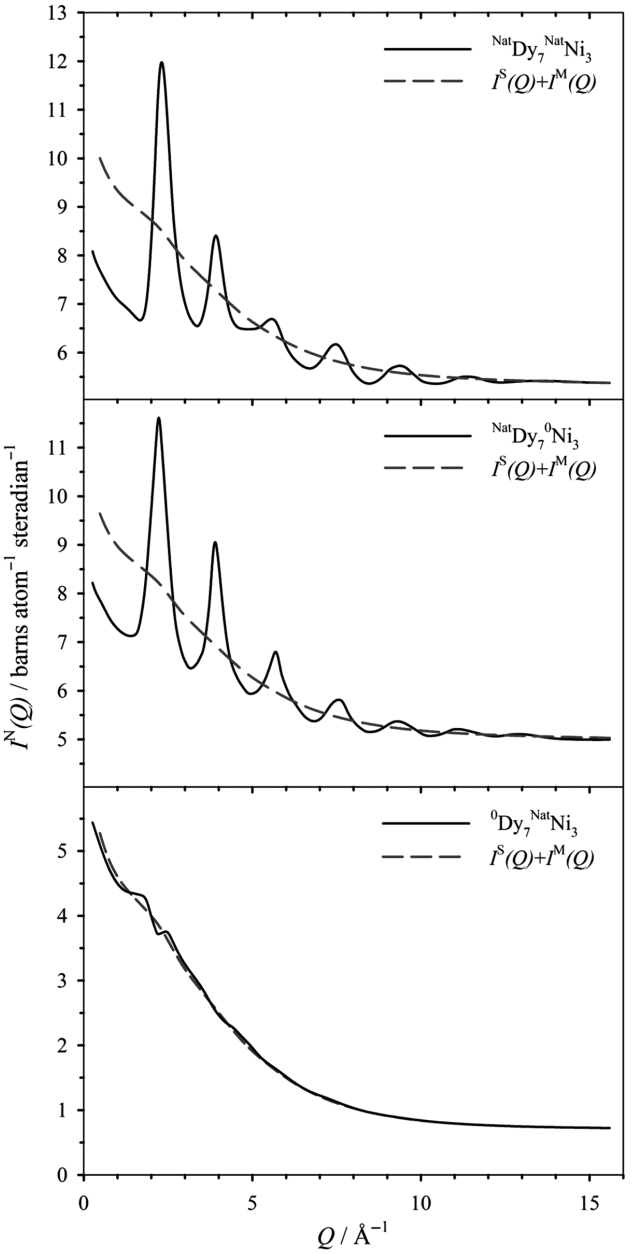

Figure 5.26. The differential cross-section, $I^N(Q)$, of amorphous Dy_7Ni_3 for three different isotopic compositions (superscripts Nat and 0 indicate the natural isotopic composition and the null isotopic composition), shown as a continuous line [58]. The dashed line indicates the sum of the magnetic scattering, $I^M(Q)$, and the calculated nuclear self scattering, $I^S(Q)$, for each sample.

where γ is the neutron magnetic moment in nuclear magnetons and r_0 is the classical electron radius. $f_l(Q)$ and $\langle \mu_l^2 \rangle$ are respectively the magnetic form factor and mean square magnetic moment for element l. Thus $I^M(Q)$ is proportional to $|f_{Dy}(Q)|^2$, where $f_{Dy}(Q)$ is the dysprosium magnetic form factor. For the $^{Nat}Dy_7{}^0Ni_3$ sample, $\bar{b}_{Ni} = 0$, and hence Eq. 5.53 shows that the experimental correlation function yields a direct measurement of the $t_{DyDy}(r)$ partial correlation function. Similarly, the $^0Dy_7{}^{Nat}Ni_3$ sample has $\bar{b}_{Dy} = 0$ and yields a direct measurement of the $t_{NiNi}(r)$ correlation function. These two like-atom partial correlation functions can then be combined (according to Eq. 5.53) with the correlation function measured for the $^{Nat}Dy_7{}^{Nat}Ni_3$ sample to obtain the unlike-atom correlation function, $t_{DyNi}(r)$. Figure 5.27 shows the three partial correlation functions for Dy_7Ni_3, obtained by use of the double-null isotopic substitution technique [58]. The figure also shows the partial correlation functions calculated for a Dy_7Ni_3 hard sphere liquid, according to the Percus–Yevick equation [77, 78]. For a binary hard sphere system, the interatomic distance for unlike-atom contacts is midway between the two distances for like-atom contacts, but (as is shown by the comparison with the hard sphere calculation in Figure 5.27) this is not the case for Dy_7Ni_3. Instead the measured partial correlation functions show that pairs of nickel atoms are close but not touching. The amorphous metal has a more ordered structure than a hard sphere liquid, and the observed Ni–Ni nearest neighbor distance is similar to that in crystalline Dy_3Ni_2 [79], where it arises from two nickel atoms packed into the recess on either side of a square of four dysprosium atoms (as shown in the inset to Figure 5.27).

For most elements, it is not possible to use the null technique, but nevertheless isotopic substitution can be performed (although there are some elements for which isotopic substitution is not feasible, either because there is only one stable isotope, or because the difference between the scattering lengths of the available isotopes is too small). If only one substitution is performed, then this is known as a *first difference*. In this case, let A be the element on which isotopic substitution is performed so that two samples are made in which it has scattering lengths $\bar{b}_A$ and $\bar{b}'_A$. The correlation functions measured for these two samples are $T(r)$ and $T'(r)$. Using these two measurements it is possible to separate any two of the three combinations A–A, A–X and X–X (where X is any element other than A). However, the two most useful combinations are a simple difference, or a weighted difference, derived from Eq. 5.36 as follows:

$$T(r) - T'(r) = c_A\left(\bar{b}_A - \bar{b}'_A\right)\left(\left(\bar{b}_A + \bar{b}'_A\right)t_{AA}(r) + 2\sum_{\substack{k \\ k\neq A}} \bar{b}_k t_{Ak}(r)\right), \quad (5.55)$$

$$\bar{b}_A T'(r) - \bar{b}'_A T(r) = \left(\bar{b}_A - \bar{b}'_A\right)\left(\sum_{\substack{j \\ j\neq A}}\sum_{\substack{k \\ k\neq A}} c_j \bar{b}_j \bar{b}_k t_{jk}(r) - c_A \bar{b}_A \bar{b}'_A t_{AA}(r)\right), \quad (5.56)$$

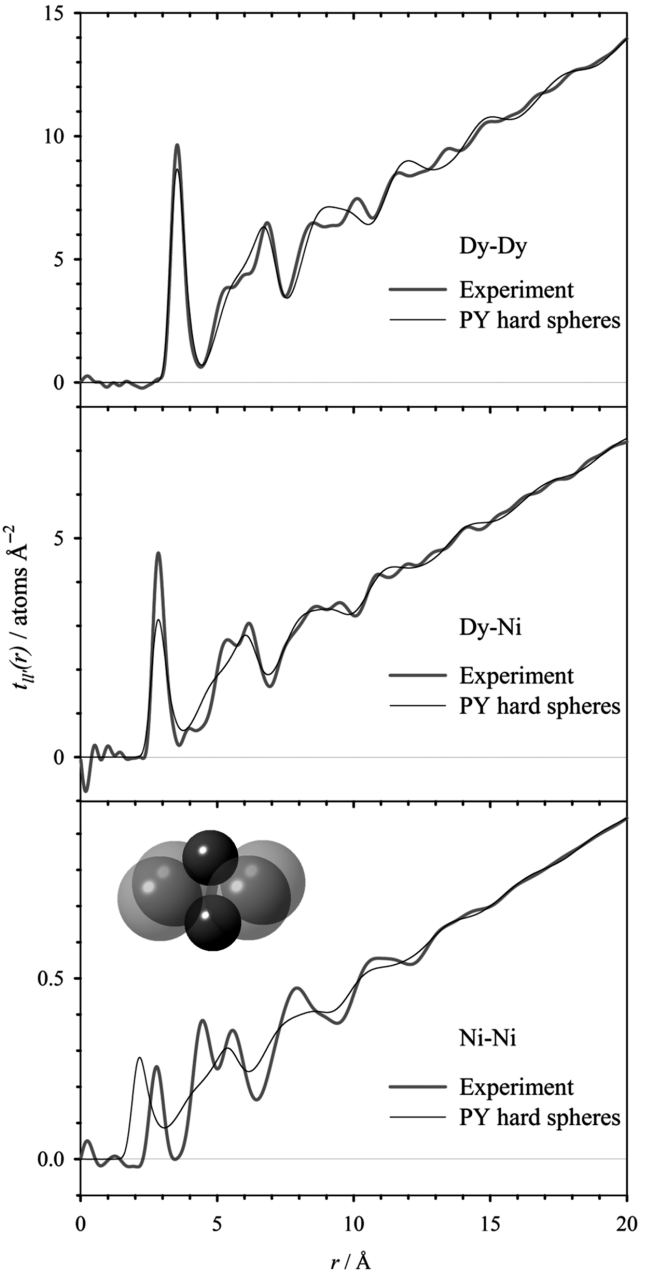

Figure 5.27. The three measured partial correlation functions for amorphous Dy_7Ni_3 [58], together with the partial correlation functions for a Percus–Yevick calculation of the partial correlation functions for a binary hard sphere liquid. The inset in the figure shows how a similar Ni–Ni distance arises in crystalline Dy_3Ni_2 [79] (large, translucent spheres are Dy, smaller, solid spheres are Ni).

Equation 5.55 shows that the result of a simple difference only includes correlations which involve element A; that is, it eliminates correlations which do not involve A. Equation 5.56 shows that the result of the weighted difference eliminates all correlations involving A except the A–A correlation, that is, it eliminates all unlike-atom correlations which involve A. Note that a first difference, as in Eq. 5.55, is equivalent to a XAFS (X-ray Absorption Fine Structure) measurement at the absorption edge of element A, but with the added advantage that it yields longer range information, which is not accessible to the XAFS experiment due to the absence of data at low wavevector.

If another substitution is performed, say a measurement in which the scattering length of element A is changed to $\bar{b}_{\mathrm{A}}''$, so that the correlation function is $T''(r)$, then this is known as a *second difference*. It is then possible to obtain a complete separation into A–A, A–X and X–X contributions, for example,

$$t_{\mathrm{AA}}(r) = \frac{\bar{b}_{\mathrm{A}}\left(T'(r) - T''(r)\right) + \bar{b}_{\mathrm{A}}'\left(T''(r) - T(r)\right) + \bar{b}_{\mathrm{A}}''\left(T(r) - T'(r)\right)}{c_{\mathrm{A}}\left(\bar{b}_{\mathrm{A}} - \bar{b}_{\mathrm{A}}'\right)\left(\bar{b}_{\mathrm{A}} - \bar{b}_{\mathrm{A}}''\right)\left(\bar{b}_{\mathrm{A}}'' - \bar{b}_{\mathrm{A}}'\right)}. \quad (5.57)$$

For a sample containing N_{e} elements, there are $N_{\mathrm{e}}(N_{\mathrm{e}}+1)/2$ independent partial correlation functions, and hence this number of isotopic substitution measurements must be made in order to achieve a complete separation of all the partial pairwise atomic correlation functions; this rapidly becomes prohibitive as the number of elements increases.

For simplicity, consider a sample containing two elements A and B (e.g., Dy_7Ni_3). If three correlation functions, $T(r)$, $T'(r)$, and $T''(r)$, are measured for three samples with scattering lengths $(\bar{b}_{\mathrm{A}}, \bar{b}_{\mathrm{B}})$, $(\bar{b}_{\mathrm{A}}', \bar{b}_{\mathrm{B}}')$, and $(\bar{b}_{\mathrm{A}}'', \bar{b}_{\mathrm{B}}'')$, respectively, then the measured correlation functions are related to the partials by

$$\begin{bmatrix} T(r) \\ T'(r) \\ T''(r) \end{bmatrix} = [A] \begin{bmatrix} t_{\mathrm{AA(r)}} \\ t_{\mathrm{BB}}(r) \\ t_{\mathrm{AB}}(r) \end{bmatrix} = \begin{bmatrix} c_{\mathrm{A}}\bar{b}_{\mathrm{A}}^2 & c_{\mathrm{B}}\bar{b}_{\mathrm{B}}^2 & 2c_{\mathrm{A}}\bar{b}_{\mathrm{A}}\bar{b}_{\mathrm{B}} \\ c_{\mathrm{A}}\bar{b}_{\mathrm{A}}'^2 & c_{\mathrm{B}}\bar{b}_{\mathrm{B}}'^2 & 2c_{\mathrm{A}}\bar{b}_{\mathrm{A}}'\bar{b}_{\mathrm{B}}' \\ c_{\mathrm{A}}\bar{b}_{\mathrm{A}}''^2 & c_{\mathrm{B}}\bar{b}_{\mathrm{B}}'^2 & 2c_{\mathrm{A}}\bar{b}_{\mathrm{A}}''\bar{b}_{\mathrm{B}}'' \end{bmatrix} \begin{bmatrix} t_{\mathrm{AA}}(r) \\ t_{\mathrm{BB}}(r) \\ t_{\mathrm{AB}}(r) \end{bmatrix}. \quad (5.58)$$

The three partial correlation functions can then be obtained by means of an inversion of the matrix A,

$$[t(r)] = [A]^{-1}\ [T(r)]. \quad (5.59)$$

Thus the partial correlation functions are essentially obtained by solving simultaneous equations, and Eq. 5.57 shows that the extraction of the partials depends critically on the difference between scattering length values. Even if the scattering length values are known very precisely, the matrix inversion amplifies the errors on the measured correlation functions. Thus the differences in scattering length need to be as large as possible, for the derivation of partials to be well-conditioned. As Livesey and Gaskell have proposed [80], Turing's number, T_{n} [81], can be used as a figure of merit for isotopic substitution experiments. T_{n} gives an upper limit on the factor by which the fractional

error in the partial functions exceeds the fractional error in the measurements, and is given approximately by

$$T_{\mathrm{n}} = |A|_{\mathrm{E}} \left|A^{-1}\right|_{\mathrm{E}}, \tag{5.60}$$

where the Euclidean norm is given by adding in quadrature the components of the matrix A,

$$|A|_{\mathrm{E}} = \left(\sum_{i,j} A_{ij}^2 \right)^{1/2}. \tag{5.61}$$

For example, the study of Dy_7Ni_3 using the double-null isotopic substitution technique is one of the most well-conditioned of all isotopic substitution studies, with $T_{\mathrm{n}} = 12.3$. For most isotopic substitution studies in the literature, the value of T_{n} is typically an order of magnitude larger. Consequently, there are severe experimental requirements on an isotopic substitution experiment if a satisfactory separation of partials is to be achieved. First, it is essential that the samples be identical, apart from their differing isotopic composition, and XRD is usually the preferred way to verify this. Furthermore the measurements on the isotopic samples must be performed in the same way, to reduce the effect of systematic errors. High statistical accuracy diffraction data are required, which requires long counting times and also high detector stability.

An excellent example of isotopic substitution on a glass has been given by Eckersley and Gaskell who have reported both first difference [82] and second difference [83] isotopic substitution for $48CaO{\cdot}49SiO_2{\cdot}3Al_2O_3$, using calcium isotopes. The first difference showed that modifier ions have a well-ordered nearest neighbor shell and also ordering at longer distances up to ∼10Å. Another example of a second difference measurement has been given by Petri et al. [84] for $GeSe_2$ glass, using both Ge and Se isotopes to obtain a full separation of the partial functions, finding evidence for defects in the form of homopolar (i.e., Ge–Ge and Se–Se) bonds. The method of H/D substitution has made a big impact in the study of molecular liquids, especially aqueous solutions [85], because there is a large difference between the hydrogen and deuterium scattering lengths ($\bar{b}_{\mathrm{H}} = -3.739$ fm and $\bar{b}_{^2\mathrm{H}} = 6.671$ fm [32]), and deuterated samples are available relatively cheaply, with the possibility of deuterating specific molecular sites.

5.4.7.2 Other Methods An impediment to the widespread use of isotopic substitution is the very high financial cost of isotopic material (especially since ND requires relatively large samples, say a few grams), and also the lack of suitable isotopes for some elements. However, other methods may also be used to help to differentiate the various partial contributions to the total correlation function. The most widely applicable of these methods involves the combination of ND and XRD. The strength of X-ray scattering for a given element is proportional to the atomic number, Z, whereas the coherent neutron scattering length varies haphazardly across the periodic table (see Figure 5.9). Thus the relative weights of the various partial functions are different in the X-ray and neutron correlation functions (the X-ray correlation function, $T^{\mathrm{X}}(r)$, is usually more strongly dominated by the contributions involving heavier elements). Hence the use of both ND and XRD on a sample can reveal more than can be obtained by the use of one radiation alone. A detailed discussion of the combined use of ND and XRD is beyond the scope

of this chapter, but a good example of the method has been given by Benmore et al. [86] in a study of calcium aluminate glasses. Another good example of the application of the method can be found in a study of a high lead silicate glass, $80PbO{\cdot}20SiO_2$ [87], for which $T^N(r)$ is dominated by partials involving Pb or O, whilst $T^X(r)$ is dominated by partials involving Pb; simultaneous modeling of the two correlation functions provides information that is much more element-specific than is possible using only one radiation, and for the first time it has been possible to derive a detailed structural model showing how the lone-pairs of electrons are arranged relative to each other in a glass network containing lone-pair cations.

Another approach which has been used to differentiate the various partial contributions to the total correlation function is isomorphous substitution. This method involves performing diffraction on two samples that are identical, except that one element is substituted for another, and the two elements are assumed to be structurally identical. Mostly this approach has been applied to amorphous metals [88], although it has also been applied successfully to investigate the environment of rare earth (RE) ions in phosphate glass. [89] Clearly the requirement that the two substituted elements are structurally identical is a limitation of the technique, but RE elements are probably the best suited of all to this technique.

In some cases, ND can be used in more novel, specialized ways to obtain element-specific information. For example, a magnetic difference ND technique has been applied to directly observe the distribution of Tb–Tb distances in a phosphate glass, $24.6Tb_2O_3{\cdot}72.2P_2O_5{\cdot}3.2Al_2O_3$ [90]. First, the ND pattern was measured with the sample at a temperature 4 K, with the sample in the paramagnetic state. Second, the ND pattern was measured again, after application of a high magnetic field of 4 T, which is large enough to cause a high degree of alignment of the Tb magnetic moments. Figure 5.28a shows the two measured diffraction patterns, whilst Figure 5.28b shows their difference. In the absence of a magnetic field, with the sample in the paramagnetic state, there is no correlation between the orientations of pairs of Tb magnetic moments, and hence there is no structural information in the magnetic contribution to the scattering. However, with the high applied magnetic field, there is a high degree of alignment of the magnetic moments, with the result that the magnetic scattering contains structural information. Thus the difference shown in Figure 5.28b depends exclusively on Tb–Tb correlations. Figure 5.29a shows the differential correlation function, $D^N(r)$, measured before and after application of the magnetic field, whilst Figure 5.29b shows their difference, together with a simulation of the first two peaks. The first peak at 3.9 Å is due to pairs of Tb ions which are both bonded to the same non-bridging oxygen, whilst the second peak at 6.4 Å is due to two Tb ions which are bonded to different oxygens in the same PO_4 tetrahedron. Knowledge of the RE–RE distances in glass is of particular interest for laser and optoelectronic applications. Figure 5.29c shows a reverse Monte Carlo (see Section 5.4.9) simulation of the partial Er-Er differential correlation function for erbium metaphosphate glass [91] (together with an arbitrary scaling of $\Delta D^N(r)$); there is a remarkable agreement between the two independent results.

Diffraction with polarized neutrons can also be used to measure partial functions for magnetic materials [92]. However, it is worth noting that novel techniques which make use of magnetic scattering are limited to a very small Q-range (with Q_{max} in the range 5–10 $Å^{-1}$) due to the magnetic form factor (e.g., see Figure 5.26).

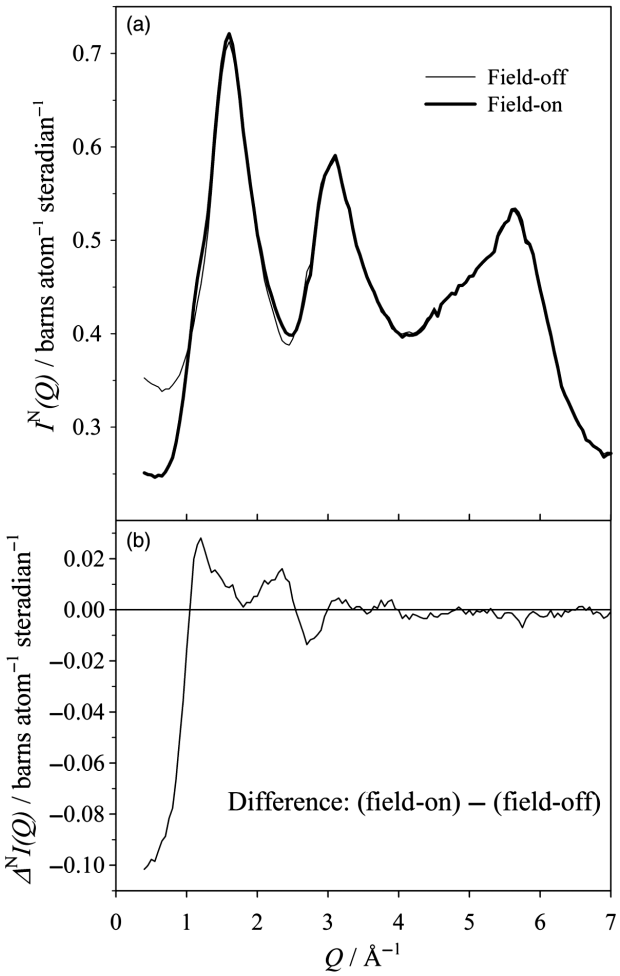

Figure 5.28. The differential cross-section for $24.6Tb_2O_3{\cdot}72.2P_2O_5{\cdot}3.2Al_2O_3$ glass at 4 K, showing (a) the diffraction pattern with and without the application of the 4 T magnetic field; and (b) the field-on minus field-off difference, $\Delta I^N(Q)$. [90].

For some elements it is also possible to measure partial functions using the anomalous dispersion technique. For this technique, it is necessary that the element of interest has a nuclear resonance at low energy (see Section 5.4.6.1). The method makes use of the fact that there is a strong wavelength-dependence of both the real and imaginary parts of the scattering length close to an absorption resonance. Although it is potentially a very powerful technique, anomalous dispersion is experimentally challenging, since it necessarily involves measurements for which absorption is very high, and thus far it has only been applied to glasses containing samarium ($14Sm_2O_3{\cdot}13Al_2O_3{\cdot}73GeO_2$ [93] and $20.5Sm_2O_3{\cdot}79.5P_2O_5$ [94, 95]).

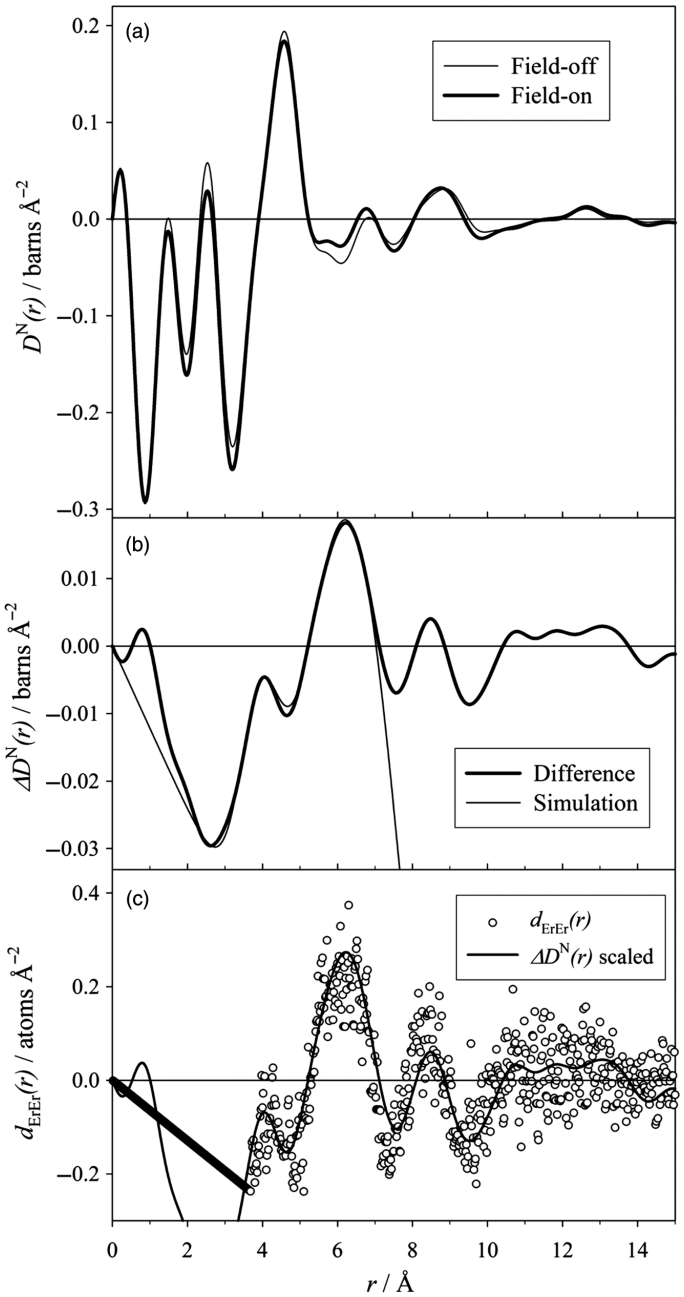

Figure 5.29. The differential correlation functions for $24.6Tb_2O_3{\cdot}72.2P_2O_5{\cdot}3.2Al_2O_3$ glass at 4 K [90], showing (a) the differential correlation function with and without the application of the 4 T magnetic field; (b) the field-on minus field-off difference, $\Delta D^N(r)$ (together with the simulation of the contribution from the first two distances described in the text); and (c) a reverse Monte Carlo simulation of the partial Er–Er differential correlation function for erbium metaphosphate glass [91] (together with an arbitrary scaling of $\Delta D^N(r)$).

5.4.8 Interpretation of Results

It is beyond the scope of this chapter to exhaustively review methods of interpretation of glass diffraction results. Instead a number of general concepts that are useful for gaining an understanding of ND results on glass structure are presented.

5.4.8.1 Crystallite Models The diffraction pattern of a glass consists of a series of peaks that are much broader than the sharp Bragg peaks normally measured for a polycrystalline powder (see Figure 5.16). However, it is well known that when crystallites become very small there is an observable broadening of the Bragg peaks, according to the Scherrer equation [96], which gives the FWHM of a Bragg peak as

$$\Delta Q = \frac{2\pi K}{L}, \tag{5.62}$$

where L is the crystallite dimension and K ($\sim$1) is a shape factor. Thus it has often been regarded as attractive to describe glass structure in terms of a model involving very small crystallites to account for the broad diffraction peaks [97–99]. Figure 5.30 shows the ND patterns of normal polycrystalline PdO and of hydrous PdO, which involves extremely small crystallites of diameter about 18 Å (illustrated by the inset to the figure) [100]. The simulation in the figure was calculated for a spherical particle of PdO of diameter 18 Å (inset) using the Debye equation (Eq. 5.28), and the SANS for this model was removed by use of Eq. 5.50, which is equivalent to placing the model in a hole in a homogenous medium of the same scattering length density. Even though the crystallites in hydrous PdO are extremely small, the diffraction pattern retains the broadened Bragg peaks of normal PdO, and it is also apparent from the differential correlation function (Figure 5.31) that the order extends to a relatively long distance compared to that observed in a glass. For a microcrystalline model to give a reasonable representation of diffraction results for a glass, it is necessary that the crystallite dimension be of order one unit cell, in which case there is no translational symmetry and the model ceases to be crystalline. Thus microcrystalline models of glass structure are not viable, because the crystallites contain too few unit cells to be considered crystalline, and because they lack a description of the region between crystallites [101] (see also Section 5.4.5.1). Instead, disordered models involving a distribution of atomic sites are to be preferred, such as the random network model [99, 101–103] which is commonly used to describe the structure of covalently bonded glasses.

5.4.8.2 Bonding and Bond Lengths When planning an ND experiment on a glass, it is useful to estimate the nearest neighbor distances likely to be observed; it can be preferable to choose to study a system in which there is little or no overlap between the nearest neighbor peaks in the correlation function, because then the peak parameters (e.g., bond lengths and coordination numbers) can be determined more reliably. This can be done by reference to the structure of crystalline materials of similar composition, or by use of tabulated values for the sizes of atoms. The ionic radii provided by Shannon [104] are often used for this purpose; for example, the ionic radii of Ge^{4+} and O^{2-} (with coordination numbers of 4 and 2, respectively) are 0.390 Å and 1.35 Å, giving a Ge–O

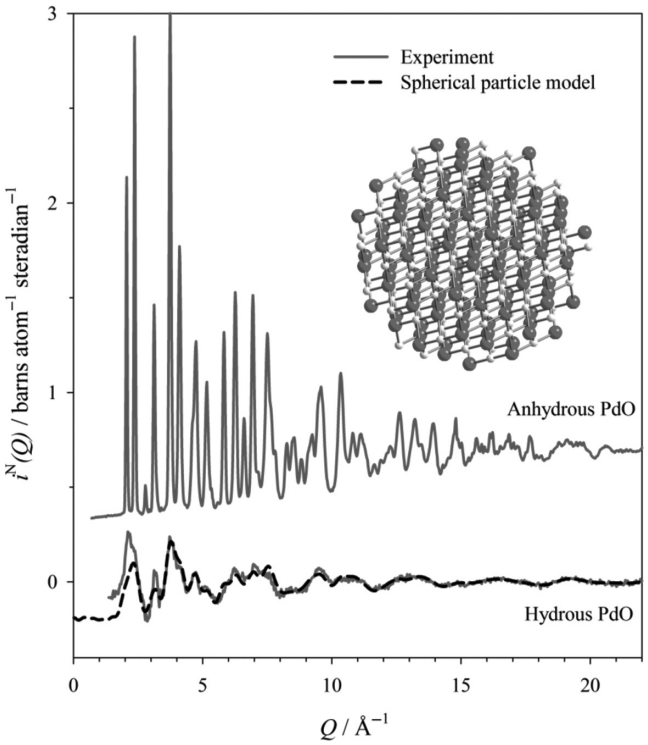

Figure 5.30. The measured distinct scattering (thick grey lines), $i^N(Q)$, for anhydrous PdO (vertically offset) and for hydrous PdO [100]. Also shown (thin black line) is a simulation of $i^N(Q)$ for a spherical particle of PdO of diameter 18 Å (inset) embedded in a homogenous medium.

distance of 1.74 Å, which is a good estimate of the bond length in GeO_2 glass (see Table 5.3). For amorphous metals, it is usual to make use of the Goldschmidt radii for 12-fold coordination [105], simply because coordination numbers in metals are usually much larger.

Electrostatic bond strength (EBS) is another very simple concept, first proposed by Pauling [106], which can be of great use in understanding glass networks. If a cation with formal charge ze is coordinated by ν anions (all of the same type), then the bond going from the cation to each anion has an EBS, s, defined as

$$s = \frac{z}{\nu}. \tag{5.63}$$

Pauling [107] postulated that in a stable structure the magnitude of the formal charge, $-\zeta e$, of an anion is exactly or nearly equal to the sum of the strengths of the bonds to it from the adjacent cations, so that

$$\zeta = \sum_k s_k = \sum_k \frac{z_k}{\nu_k}. \tag{5.64}$$

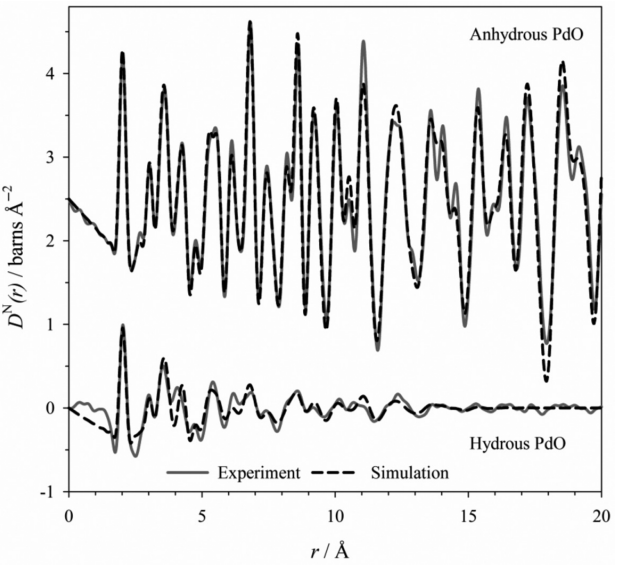

Figure 5.31. The measured differential neutron correlation function (thick grey lines), $D^N(r)$, for anhydrous PdO (vertically offset) and for hydrous PdO [100]. Also shown are simulated (see text) differential neutron correlation functions (thin black lines).

This criterion may be considered to be an expression of the necessity for charge balance in stable structures. It is of great use in determining which anion environments are likely to occur [47, 108].

The neutron correlation function, $T^N(r)$, provides information on the distribution of interatomic distances which can be much more detailed than a single bond length, and the concept of bond-valence (BV) can be of great use in obtaining a more profound understanding of the results. BV is an empirical concept, based on information from a large number of crystal structures, according to which the valence of an atom, i, may be expressed in the form

$$V_i = \sum_j v_j = \sum_j \exp\left(\frac{R_{ij} - d_{ij}}{b}\right), \tag{5.65}$$

where the summation is performed over its neighbors, j. d_{ij} and v_{ij} are respectively the length and the valence of the bond between atoms i and j. R_{ij} is the BV parameter for the atom pair (i,j) (tabulated values for R_{ij}, based on numerous crystal structures, are given by Brese and O'Keeffe [109]) and b is a universal constant (= 0.37Å). If we make the simplifying assumption that all of the n_{ij} neighbors to atom i have the same bond length, r_{ij}^{bv}, then this interatomic distance is given by

$$r_{ij}^{bv} = R_{ij} + b \log_e\left(\frac{n_{ij}}{V_i}\right). \tag{5.66}$$

Although the BV method has been developed for crystal structures [110], it is becoming increasingly clear that it is a powerful tool for understanding glass structure [111]. Equation 5.66 shows that the bond length increases as the coordination number increases. For example, for Ge–O coordination numbers of 4, 5, and 6, Eq. 5.66 predicts Ge–O bond lengths of 1.7480, 1.8306, and 1.8980 Å, respectively [16]; thus the appearance of a shoulder on the right hand side of the Ge–O peak for $18Cs_2O.82GeO_2$ glass (in Figure 5.20b) is clearly associated with the presence of a significant fraction of germanium atoms with a coordination number greater than four. The BV method is also of great use in considering the environment of bridging oxygens, especially in glasses such as tellurites in which there can be a large difference in the lengths of the bonds [64, 112].

5.4.8.3 Coordination Polyhedra As well as understanding the bond lengths (or interatomic distances) between pairs of atoms in the glass, it is also of interest to understand the geometry of the coordination shell around each atom, that is the coordination polyhedron of each atom. For example, we may wish to determine the number and geometry of anions X (e.g., O^{2-}) around a cation A (e.g., Si^{4+}) in a glass.

Obviously the coordination number for each type of atom is of great relevance for a consideration of the coordination polyhedra. However, it must be acknowledged that coordination numbers cannot usually be measured as accurately as the bond lengths. As discussed in Section 5.4.4, the accuracy of the coordination numbers depends on many factors, including the sample composition and density, and in the most favourable cases coordination numbers can now be measured to within about 1% of the expected value (e.g., see the fit results for GeO_2 in Table 5.3, or the results for crystalline α-TeO_2 [112] which give $n_{TeO} = 3.95(3)$, compared to the expected value of four), but in less favourable cases the accuracy will not be as good as this, for example if the sample contains any hydrogen. As illustrated by the small errors on the bond lengths in Table 5.3, the interatomic distances in a sample can be measured very accurately, especially if their distribution is symmetric, as would be obtained if the distribution of static distances is very narrow. (In fact, the bond lengths obtained from the neutron correlation function are a true measure of the bond lengths in a material, because the effects of correlated motion are treated correctly. This is in contrast to standard crystallographic methods, which do not allow for correlated atomic motion, and hence sometimes underestimate bond lengths [113]).

It follows from the discussion of the previous paragraph that it is important not to rely solely on measured coordination number to determine the coordination polyhedron, but also to consider the longer interatomic distances in the polyhedra (i.e., X–X). The r_{XX}/r_{AX} ratio (or the X-Â-X bond angle) are very important signatures of the basic structural units in the glass. For example, if r_{XX}/r_{AX} is close to 1.6330 (implying a bond angle close to 109.47°), then this is strong evidence that the basic structural unit is a tetrahedron, which is the most common unit in network glasses.

Table 5.5 gives the structural properties of some simple coordination polyhedra with coordination numbers of six or less, since these are relevant for glass forming cations in network glasses. These structural units are also shown in Figure 5.32. All of the values

TABLE 5.5. Structural properties of coordination polyhedra in network glasses (see Figure 5.32).

Unit	Coordination number, n_{AX}	Distance ratio(s), r_{XX}/r_{AX}	Radius ratio, r_A/r_X	Bond angle(s), X-Â-X	Example(s)
Triangle AX_3	3	1.7321	0.1547	120°	B_2O_3 [12]
Trigonal pyramid AX_3	3	$2\sin(\theta/2)$	$(1/\sin(\theta/2))-1$	θ	As_2O_3 [118], tellurites [119]
Tetrahedron AX_4	4	1.6330	0.2247	109.47°	Silicates [120], GeO_2 [16], $GeSe_2$ [84], GeS_2 [121], phosphates [43], aluminates [122], gallates [123]
Disphenoid AX_4	4	1.4142, 2.0	0.4142	90°, 180°	Tellurites [124] [125]
Trigonal bipyramid AX_5	5	1.7321, 1.4142	0.1547, 0.4142	90°, 120°, 180°	Germanates [16]
Square pyramid-based AX_5	5	planar ~1.4, 2.0 apical ~1.5	planar ~0.43 apical ~0.31	planar ~90°, 160° apical ~100°	Ti in $K_2O{\cdot}TiO_2{\cdot}2SiO_2$ [114]
Octahedron AX_6	6	1.4142, 2.0	0.4142	90°, 180°	Ca in $48CaO{\cdot}49SiO_2{\cdot}\ 3Al_2O_3$ [82], germanophosphates [126]

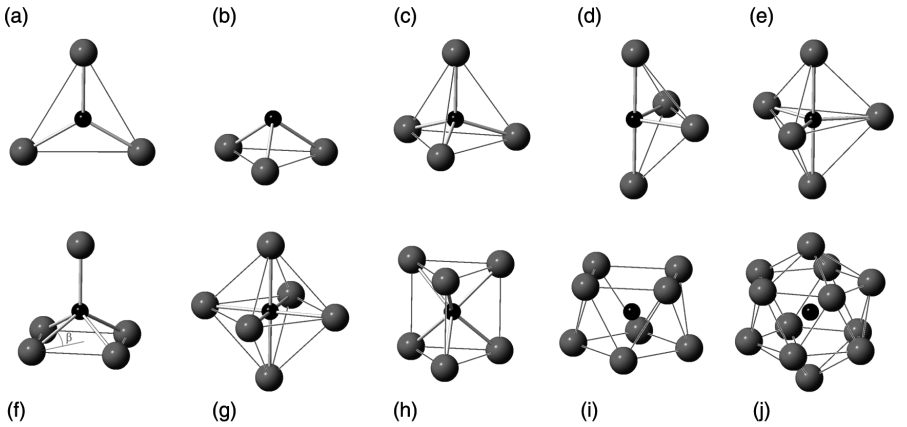

Figure 5.32. Important examples of coordination polyhedra for glasses. (a) AX_3 triangle; (b) AX_3 trigonal pyramid; (c) AX_4 tetrahedron; (d) AX_4 disphenoid; (e) AX_5 trigonal bipyramid; (f) AX_5 square pyramid-based unit; (g) AX_6 octahedron; (h) AX_6 trigonal prism; (i) AX_8 Archimedean antiprism; (j) AX_{12} icosahedron.

in Table 5.5 are given for a regular, undistorted unit, in which all A–X distances are the same, and all equivalent pairs of X atoms have the same separation, r_{XX} (for the square pyramid the values are based on a reasonable angle value, $\beta \sim 10°$). If the units are not distorted, then the bond angle θ is given by

$$\theta = 2\sin^{-1}\left(\frac{r_{XX}}{2r_{AX}}\right), \tag{5.67}$$

and if the atoms are considered to be spheres in contact then their radius ratio is

$$\frac{r_A}{r_X} = \frac{2r_{AX}}{r_{XX}} - 1. \tag{5.68}$$

The assumptions of equal A–X distances and equal equivalent X–X distances are likely to be least good for the square pyramid-based AX_5 unit, for which it is highly likely that the apical A–X distance will be markedly different from the other bond lengths. For example, in $K_2O{\cdot}TiO_2{\cdot}2SiO_2$ [114] Ti occurs in TiO_5 square pyramid units with four bridging Ti–O bonds of length 1.96 Å to oxygens in the plane, and a non-bridging titanyl Ti=O bond of length 1.65 Å to an apical oxygen. Similarly, the presence of terminal oxygens in P_2O_5 and phosphate glasses leads to relatively large distortions of the PO_4 units from the geometry of an ideal tetrahedron [44]. Also, in AX_6 octahedra there is likely to be a difference between equatorial and axial A–X bond lengths due to the Jahn–Teller effect. Similarly, there is a pronounced difference between the equatorial and axial Te–O bond lengths in a TeO_4 disphenoid [112]. Nevertheless, despite the distortions of the units that occur in many materials, it is still a useful starting point to

consider the ratio of distances (or the bond angle) as an important stage in identifying the coordination and geometry around the atoms in a glass.

For amorphous metals and for larger modifier cations in network glasses, polyhedra with larger coordination numbers than those given in Table 5.5 are usually appropriate (e.g., trigonal prism, Archimedean antiprism, icosahedron—see Figure 5.32) [115–117].

5.4.8.4 Comparison with Crystalline Structures Glasses are structurally different from crystals (see sections 4.5.1 and 4.8.1). However, the same interatomic potentials (or bonding interactions) occur between atoms, regardless of whether they are in a glass or in a crystalline solid, and therefore the local structure in a relevant crystal can provide a useful indication of the local structure in a glass. Nevertheless, sometimes there are important structural differences between glasses and crystals; for example, B_2O_3 glass contains a large proportion of highly planar B_3O_6 boroxol groups, but these superstructural units are not found in the crystalline forms of B_2O_3 [12]. Therefore, ND results on a glass should be compared critically with related crystals, rather than simply assuming that the local structure is exactly the same. For example, the addition of modifier to GeO_2 usually leads to crystal phases in which there are octahedrally coordinated germanium atoms, but there is evidence that in the corresponding glasses the higher coordination may be more uniformly distributed due to the formation of 5-coordinated germanium atoms [16].

For a full comparison of ND results for a glass with a crystal structure, it is essential to simulate $T^{N}(r)$ for the crystal structure [127], taking into account both the real-space resolution of the measurement, and the broadening effect of atomic motion. The effect of real-space resolution is included in the simulation by convoluting the ideal correlation function of the crystal (i.e., the correlation function calculated from the crystallographic positions of the atoms) with the resolution function appropriate to the experimental measurement. This resolution function depends on the modification function, and in particular the value of Q_{max} used in the Fourier transformation of the experimental data (see Section 5.4.2.2). The effect of thermal motions of the atoms is included in the simulation by convoluting the ideal partial correlation functions of the crystal with a Gaussian whose standard deviation is $\langle u_{ll'}^2 \rangle^{1/2}$, the RMS variation in distance between a pair of atoms of types l and l'. Due to the effects of correlated motion, the thermal width $\langle u_{ll'}^2 \rangle^{1/2}$ is a function of distance, r, with smaller values for short distances [15]. For example, a reasonable simulation of the correlation function of the quartz form of GeO_2 can be obtained with a thermal of 0.040 Å for Ge–O bonds, and 0.100 Å for all longer distances between Ge and O atoms.

It is an intricate procedure to simulate the correlation function of a crystal, and a computer program, XTAL, is available on the internet for this purpose [128, 129]. Examples of the use of this program are shown in Figure 5.31 and Figure 5.33b and c.

5.4.8.5 The First Sharp Diffraction Peak The peak in the diffraction pattern of a glass with the smallest Q-value is usually the sharpest peak (e.g., see Figure 5.11 or 5.13), and this so-called *first sharp diffraction peak* (FSDP) has attracted a great deal of attention [130]. Since the FSDP occurs at the lowest Q-value of any diffraction

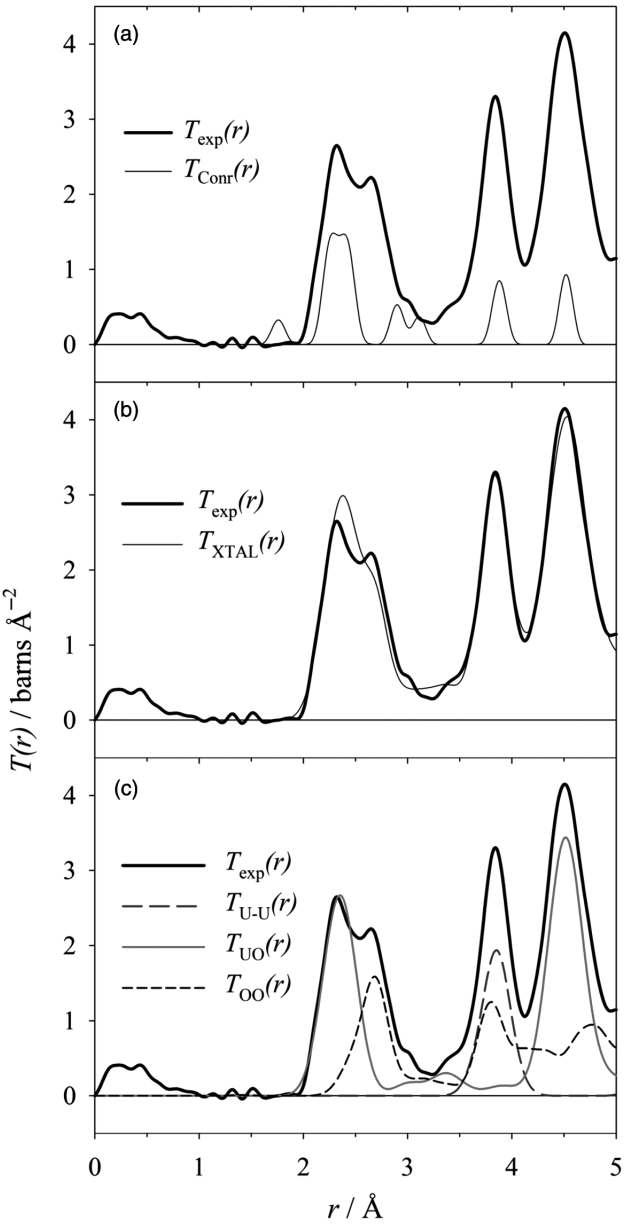

Figure 5.33. The total neutron correlation function, $T^N(r)$, of crystalline U_4O_9. (a) The experimental correlation function, $T_{exp}(r)$, compared with the U–O and U–U contributions, $T_{Conr}(r)$, as determined by EXAFS [163]. (b) The experimental correlation function, compared with the total neutron correlation function, $T_{XTAL}(r)$, simulated from the crystallographically determined structure of U_4O_9 [160]. (c) The experimental correlation function, compared with the partial components of $T_{XTAL}(r)$ [160].

peak, it relates to the longest "periodicity" in the glass structure. Furthermore, if the first peak is the sharpest peak, then it is also the most slowly decaying correlation in real space. Thus, the FSDP relates to the longest range order that exists in the glass (in the absence of microstructure, which gives rise to small angle scattering), and this is why it has received special attention, as key evidence for *intermediate range order* (IRO). Furthermore, the FSDP has physical properties (e.g., temperature-dependence) that are anomalous, and similar in different glass systems, which some workers interpret as evidence of a universal phenomenon.

Wright has shown that the low Q side of the FSDP is well described by a Lorentzian, which provides a convenient form with which to fit the peak and to determine its position, Q_1, width, and height [101]. There have been many phenomenological studies of the way in which the properties of the FSDP depend on other parameters, such as composition, pressure, etc., but these have shed little light on its origin. There is a longstanding interpretation of the FSDP as arising from crystalline-like layers in the glass structure [131, 132], such that its position is $Q_1 \sim 2\pi/L$, where L is the inter-layer spacing. More recently a view has emerged which is more consistent with the non-crystalline structure of glass, in which the FSDP results from the periodicity arising from the boundaries between a succession of the cages which comprise the structure of a three-dimensional covalent network [133]. Alternatively, Elliott [134] has interpreted the FSDP as arising from the arrangement of the voids in the network structure, but this is essentially equivalent to the cage interpretation, since it is the contrast between the voids and their boundaries that gives rise to the FSDP (as for small angle scattering—see Section 5.4.5.2).

5.4.9 Modeling

The clearest information on a glass that can be obtained by ND concerns the short range order (SRO). The interatomic distances and coordination numbers derived from ND are potentially more accurate than for any other experimental technique, and much of this chapter describes the means by which they may be determined reliably, so that the coordination polyhedra can be investigated. Nevertheless, the way in which the structural units connect together to form the extended structure of the glass (i.e., the intermediate range order, IRO) is also of considerable interest. However, as the interatomic distance, r, increases, the peaks in the correlation function become closer together, and their thermal widths become larger because there is less correlation between the atomic motions [15]. Hence there is increasing overlap of the peaks at higher r, with the result that ND is sensitive to IRO in a more subtle way than for SRO, and it is necessary to employ modeling techniques to make progress with the investigation of IRO.

The ideal modeling solution would be to determine the three-dimensional position of every atom relative to the other atoms in the sample. In principle, this is feasible when performing single-crystal diffraction because information is obtained as a function of the momentum transfer vector, $\boldsymbol{Q}$. However, glasses are usually isotropic, or almost isotropic, with the result that the measured diffraction pattern is condensed down to a function of a single variable, the magnitude of the momentum transfer, $Q = |\boldsymbol{Q}|$; that is, the measured distinct scattering, $i(Q)$, is an average over all possible orientations of the sample relative to the incident neutron beam. This results in a loss of information so that

it is not possible to deduce the positions of all the atoms in the sample.[2] Conversely, there may be an enormous number of different sets of atomic coordinates which would all give rise to the same observed distinct scattering, *i(Q)*. This situation is called the *uniqueness problem*. For a structural model of a glass to be correct it is necessary that it agrees with the observed diffraction pattern. However, if a model is consistent with the diffraction pattern, this is not proof that the model is right—it is merely evidence that the model is not wrong. Thus, unique structure determination is not possible.

The random network model for the structure of covalent glasses was proposed by Zachariasen in 1932 [102], and this provides a description of the SRO in a glass in terms of structural units which connect together with a degree of randomness (such as a distribution of bond angles and dihedral angles). Originally there was some doubt whether it was possible to form an extended three-dimensional structure on the basis of the model, and this concern was allayed by the early ball-and-stick modeling technique. A ball-and-stick model would be constructed by hand, and then photographed from more than one direction so that the coordinates of the atoms could be digitized [135, 136]. A similar approach was adopted for metallic glasses, in which a dense random packing of hard spheres was modeled by filling a bag with ball bearings [137]. The correlation functions of these models showed reasonable agreement with experiment. However, the method is laborious, and has largely been superseded by computer modeling methods. It is worth noting that most computer modeling methods make use of periodic boundary conditions, and hence the model needs to be sufficiently large that its crystalline nature is not a problem; according to the minimum image convention, this may be achieved if the size of the unit cell is twice the longest significant distance in the glass [138].

Recent years have seen the development of techniques for obtaining structural models of disordered materials in which a computer programme is used to move atoms around inside a box so as to optimize the agreement with diffraction data. The most widespread of these is the reverse Monte Carlo (RMC) method in which the atoms are moved according to a variant of the standard Monte Carlo algorithm [138]; a move which improves agreement with diffraction data is accepted, but if the move worsens the agreement then it may be rejected or accepted according to a probability factor [139, 140]. Thus the aim is to produce a model for which the deviation from experiment has been minimized (whereas for the standard Monte Carlo method it is the energy that is minimized). For a large number of atoms, N (say $N \sim 1000$ or more), there are $3N$ parameters; with such a large number of parameters a very close fit to the diffraction data can potentially be obtained. According to the "uniqueness problem" there are many models which may be produced by this method, and in fact it tends to produce the most disordered model that is consistent with the diffraction data (and constraints) [141]. Thus early RMC models of glass were not consistent with what was already known about glass structure; for example, for SiO_2 glass, which is well described as a random network of corner-sharing SiO_4 tetrahedra, many of the silicon atoms were 3- or 5-coordinated, or had a 4-coordinated coordination polyhedron which was not tetrahedral [142].

[2] Also the study of crystalline structures has the huge advantage that it is only necessary to determine the coordinates of the atoms in one unit cell, which is then reproduced by translations to build up the full three-dimensional structure.

In response to the problems with early RMC models, the method was developed to include constraints; for example, there can be restrictions on the distances between a pair of atom types, or restrictions on the coordination numbers for a pair of atom types [143]. There have also been other variations on the RMC method, such as the inclusion of a constraint based on BV [144] (see Section 4.8.2), which are intended to produce more reasonable models. A more recent RMC variation, which appears promising, minimizes the difference from diffraction for each of the individual atomic sites (whereas the standard RMC method minimizes the difference from diffraction for the average atomic site) [145]. With the addition of constraints, the RMC method has been able to produce structural models which are consistent with diffraction data and are consistent with what is already known about the nature of bonding in materials. However, the danger introduced by the use of constraints is that the RMC simulation can no longer sample configurations with different IRO (e.g., different ring statistics) to the starting model; RMC is then a means of refining a starting model so that it has better agreement with experiment, rather than a means of finding a fundamentally new model [140, 146].

A rather different method of modeling glass structure is provided by molecular dynamics (MD) simulations [147, 148]. This involves filling a box with atoms, and determining their trajectories by solving Newton's equations of motion, using a particular set of assumed potentials to describe the interactions between the various pairs of atoms. Usually the system is simulated at a very high initial temperature so that it is liquid, and then the temperature is reduced to mimic the quenching of a glass; an inherent difficulty with the technique (due to computer limitations) is that the melt is quenched at a very high rate ($\sim 10^{12}$ K/s), which is much faster than for the quenching of real glasses ($\sim 1 - 10^{6}$ K/s). A common problem with the use of MD to simulate glass is that the comparison with experiment is cursory: one reason for this is that it is difficult to know how to change the input potential to improve the agreement. However, it is essential that models are compared quantitatively with experiment to assess their worth [149]. A promising new development is thus the use of RMC to refine an MD model so that it agrees well with diffraction data [150]. The DL_POLY package is perhaps the most widely used MD software for glass simulation, and is readily available on the internet [151]. DL_POLY performs classical MD simulations which use empirical potentials, but a more recent development has been *ab initio* MD, which calculates the forces between the atoms using quantum mechanics—a parameter-free, first-principles approach [152, 153].

In the early days of RMC, the debate about the legitimacy of the method was almost theological in character [154]. One criticism of the method is that it is unphysical, and in particular that it does not involve the use of a potential. The aim of modeling a glass structure is to produce a model that is consistent with all the available experimental data, by whatever means the model is produced; in this author's opinion, it is ironic that RMC was criticized for producing models without the use of a potential, when those models agree well with experiment, whereas MD modeling (which does use a potential) is often unable to closely reproduce diffraction data. Nevertheless, this criticism was recently addressed by the development of the empirical potential structure refinement (EPSR) modeling technique [155]. This method is similar to RMC, but with the important difference that the atoms are moved around in the box by use of the Monte Carlo method, using potentials to describe the interatomic interactions, and then the potentials

are adjusted to optimize the agreement with diffraction data. Significantly, there is little requirement for constraints and the structural model obtained is not dependent on the assumptions used to form the initial model. Nevertheless, the method is more successful if XRD data can be used, in addition to ND data, and an excellent example of this has recently been given in a study of $80PbO.20SiO_2$ glass by Alderman et al. [87].

A striking example of a successful result from the use of RMC has already been mentioned in Section 5.4.7.2. The structure of several RE metaphosphate glasses was simulated by RMC, using experimental data from both ND and XRD [91]. At the same time a completely independent study used ND with a magnetic difference technique to isolate the Tb–Tb correlation function in a terbium metaphosphate glass [90], and it was found to show a remarkable similarity to the RE–RE partial function from the RMC study (see Figure 5.29). The results of a diffraction experiment depend on the distances between pairs of atoms in the sample, and so they can be used to determine a two-body correlation function. Thus RMC simulation of diffraction data has the potential to be able to extract two-body correlations well, as shown by the example of RE–RE correlations in metaphosphate glasses. However, the IRO in a glass (e.g., the distribution of rings) is characterized in terms of many-body correlations, which are not measured directly by diffraction. Thus diffraction is sensitive to IRO in an indirect way—essentially information about IRO is built up from diffraction results by a process of "triangulation" of the various pairwise distances (as for the determination of coordination polyhedra, see Section 5.4.8.3). For example, as yet, RMC [156, 157] and EPSR [158] have been unable to reliably extract information on the presence of boroxol rings in B_2O_3 glass, in contrast with what is known from other experimental techniques, such as Raman scattering and NMR [12].

5.4.10 The PDF Method

The analysis of diffraction data by Fourier transformation to a real-space correlation function was first used in a study of a crystalline form of sulphur in 1934 [159], but for the next few decades the approach was developed almost entirely for the study of non-crystalline samples (glasses and liquids), whilst almost all diffraction studies of crystalline materials used reciprocal-space analysis methods, such as Rietveld refinement [73]. However, in recent years the real-space correlation function method has increasingly been applied to the study of crystal structures, in which case the method is often called the *PDF* (pair distribution function) *method* [19, 20]; the function which is called the PDF in such studies is usually the differential correlation function, $D^N(r)$, introduced above in Eq. 5.34. The reason for using $D^N(r)$, rather than $T^N(r)$ which is generally preferred for glasses, is that the differential correlation function is better suited to the display of the much greater order at longer range in crystals (for example, see Figure 5.31). The PDF method has proved very useful for structural investigations of disordered crystals (i.e., crystals in which the contents of the unit cells are not all exactly the same, and for which the local structure may differ from the average structure), and sometimes it is even useful for ordered crystals. Although "the PDF method" essentially concerns the structure of crystalline materials, there is currently increasing overlap between the study of the structure of non-crystalline materials and of disordered crystalline materials, and thus it is useful for a glass scientist to be aware of the method.

A brief illustration of the PDF method is given here using crystalline U_4O_9 as an example of its use [160], because this is of at least some passing interest to glass scientists due to the proposed presence of a "glassy part" in the structure, and the use of X-ray spectroscopy.

Crystalline UO_2 has the calcium fluorite structure, in which each uranium atom has eight oxygen neighbors at a distance 2.368 Å, whilst the oxygen atoms are separated by 2.734 Å [160]. By means of a modification of the UO_2 structure, a larger concentration of oxygen can be incorporated, resulting in the formation of U_4O_9. The crystal structure of U_4O_9 has been determined by single-crystal ND [161, 163], and the oxygens are arranged around the center of a vacant cube with the geometry of a cuboctahedron. The unit cell of U_4O_9 is relatively large and complex, containing 828 atoms on average, with mean coordination number and bond length $n_{UO} = 8.328$ and $r_{UO} = 2.354$ Å, respectively. However, a radically different structural view emerged on the basis of a XAFS study, using the uranium L_{III} edge [163]. The results were interpreted as showing first that there is separation into two phases, one with the UO_2 structure, and one which is glassy and is *spectroscopically invisible* (i.e., with a distribution of U–O bond lengths which is too broad to be observed by XAFS), and secondly that there are short oxo bonds (i.e., terminal U=O bonds) in the material. Figure 5.33 shows the total neutron correlation function, $T_{exp}(r)$, which was measured for a sample of U_4O_9 [160]. The first two peaks at around 2.33 Å and 2.66 Å arise from U–O and O–O correlations, respectively. It is important to note that ND is sensitive to all atomic pairs in the sample, and there is no possibility of a portion of the sample that is spectroscopically invisible. Figure 5.33a also shows a simulation of the total neutron correlation function, $T_{Conr}(r)$, calculated according to the results of the XAFS study [163]. Firstly, it should be noted that whereas the XAFS results give rise to a peak at 1.76 Å due to oxo bonds, there is no such peak in the ND measurement. Figure 5.33b shows a simulation of the total neutron correlation function, $T_{XTAL}(r)$, calculated from the known crystal structure of U_4O_9 using the XTAL program [128, 129], and Figure 5.33c shows the three partial contributions to the simulation. This simulation gives a fairly good account of the observed $T_{exp}(r)$; there are small differences, which may arise because the local structure is not exactly the same as the average structure. Nevertheless, the similarity of peak areas shows that the observed $T_{exp}(r)$ is consistent with a coordination number, n_{UO}, similar to that of the crystallographic result. The XAFS results are sensitive to U–O and U–U correlations, but not O–O correlations. In practice, this means that the XAFS simulation, $T_{Conr}(r)$, in Figure 5.33a should give a full account of the experimental correlation function only in the region of the U–O peak at around 2.33 Å. However, the XAFS results underestimate the area under $T_{exp}(r)$ in this region by a factor of order two, that is, the XAFS results severely underestimate the U–O coordination number. Thus the ND results [160] do not support the structural conclusions based on the XAFS results [163]; no evidence was found for oxo bonds or a glassy component of the structure in U_4O_9.

An important reason why XAFS studies can give highly inaccurate coordination numbers is that there is a very high correlation between the coordination number and the variation in bond length. This high correlation arises because of the lack of information in the low momentum transfer region for XAFS results. For the simulation shown in Figures 5.33b and c, the thermal variation in interatomic distances was adjusted empirically to

optimize the agreement with the experimental measurement, leading to $\langle u^2_{U-U}\rangle^{1/2} = \langle u^2_{O-O}\rangle^{1/2} = 0.1$ Å and $\langle u^2_{U-O}\rangle^{1/2} = 0.13$ Å [160]. These values are in contrast to the Debye–Waller factors from the XAFS experiment which are typically 0.045 Å [163]. Thus the probable reason for the highly inaccurate coordination numbers from the XAFS study is that a poor value was chosen for the Debye–Waller factor, and indeed an earlier XAFS study [164] of U_4O_9 used Debye–Waller factors in closer agreement with those obtained from the crystallographic simulation, $T_{XTAL}(r)$, and also gave coordination numbers which are closer to the expected values.

Considerable structural insight can be gained by making a detailed comparison of a measured correlation function for a glass with the simulation for a related crystal structure. The model correlation function, $T_{XTAL}(r)$, shown in Figure 5.33b was calculated using the program XTAL [128] which is available on the internet [129] and can be used to simulate neutron or X-ray correlation functions for either crystalline or non-crystalline model structures. For PDF studies of crystalline materials other programs are also available. These include the program PDFfit [165], which essentially performs a structural refinement in real space (although the crystallographic symmetry is not maintained), and the program RMCprofile [166], which may be used to perform an RMC simulation for a crystalline structure.

ACKNOWLEDGMENTS

I am very grateful to Dr. Stuart Ansell (ISIS) for providing his prediction of the flux distribution of the ISIS methane moderator. Thanks are due to Dr. Isaac Abrahams and Dr. Tiziana di Cristina (Queen Mary, University of London) for use of their data on a phosphate glass. Dr. Uwe Hoppe (Rostock University) is thanked for providing his RMC simulation data for rare earth metaphosphate glasses. I am grateful to Professor Richard Walton (University of Warwick) for assistance with data on an amorphous zeolite precursor. Finally, Professor Adrian Wright (Reading University) is thanked for many illuminating discussions about neutron diffraction and glasses, including a discussion about the compressibility limit for silica glass for this chapter.

REFERENCES

1. H.E. Fischer, G.J. Cuello, P. Palleau, D. Feltin, A.C. Barnes, Y.S. Badyal, and J.M. Simonson, "D4c: A very high precision diffractometer for disordered materials," *Appl. Phys. A* **74**, S160–S162 (2002).
2. A.C. Hannon, "Results on disordered materials from the GEneral Materials diffractometer, GEM, at ISIS," *Nucl. Instrum. Meth. A* **551**, 88–107 (2005).
3. A.C. Wright, "The structure of amorphous solids by x-ray and neutron diffraction," *Adv. Struc. Res. Diffr. Meth.* **5**, 1–120 (1974).
4. G.L. Squires, *Introduction to the Theory of Thermal Neutron Scattering*, Cambridge University Press, Cambridge, 1978.

5. P.A.V. Johnson, A.C. Wright, and R.N. Sinclair, "Neutron scattering from vitreous silica II. Twin-axis diffraction experiments," *J. Non-Cryst. Solids* **58**, 109–130 (1983).
6. S.W. Lovesey, *Theory of Neutron Scattering from Condensed Matter. Volume* **1**., Clarendon Press, Oxford, 1984.
7. D.L. Price and K. Sköld, "Introduction to neutron scattering," In: *Neutron Scattering Part A*, K. Sköld and D.L. Price, eds. Academic Press, Orlando, 1986, pp. 1–97.
8. G. Placzek, "The scattering of neutrons by systems of heavy nuclei," *Phys. Rev.*, **86**, 377–388 (1952).
9. A.C. Wright, "Scientific opportunities for the study of amorphous solids using pulsed neutron sources," *J. Non-Cryst. Solids* **76**, 187–210 (1985).
10. M.A. Howe, R.L. McGreevy, and W.S. Howells, "The analysis of liquid structure data from time-of-flight neutron diffractometry," *J. Phys.: Condens. Matter* **1**, 3433–3451 (1989).
11. A.K. Soper, "Inelasticity corrections for time-of-flight and fixed wavelength neutron diffraction experiments," *Mol. Phys.* **107**, 1667–1684 (2009).
12. A.C. Hannon, D.I. Grimley, R.A. Hulme, A.C. Wright, and R.N. Sinclair, "Boroxol groups in vitreous boron oxide : New evidence from neutron diffraction and inelastic neutron scattering studies," *J. Non-Cryst. Solids* **177**, 299–316 (1994).
13. A.C. Hannon, E.R. Barney, and D. Holland, "The structure of tin borate based glasses," *Phys. Chem. Glasses Eur. J. Glass Sci. Technol. B* **50**, 271–283 (2009).
14. T.E. Faber and J.M. Ziman, "A theory of electrical properties of liquid metals III. Resistivity of binary alloys," *Philos. Mag.* **11**, 153–173 (1965).
15. I.K. Jeong, R.H. Heffner, M.J. Graf, and S.J.L. Billinge, "Lattice dynamics and correlated atomic motion from the atomic pair distribution function," *Phys. Rev. B* **67**, 104301 (2003).
16. A.C. Hannon, D. Di Martino, L.F. Santos, and R.M. Almeida, "Ge-O coordination in cesium germanate glasses," *J. Phys. Chem. B* **111**, 3342–3354 (2007).
17. B.E. Warren, H. Krutter, and O. Morningstar, "Fourier analysis of X-ray patterns of vitreous SiO_2 and B_2O_3," *J. Am. Ceram. Soc.* **19**, 202–206 (1936).
18. H.E. Fischer, A.C. Barnes, and P.S. Salmon, "Neutron and X-ray diffraction studies of liquids and glasses," *Rep. Prog. Phys.* **69**, 233–299 (2006).
19. S.J. Hibble, A.C. Hannon, and I.D. Fawcett, "Total neutron diffraction: The correct way to determine the true structure of crystalline materials?," *J. Phys.: Condens. Matter* **11**, 9203–9219 (1999).
20. S.J.L. Billinge and M.G. Kanatzidis, "Beyond crystallography: the study of disorder, nanocrystallinity and crystallographically challenged materials with pair distribution functions," *Chem. Comm.* 749–760 (2004).
21. D.A. Keen, "A comparison of various commonly used correlation functions for describing total scattering," *J. Appl. Cryst.* **34**, 172–177 (2001).
22. L van Hove., "Correlations in space and time and Born approximation scattering in systems of interacting particles," *Phys. Rev.* **95**, 249–262 (1954).
23. L.N.G. Filon, "On a quadrature formula for trigonometric integrals," *Proc. Roy. Soc. Edinburgh* **49**, 38–47 (1929).
24. B.H. Toby and T. Egami, "Accuracy of pair distribution function analysis applied to crystalline and non-crystalline materials," *Acta Cryst. A* **48**, 336–346 (1992).
25. M.G. Tucker, M.T. Dove, and D.A. Keen, "MCGRtof: Monte Carlo G(r) with resolution corrections for time- of-flight neutron diffractometers," *J. Appl. Cryst.* **34**, 780–782 (2001).

26. A.C. Hannon, W.S. Howells, and A.K. Soper, "ATLAS: A suite of programs for the analysis of time-of-flight neutron diffraction data from liquid and amorphous samples," *Inst. Phys. Conf. Ser.* **107**, 193–211 (1990).
27. H.H. Paalman and C.J. Pings, "Numerical evaluation of x-ray absorption factors for cylindrical samples and annular sample cells," *J. Appl. Phys.* **33**, 2635–2639 (1962).
28. A.K. Soper, "*GudrunN and GudrunX : Programs for Correcting Raw Neutron and X-ray Diffraction Data to Differential Scattering Cross Section,*" Rutherford Appleton Laboratory Technical Report RAL-TR-2011-013, 2011.
29. A.K. Soper, Delight in Disorder, https://www.facebook.com/disord.matt (Last accessed on 27 July 2015).
30. S.S. Sidhu, L. Heaton, D.D. Zauberis, and F.P. Campos, "Neutron diffraction study of titanium-zirconium system," *J. Appl. Phys.* **27**, 1040–1042 (1956).
31. A.C. Wright, "Neutron and X-ray Amorphography," In: *Experimental Techniques of Glass Science*, C.J. Simmons and O.H. El-Bayoumi, eds. American Ceramic Society, Westerville, 1993, pp. 205–314.
32. V.F. Sears, "Neutron Scattering Lengths and Cross Sections," *Neutron News* **3**, 26–37 (1992).
33. D.I. Grimley, A.C. Wright, and R.N. Sinclair, "Neutron scattering from vitreous silica IV. Time-of-flight diffraction," *J. Non-Cryst. Solids* **119**, 49–64 (1990).
34. X.Y. Qiu, E.S. Bozin, P. Juhas, T. Proffen, and S.J.L. Billinge, "Reciprocal-space instrumental effects on the real-space neutron atomic pair distribution function," *J. Appl. Cryst.* **37**, 110–116 (2004).
35. A.K. Soper, W.S. Howells, and A.C. Hannon, "*ATLAS - Analysis of Time-of-Flight Diffraction Data from Liquid and Amorphous Samples*.," Rutherford Appleton Laboratory Report RAL-89–046, 1989.
36. J. Waser and V. Schomaker, "The Fourier inversion of diffraction data," *Rev. Mod. Phys.* **25**, 671–690 (1953).
37. E. Lorch, "Neutron diffraction by germania, silica and radiation-damaged silica glasses," *J. Phys. C* **2**, 229–237 (1969).
38. R.L. Mozzi and B.E. Warren, "The structure of vitreous silica," *J. Appl. Cryst.* **2**, 164–172 (1969).
39. D.T. Bowron, R.J. Newport, B.D. Rainford, G.A. Saunders, and H.B. Senin, "EXAFS and x-ray structural studies of $(Tb_2O_3)_{0.26}(P_2O_5)_{0.74}$ metaphosphate glass," *Phys. Rev. B* **51**, 5739–5745 (1995).
40. A.K. Soper and E.R. Barney, "On the use of modification functions when Fourier transforming total scattering data," *J. Appl. Cryst.* **45**, 1314–1317 (2012).
41. P.S. Salmon, "Decay of the pair correlations and small-angle scattering for binary liquids and glasses," *J. Phys.: Condens. Matter* **18**, 11443–11469 (2006).
42. T. di Cristina, Ph.D. Thesis, 2004, *Structural studies on phosphate glasses for biomedial applications*, Queen Mary, University of London.
43. U. Hoppe, G. Walter, R. Kranold, and D. Stachel, "Structural specifics of phosphate glasses probed by diffraction methods: a review," *J. Non-Cryst. Solids* **263-264**, 29–47 (2000).
44. U. Hoppe, G. Walter, A. Barz, D. Stachel, and A.C. Hannon, "The P-O bond lengths in vitreous P_2O_5 probed by neutron diffraction with high real-space resolution," *J. Phys.: Condens. Matter* **10**, 261–270 (1998).
45. A.C. Hannon, *PFIT correlation function fitting software*, http://www.alexhannon.co.uk/ (Last accessed on 27 July 2015).

46. M. Ueno, M. Misawa, and K. Suzuki, "On the change in coordination of Ge atoms in Na_2O-GeO_2 glasses," *Physica B & C* **120**, 347–351 (1983).
47. E.R. Barney, A.C. Hannon, N. Laorodphan, and D. Holland, "The influence of lone-pair cations on the germanate anomaly in glass," *J. Phys. Chem. C* **115**, 14997–15007 (2011).
48. O.L.G. Alderman, A.C. Hannon, D. Holland, and N. Umesaki, "On the germanium-oxygen coordination number in lead germanate glasses," *J. Non-Cryst. Solids* **386**, 56–60 (2014).
49. H. Ishibashi, K. Shimomoto, and K. Nakahigashi, "Electron density distribution and chemical bonding of Ln_2O_3 (Ln = Y, Tm, Yb) from powder x-ray diffraction data by the maximum-entropy method," *J. Phys. Chem. Solids* **55**, 809–814 (1994).
50. D.L. Weinberg, "Absolute intensity measurements in small-angle X-ray scattering," *Rev. Sci. Instrum.* **34**, 691–696 (1963).
51. J.P. Hansen and I.R. McDonald, *Theory of Simple Liquids*. Academic Press, London, 1986.
52. A.C. Wright, R.A. Hulme, and R.N. Sinclair, "A small angle neutron scattering study of long range density fluctuations in vitreous silica," *Phys. Chem. Glasses* **46**, 59–66 (2005).
53. A. Guinier, *X-Ray Diffraction in Crystals, Imperfect Crystals, and Amorphous Bodies*., Dover, New York, 1994.
54. A. Guinier, "La diffraction des rayons X aux tres petits angles; application à l'étude de phenomenes ultramicroscopiques," *Ann. Phys. (Paris)* **12**, 161–237 (1939).
55. G. Porod, "Die Rontgenkleinwinkelstreuung von dichtgepackten kolloiden Systemen 1. Teil," *Kolloid Z.Z. Polym.* **124**, 83–114 (1951).
56. H.D. Bale and P.W. Schmidt, "Small-angle x-ray-scattering investigation of submicroscopic porosity with fractal properties," *Phys. Rev. Lett.* **53**, 596–599 (1984).
57. J. Teixeira, "Small-angle scattering by fractal systems," *J. Appl. Cryst.* **21**, 781–785 (1988).
58. A.C. Hannon, A.C. Wright, and R.N. Sinclair, "The atomic and magnetic structure of melt-spun amorphous Dy_7Ni_3," *Mat. Sci. Eng. A* **134**, 883–887 (1991).
59. C. Janot and B. George, "Surface-states and magnetic heterogeneity in iron-based glasses," *Journal De Physique Lettres* **46**, L85–L88 (1985).
60. B. Rodmacq, P. Mangin, and A. Chamberod, "Contribution to SANS of the surface-state of $Pd_{80}Si_{20}$ amorphous-alloys," *J. de Phys. Coll.* **46**, 499–503 (1985).
61. D.T. Bowron, A.K. Soper, K. Jones, S. Ansell, S. Birch, J. Norris, L. Perrott, D. Riedel, N.J. Rhodes, S.R. Wakefield, A. Botti, M.A. Ricci, F. Grazzi, M. Zoppi, "NIMROD: The Near and InterMediate Range Order Diffractometer of the ISIS second target station," *Rev. Sci. Instrum.* **81**, 033905 (2010).
62. S.F. Mughabghab, M. Divadeenam, and N.E. Holden, *Neutron Cross Sections. Vol. 1. Neutron Resonance Parameters and Thermal Cross Sections. Part A, Z* = 1–60., Academic Press, New York, 1981.
63. S.F. Mughabghab, *Neutron Cross Sections. Vol. 1. Neutron Resonance Parameters and Thermal Cross Sections. Part B. Z* = 61–100., Academic Press, New York, 1984.
64. E.R. Barney, A.C. Hannon, D. Holland, N. Umesaki, M. Tatsumisago, R.G. Orman, and S. Feller, "Terminal oxygens in amorphous TeO_2," *J. Phys. Chem. Lett.* **4**, 2312–2316 (2013).
65. W.S. Howells and A.C. Hannon, "LAD, 1982-1998: The first ISIS diffractometer," *J. Phys.: Condens. Matter* **11**, 9127–9138 (1999).
66. J.E. Shelby, "Diffusion and solubility of water in alkali borate melts," *Phys. Chem. Glasses* **44**, 106–112 (2003).
67. J.E. Shelby, "A limited review of water diffusivity and solubility in glasses and melts," *J. Am. Ceram. Soc.* **91**, 703–708 (2008).

68. H. Yang, R.I. Walton, S. Antonijevic, S. Wimperis, and A.C. Hannon, "Local order of amorphous zeolite precursors from $^{29}Si\{^{1}H\}$ CPMAS and ^{27}Al and ^{23}Na MQMAS NMR and evidence for the nature of medium-range order from neutron diffraction," *J. Phys. Chem. B* **108**, 8208–8217 (2004).
69. A.K. Soper, "Future perspectives for liquids and amorphous materials diffraction at ISIS," *Inst. Phys. Conf. Ser.* **97**, 353–366 (1989).
70. T. Yamanaka, R. Kurashima, and J. Mimaki, "X-ray diffraction study of bond character of rutile-type SiO_2, GeO_2 and SnO_2," *Z. Kristallogr.* **215**, 424–428 (2000).
71. D.C. Palmer and M. Conley, *CrystalMaker,* CrystalMaker Software Ltd., Oxfordshire, UK. 2013.
72. A. Paul, J.D. Donaldson, M.T. Donoghue, and M.J.K. Thomas, "Infrared and ^{119}Sn Mössbauer spectra of tin borate glasses," *Phys. Chem. Glasses* **18**, 125–127 (1977).
73. H.M. Rietveld, "Line profiles of neutron powder-diffraction peaks for structure refinement," *Acta Cryst.* **22**, 151–152 (1967).
74. A.C. Hannon, E.R. Barney, D. Holland, and K.S. Knight, "Local structure and disorder in crystalline $Pb_9Al_8O_{21}$," *J. Solid State Chem.* **181**, 1087–1102 (2008).
75. J.E. Enderby, D.M. North, and P.A. Egelstaf, "The partial structure factors of liquid Cu-Sn," *Philos. Mag.* **14**, 961–970 (1966).
76. A.C. Wright, A.C. Hannon, R.N. Sinclair, W.L. Johnson, and M. Atzmon, "The neutron diffraction double null isotopic substitution technique," *J. Phys. F* **14**, L201–205 (1984).
77. N.W. Ashcroft and D.C. Langreth, "Structure of binary liquid mixtures. I," *Phys. Rev.* **156**, 685–692 (1967).
78. J.E. Enderby and D.M. North, "Percus–Yevick structure factors for liquid alloys," *Phys. Chem. Liq.* **1**, 1–11 (1968).
79. J.M. Moreau, D. Paccard, and E. Parthe, "The monoclinic, CrB-related, crystal-structure of Tb_3Ni_2, Dy_3Ni_2 and Ho_3Ni_2," *Acta Cryst. B* **30**, 2583–2586 (1974).
80. A.K. Livesey and P.H. Gaskell, "*Accuracy of experimental partial structure factors*," In: *Proceedings of the 4th International Conference on Rapidly Quenched Metals*, vol. 1, Japan Institute of Metals, Sendai, 1982, pp. 335.
81. A.M. Turing, "Rounding-off errors in matrix processes," *Q.J. Mech. Appl. Math.* **1**, 287–308 (1948).
82. M.C. Eckersley, P.H. Gaskell, A.C. Barnes, and P. Chieux, "Structural ordering in a calcium silicate glass," *Nature* **335**, 525–527 (1988).
83. P.H. Gaskell, M.C. Eckersley, A.C. Barnes, and P. Chieux, "Medium-range order in the cation distribution of a calcium silicate glass," *Nature* **350**, 675–677 (1991).
84. I. Petri, P.S. Salmon, and H.E. Fischer, "Defects in a disordered world: The structure of glassy $GeSe_2$," *Phys. Rev. Lett.* **84**, 2413–2416 (2000).
85. A.K. Soper, "The quest for the structure of water and aqueous solutions," *J. Phys.: Condens. Matter* **9**, 2717–2730 (1997).
86. C.J. Benmore, J.K.R. Weber, S. Sampath, J. Siewenie, J. Urquidi, and J.A. Tangeman, "A neutron and X-ray diffraction study of calcium aluminate glasses," *J. Phys.: Condens. Matter* **15**, S2413–S2423 (2003).
87. O.L.G. Alderman, A.C. Hannon, D. Holland, S. Feller, G. Lehr, A. Vitale, U. Hoppe, M. v. Zimmerman, and A. Watenphul, "Lone-pair distribution and plumbite network formation in high lead silicate glass, $80PbO.20SiO_2$," *Phys. Chem. Chem. Phys.* **15**, 8506–8519 (2013).

88. A. Lee, G. Etherington, and C.N.J. Wagner, "Partial structure functions of amorphous $Ni_{35}Zr_{65}$," *J. Non-Cryst. Solids* **61-2**, 349–354 (1984).
89. R.A. Martin, P.S. Salmon, H.E. Fischer, and G.J. Cuello, "Identification of the relative distribution of rare-earth ions in phosphate glasses," *Phys. Rev. Lett.* **90**, 185501 (2003).
90. J.M. Cole, A.C. Hannon, R.A. Martin, and R.J. Newport, "Direct observation of R . . . R distances in rare-earth (R) phosphate glasses by magnetic difference neutron diffraction," *Phys. Rev. B* **73**, 104210 (2006).
91. U. Hoppe, "Rare-earth site distributions in $R(PO_3)_3$ (R = La, Nd, Er, Yb) metaphosphate glasses by reverse Monte Carlo simulations," *J. Phys.: Condens. Matter* **20**, 165206 (2008).
92. J. Blétry and J.F. Sadoc, "Determination of the three partial interference functions of an amorphous cobalt-phosphor ferromagnet by polarized-neutron scattering," *J. Phys. F* **5**, L110–L117 (1975).
93. A.C. Wright, G. Etherington, J.A.E. Desa, and R.N. Sinclair, "Neutron diffraction studies of rare earth ions in glasses," *J. de Phys. Coll.* **C9**, 31–34 (1982).
94. A.C. Wright, J.M. Cole, R.J. Newport, C.E. Fisher, S.J. Clarke, R.N. Sinclair, H.E. Fischer, and G.J. Cuello, "The neutron diffraction anomalous dispersion technique and its application to vitreous $Sm_2O_3.4P_2O_5$," *Nucl. Instrum. Meth. A* **571**, 622–635 (2007).
95. J.M. Cole, A.C. Wright, R.J. Newport, R.N. Sinclair, H.E. Fischer, G.J. Cuello, and R.A. Martin, "The structure of the rare-earth phosphate glass $(Sm_2O_3)_{0.205}(P_2O_5)_{0.795}$ studied by anomalous dispersion neutron diffraction," *J. Phys.: Condens. Matter* **19**, 056002 (2007).
96. B.E. Warren, *X-ray Diffraction*., Addison-Wesley, New York, 1969.
97. C.H.L. Goodman, "The structure and properties of glass and the strained mixed cluster model," *Phys. Chem. Glasses*, **26**, 1–10 (1985).
98. R. Hosemann, M.P. Hentschel, U. Schmeisser, and R. Bruckner, "Structural model of vitreous silica based on microparacrystal principles," *J. Non-Cryst. Solids* **83**, 223–234 (1986).
99. A.C. Wright, "Diffraction studies of glass structure: The first 70 years," *Glass Phys. Chem.* **24**, 148–179 (1998).
100. S.F. Parker, K. Refson, A.C. Hannon, E.R. Barney, S.J. Robertson, and P. Albers, "Characterisation of hydrous palladium oxide: implications for low temperature carbon monoxide oxidation," *J. Phys. Chem. C* **114**, 14164–14172 (2010).
101. A.C. Wright, "Neutron scattering from vitreous silica V. The structure of vitreous silica: What have we learned from 60 years of diffraction studies?," *J. Non-Cryst. Solids* **179**, 84–115 (1994).
102. W.H. Zachariasen, "The atomic arrangement in glass," *J. Am. Chem. Soc.* **54**, 3841–3851 (1932).
103. A.C. Wright and M.F. Thorpe, "Eighty years of random networks," *Phys. Status Solidi B* **250**, 931–936 (2013).
104. R.D. Shannon, "Revised effective ionic radii and systematic studies of interatomic distances in halides and chalcogenides.," *Acta Cryst. A* **32**, 751–767 (1976).
105. A.E. Dwight, "Factors controlling the occurrence of Laves phases and AB_5 compounds among transition elements," *Trans. ASM* **53**, 479–500 (1961).
106. L. Pauling, "The principles determining the structure of complex ionic crystals," *J. Am. Chem. Soc.* **51**, 1010–1026 (1929).
107. L. Pauling, *The Nature of the Chemical Bond*, Cornell University Press, Ithaca, 1960, pp. 547.
108. A.R. West, *Solid State Chemistry and Its Applications*, John Wiley & Sons, Chichester, 1984, pp. 274.

109. N.E. Brese and M. O'Keeffe, "Bond-valence parameters for solids," *Acta Cryst. B* **47**, 192–197 (1991).
110. I.D. Brown, *The Chemical Bond in Inorganic Chemistry*. Oxford University Press, Oxford, 2002.
111. A.C. Hannon and J.M. Parker, "The use of bond-valence parameters in interpreting glass diffraction results," *Phys. Chem. Glasses* **43C**, 6–12 (2002).
112. E.R. Barney, A.C. Hannon, and D. Holland, "Short range order and dynamics in crystalline α-TeO_2," *J. Phys. Chem. C* **116**, 3707–3718 (2012).
113. M.T. Dove, D. Keen, A.C. Hannon, and I.P. Swainson, "Direct measurement of the Si–O bond length and orientational disorder in the high-temperature phase of cristobalite," *Phys. Chem. Min.* **24**, 311–317 (1997).
114. C.A. Yarker, P.A.V. Johnson, A.C. Wright, J. Wong, R.B. Greegor, F.W. Lytle, and R.N. Sinclair, "Neutron diffraction and EXAFS evidence for TiO_5 units in vitreous $K_2O.TiO_2.2SiO_2$," *J. Non-Cryst. Solids* **79**, 117–136 (1986).
115. T. Fukunaga, K. Itoh, T. Otomo, K. Mori, M. Sugiyama, H. Kato, M. Hasegawa, A. Hirata, Y. Hirotsu, and A.C. Hannon, "Voronoi analysis of the structure of Cu-Zr and Ni-Zr metallic glasses," *Intermetallics* **14**, 893–897 (2006).
116. A.C. Wright, "Diffraction studies of halide glasses," In: *Proceedings of the NATO Advanced Research Workshop on Halide Glasses for Infrared Fiberoptics*, R.M. Almeida, ed. Matrinus Nijhoff, Dordrecht, 1986.
117. J.D. Bernal, "The geometry of the structure of liquids," In: *Liquids: Structure, Properties and Solid Interactions*, T.J. Hughel, ed. Elsevier, Amsterdam, 1965, pp. 25.
118. A.G. Clare, A.C. Wright, R.N. Sinclair, F.L. Galeener, and A.E. Geissberger, "A neutron diffraction investigation of the structure of vitreous As_2O_3," *J. Non-Cryst. Solids* **111**, 123–138 (1989).
119. J.C. McLaughlin, S.L. Tagg, and J.W. Zwanziger, "The structure of alkali tellurite glasses," *J. Phys. Chem. B* **105**, 67–75 (2001).
120. A.C. Hannon, B. Vessal, and J.M. Parker, "The structure of alkali silicate glasses," *J. Non-Cryst. Solids* **150**, 97–102 (1992).
121. A. Zeidler, J.W.E. Drewitt, P.S. Salmon, A.C. Barnes, W.A. Crichton, S. Klotz, H.E. Fischer, C.J. Benmore, S. Ramos, and A.C. Hannon, "Establishing the structure of GeS_2 at high pressures and temperatures: a combined approach using x-ray and neutron diffraction," *J. Phys.: Condens. Matter* **21**, 474217 (2009).
122. A.C. Hannon and J.M. Parker, "The structure of aluminate glasses by neutron diffraction," *J. Non-Cryst. Solids* **274**, 102–109 (2000).
123. A.C. Hannon, J.M. Parker, and B. Vessal, "Neutron diffraction analysis of the atomic short range order in lead gallate glasses," *J. Non-Cryst. Solids* **232–234**, 51–58 (1998).
124. P.A.V. Johnson, A.C. Wright, C.A. Yarker, and R.N. Sinclair, "A neutron diffraction investigation of the structure of vitreous V_2O_5-TeO_2," *J. Non-Cryst. Solids* **81**, 163–171 (1986).
125. J.C. Champarnaud-Mesjard, S. Blanchandin, P. Thomas, A. Mirgorodsky, T. Merle-Mejean, and B. Frit, "Crystal structure, Raman spectrum and lattice dynamics of a new metastable form of tellurium dioxide: γ-TeO_2," *J. Phys. Chem. Solids* **61**, 1499–1507 (2000).
126. U. Hoppe, R.K. Brow, N.P. Wyckoff, A. Schöps, and A.C. Hannon, "Structure of potassium germanophosphate glasses by X-ray and neutron diffraction. Part 1: Short-range order," *J. Non-Cryst. Solids* **354**, 3572–3579 (2008).
127. A.J. Leadbetter and A.C. Wright, "Diffraction studies of glass structure I. Theory and quasi-crystalline model," *J. Non-Cryst. Solids* **7**, 23–26 (1972).

128. A.C. Hannon, "*XTAL: A program for Calculating Interatomic Distances and Coordination Numbers for Model Structures*," Rutherford Appleton Laboratory Report RAL-93–063, 1993.

129. A.C. Hannon *XTAL structural modeling software*, http://www.alexhannon.co.uk/ (Last accessed on 27 July 2015).

130. S.C. Moss and D.L. Price, "Random packing of structural units and the first sharp diffraction peak in glasses," In: *Physics of Disordered Materials,* D. Adler, H. Fritzsche, and S.R. Ovshinsky, eds. Plenum, New York, 1985, pp. 77.

131. A.A. Vaipolin and E.A. Porai-Koshits, "The structure of arsenic chalcogenide glasses - vitreous and crystalline states in the As_2Se_3-As_2Te_3 system," *Sov. Phys. Sol. State* **5**, 186–190 (1963).

132. P.M. Bridenbaugh, G.P. Espinosa, J.E. Griffiths, J.C. Phillips, and J.P. Remeika, "Microscopic origin of the companion A_1 Raman line in glassy $Ge(S,Se)_2$," *Phys. Rev. B* **20**, 4140–4144 (1979).

133. A.C. Wright, R.N. Sinclair, and A.J. Leadbetter, "Effect of preparation method on the structure of amorphous solids in the system As-S," *J. Non-Cryst. Solids* **71**, 295–302 (1985).

134. S.R. Elliott, "Origin of the first sharp diffraction peak in the structure factor of covalent glasses," *Phys. Rev. Lett.* **67**, 711–714 (1991).

135. R.J. Bell and P. Dean, "Properties of vitreous silica: Analysis of random network models," *Nature* **212**, 1354–1356 (1966).

136. D.L. Evans and S.V. King, "Random network model of vitreous silica," *Nature* **212**, 1353–1354 (1966).

137. J.L. Finney, "Random packings and the structure of simple liquids I. The geometry of random close packing," *Proc. Roy. Soc. A* **319**, 479–493 (1970).

138. N. Metropolis, A.W. Rosenbluth, M.N. Rosenbluth, A.H. Teller, and E. Teller, "Equation of state calculations by fast computing machines," *J. Chem. Phys.* **21**, 1087–1092 (1953).

139. R.L. McGreevy and L. Pusztai, "Reverse Monte Carlo simulation: A new technique for the determination of disordered structures," *Mol. Simulation* **1**, 359–367 (1988).

140. R.L. McGreevy and P. Zetterström, "Reverse Monte Carlo modeling of network glasses: Useful or useless?," *J. Non-Cryst. Solids* **293–295**, 297–303 (2001).

141. R.L. McGreevy, "Reverse Monte Carlo: Fact and fiction," *J. Non-Cryst. Solids* **156–158**, **Part 2**, 949–955 (1993).

142. D.A. Keen and R.L. McGreevy, "Structural modeling of glasses using reverse Monte Carlo simulation," *Nature* **344**, 423–425 (1990).

143. J.D. Wicks, R.L. McGreevy, and L. Börjesson, "A network problem: Modeling alkali-silicate glasses with RMC," *Phase Transitions* **61**, 195–213 (1997).

144. J. Swenson and S. Adams, "Mixed alkali effect in glasses," *Phys. Rev. Lett.* **90**, 155507 (2003).

145. M.J. Cliffe, M.T. Dove, D.A. Drabold, and A.L. Goodwin, "Structure determination of disordered materials from diffraction data," *Phys. Rev. Lett.* **104**, 125501 (2010).

146. C.R. Müller, V. Kathriarachchi, M. Schuch, P. Maass and V.G. Petkov, "Reverse Monte Carlo modeling of ion conducting network glasses: An evaluation based on molecular dynamics simulations," *Phys. Chem. Chem. Phys.* **12**, 10444–10451 (2010).

147. B.W.M. Thomas, R.N. Mead, and G. Mountjoy, "A molecular dynamics study of the atomic structure of $(CaO)_x(Al_2O_3)_{1-x}$ glass with x = 0.625 close to the eutectic," *J. Phys.: Condens. Matter* **18**, 4697–4708 (2006).

148. E.-T. Kang, S.-J. Lee, and A.C. Hannon, "Molecular dynamics simulation of calcium aluminate glasses," *J. Non-Cryst. Solids* **352**, 725–736 (2006).

149. A.C. Wright, "The comparison of molecular dynamics simulations with diffraction experiments," *J. Non-Cryst. Solids* **159**, 264–268 (1993).

150. L.B. Skinner, A.C. Barnes, P.S. Salmon, H.E. Fischer, Drewitt, J.W.E., and Honkimäki, V., "Structure and triclustering in Ba-Al-O glass," *Phys. Rev. B* **85**, 064201 (2012).

151. W. Smith, C.W. Yong, and P.M. Rodger, "DL_POLY: Application to molecular simulation," *Mol. Simulation* **28**, 385–471 (2002).

152. R. Car and M. Parrinello, "Unified approach for molecular dynamics and density-functional theory," *Phys. Rev. Lett.* **55**, 2471–2474 (1985).

153. J. Sarnthein, A. Pasquarello, and R. Car, "Structural and electronic properties of liquid and amorphous SiO_2: An ab initio molecular dynamics study," *Phys. Rev. Lett.*, **74**, 4682–4685 (1995).

154. R. Evans, "Comment on reverse Monte Carlo simulation," *Mol. Simulation* **4**, 409–411 (1990).

155. A.K. Soper, "Partial structure factors from disordered materials diffraction data: An approach using empirical potential structure refinement," *Phys. Rev. B* **72**, 104204 (2005).

156. J. Swenson and L. Börjesson, "An investigation of the structure of vitreous boron trioxide by reverse Monte Carlo simulations," In: *Borate Glasses, Crystals and Melts*, A.C. Wright, S.A. Feller, and A.C. Hannon, eds. The Society of Glass Technology, Sheffield, 1997, pp. 425–434.

157. J. Swenson and L. Börjesson, "Fraction of boroxol rings in vitreous boron trioxide," *Phys. Rev. B* **55**, 11138–11143 (1997).

158. A.K. Soper, "Boroxol rings from diffraction data on vitreous boron trioxide," *J. Phys.: Condens. Matter* **23**, 365402 (2011).

159. B.E. Warren and N.S. Gingrich, "Fourier integral analysis of X-ray powder patterns," *Phys. Rev.* **46**, 368–372 (1934).

160. F. Garrido, A.C. Hannon, R.M. Ibberson, L. Nowicki, and Willis, B.T.M., "Neutron diffraction studies of U_4O_9 : Comparison with EXAFS results," *Inorg. Chem.* **45**, 8408–8413 (2006).

161. D.J.M. Bevan, I.E. Grey, and B.T.M. Willis, "The crystal structure of β-U_4O_{9-y}," *J. Solid State Chem.* **61**, 1–7 (1986).

162. R.I. Cooper and B.T.M. Willis, "Refinement of the structure of β-U_4O_9," *Acta Cryst. A* **60**, 322–325 (2004).

163. S.D. Conradson, B.D. Begg, D.L. Clark, C. den Auwer, M. Ding, P.K. Dorhout, F.J. Espinosa-Faller, P.L. Gordon, R.G. Haire, N.J. Hess, R.F. Hess, D.W. Keogh, G.H. Lander, D. Manara, L.A. Morales, M.P. Neu, P. Paviet-Hartmann, J. Rebizant, V.V. Rondinella, W. Runde, C.D. Tait, D.K. Veirs, P.M. Villella, F. Wastin, "Charge distribution and local structure and speciation in the UO_{2+x} and PuO_{2+x} binary oxides for $x \leq 0.25$," *J. Solid State Chem.* **178**, 521–535 (2005).

164. D.J. Jones, J. Roziere, G.C. Allen, and P.A. Tempest, "The structural determination of fluorite-type oxygen excess uranium-oxides using EXAFS spectroscopy," *J. Chem. Phys.* **84**, 6075–6082 (1986).

165. C.L. Farrow, P. Juhas, J.W. Liu, D. Bryndin, E.S. Bozin, J. Bloch, T. Proffen, and S.J.L. Billinge, "PDFfit2 and PDFgui: Computer programs for studying nanostructure in crystals," *J. Phys.: Condens. Matter* **19**, 335219 (2007).

166. M.G. Tucker, D.A. Keen, M.T. Dove, A.L. Goodwin, and Q. Hui, "RMCProfile: Reverse Monte Carlo for polycrystalline materials," *J. Phys.: Condens. Matter* **19**, 335218 (2007).

FURTHER READING

Further information of general relevance to neutron diffraction on glasses may be found in the following references.

A.C. Wright, "The Structure of Amorphous Solids by X-ray and Neutron Diffraction," *Adv. Struc. Res. Diffr. Meth*. **5**, 1–120 (1974).

G.E. Bacon, *Neutron diffraction*, Clarendon Press, Oxford, 1975.

A.C. Wright, and A.J. Leadbetter, "Diffraction studies of glass structure," *Phys. Chem. Glasses* **17**, 122–145 (1976).

G.L. Squires, *Introduction to the theory of thermal neutron scattering*, Cambridge University Press, Cambridge, 1978.

C.G. Windsor, *Pulsed neutron scattering*, Taylor and Francis, London, 1981.

A.C. Wright, G. Etherington, J.A.E. Desa, R.N. Sinclair, G.A.N. Connell, and J.C. Mikkelsen, "Neutron amorphography," *J. Non-Cryst. Solids* **49**, 63–102 (1982).

P.A.V. Johnson, A.C. Wright, & R.N. Sinclair, "Neutron Scattering from Vitreous Silica II. Twin-axis Diffraction Experiments," *J. Non-Cryst. Solids* **58**, 109–130 (1983).

S.W. Lovesey, *Theory of neutron scattering from condensed matter*, *Volume 1*. Clarendon Press, Oxford, 1984.

A.C. Wright, "Diffraction studies of halide glasses," In: *Proceedings of the NATO Advanced Research Workshop on Halide Glasses for Infrared Fiberoptics*, R.M. Almeida, ed. Matrinus Nijhoff, Dordrecht, 1986.

D.L. Price, and K. Sköld, "Introduction to neutron scattering," In: *Neutron Scattering Part A*, K. Sköld, and D.L. Price, eds. Academic Press, Orlando, 1986, pp. 1–97.

D.I. Grimley, A.C. Wright, and R.N. Sinclair, "Neutron Scattering from Vitreous Silica IV. Time-of-flight Diffraction," *J. Non-Cryst. Solids* **119**, 49–64 (1990).

A.C. Wright, "Neutron and X-ray Amorphography," In: *Experimental Techniques of Glass Science*, C.J. Simmons and O.H. El-Bayoumi, eds. American Ceramic Society, Westerville, 1993, pp. 205–314.

A.C. Hannon, "Neutron Diffraction, Theory," In: *Encyclopedia of Spectroscopy and Spectrometry*, vol. 2, J. Lindon, G. Tranter, and J. Holmes, eds. Academic Press, London, 2000, pp. 1493–1503.

A.C. Hannon, "Neutron Diffraction, Instrumentation," In: *Encyclopedia of Spectroscopy and Spectrometry*, vol. 2, J. Lindon, G. Tranter, and J. Holmes, eds. Academic Press, London, 2000, pp. 1479–1492.

H.E. Fischer, A.C. Barnes, and P.S. Salmon, "Neutron and X-ray diffraction studies of liquids and glasses," *Rep. Prog. Phys*. **69**, 233–299 (2006).

B.T.M. Willis, and C.J. Carlile, *Experimental neutron scattering*, Oxford University Press, Oxford, 2009.

D.S. Sivia, *Elementary scattering theory for X-ray and neutron users*, Oxford University Press, Oxford, 2011.